UNIVERSITY OF OKLAHOMA

GRADUATE COLLEGE

LABORATORY GEOMECHANICAL CHARACTERIZATION OF THE ARBUCKLE GROUP AND CRYSTALLINE BASEMENT ROCKS IN OKLAHOMA

A THESIS

SUBMITTED TO THE GRADUATE FACULTY

in partial fulfillment of the requirements for the

Degree of

MASTER OF SCIENCE

By

WEIQI YU
Norman, Oklahoma
2017

LABORATORY GEOMECHANICAL CHARACTERIZATION OF THE ARBUCKLE GROUP AND CRYSTALLINE BASEMENT ROCKS IN OKLAHOMA

A THESIS APPROVED FOR THE
MEWBOURNE SCHOOL OF PETROLEUM AND GEOLOGICAL ENGINEERING

BY

_____
Dr. Ahmad Ghassemi, Chair

_____
Dr. Maysam Pournik

_____
Dr. Xingru Wu

Table of Contents

List of Tables

List of Figures

Abstract

In the past decade, the rapidly increase in earthquakes in the State of Oklahoma has drawn serious attention. Some investigations have attributed the increased MEQ to the large amount of wastewater injections as part of hydrocarbon production. The crystalline basement of Oklahoma and the Arbuckle Group, which are situated above the basement rocks, have been considered among the most important geological sequences since they were identified as the major disposal zone and seismic hazard zone. Modeling and analysis of MEQ requires a good understanding of rock and fracture characteristics. Although preliminary research efforts have aimed to understand the injection induced seismicity problems, the laboratory characterizations of the geomechanical and petrophysical properties of the rock from these layers are rear.

In this study, a laboratory characterization program has been carried out to determine the much needed rock elastic properties, strength properties and fracture properties of the Arbuckle Group and two types of crystalline rock, Troy granite and Roosevelt gabbro from its bounding basement. A series of laboratory techniques, such as ultrasonic velocity measurements, multistage triaxial compression test, and multistage shear test have been performed on multiple one-inch right circular cylindered specimens extracted from outcrops and quarries of these geological sequences. In addition, the relations among the measured properties, such as the static and dynamic elastic constants and the mechanical anisotropy have been explored and discussed.

Samples from both the Arbuckle Group and the crystalline basement have been characterized and show to be strong, with a high density of 2.61 to 2.68 g/cc for the Arbuckle limestone and Troy granite, and more than 2.80 g/cc for the Roosevelt gabbro.

The samples show high hardness index of more than 600, 700, and 800 for Arbuckle limestone, Roosevelt gabbro and Troy granite, respectively. High Young's modulus are also the case with 100 GPa for Roosevelt gabbro, and about 60 – 80 GPa for others. The Troy granite is the strongest material with extremely high compressive strength; and the Roosevelt gabbro has the highest stiffness. Furthermore, to characterize the rock joint properties, Barton's shear strength criterion has been deployed. All the fractures have small JRC values, typically 0.2, from back-analysis. The JCS values were obtained and are similar to the UCS determined for intact samples, indicating low level of weathering. The shear stiffness values increase with confining pressure and the Arbuckle limestone tends to have higher stiffness values than the other tested rocks from the basement.

Chapter 1 Introduction

In the past decade, the frequency of earthquakes in State of Oklahoma has dramatically increased and drawn widely attention. According to the United States Geological Survey (USGS), before 2009, only 1.6 earthquakes of magnitude 3.0 or higher happened in Oklahoma area per year. However, this number has become hundred times bigger in recent years. In 2014, as many as 567 earthquakes of 3.0+ in Oklahoma were recorded, making Oklahoma the most seismically active state in the contiguous United States by a substantial margin. Particularly, in November 5, 2011, the record-breaking 5.6 magnitude earthquake happened near Prague area caused more than one million dollars in damage and one people injury. With increasing attention of Oklahoma earthquake hazard, many valuable efforts have been made by scientists to understand the Oklahoma earthquake swarms and to constrain the earthquake damage.

It has been suggested that human activities in unconventional hydrocarbon recovery contribute to the earthquake swarms. More studies are ongoing to discover any possible relationships among disposal well locations, injection volumes, earthquake activity and timing using numerical models and statistical methods.

The crystalline basement and the Arbuckle Group appear to be the two predominant disposal zone sequences, and where much of the seismicity has been observed. Their deformation, stress and pore pressure developments, and pre-existing fracture reactivation are among the most interesting topics for better understanding of seismicity. However, the literature contains very little to no data on the basic geomechanical properties for both the sequences from laboratory measurements. Thus, in order to provide reliable parameters for numerical modeling of production and seismicity, a

laboratory geomechanical and petrophysical characterization program has been developed for rock and fracture properties of the crystalline basement and the Arbuckle Group in the Oklahoma.

A series of geomechanical rock properties such as ultrasonic velocity, elastic modulus, strength and failure envelope, friction angle, cohesion; and fracture properties like shear strength, stiffness, as well as important empirical parameters such as JRC, JCR and $\emptyset_b$ have been determined from rock mechanical laboratory tests. These important properties and their characterization techniques will be introduced through in the literature review and the theoretical background chapters. The research will be beneficial to works that seek further understanding of induced seismicity.

1.1 Literature Review

In this part, related literatures are discussed focusing on two major topics. The first part will briefly review the recent rise in Oklahoma earthquakes and the theories about the relationship between fluid injection and fracture re-activation. Then, some important laboratory measured properties of rock material and the development of relevant characterizing techniques will be discussed.

Since 2009, the frequency of earthquakes has increased drastically, not only within the state of Oklahoma, but in the central and eastern United States. More earthquakes, with bigger magnitudes, happened in Ohio, Arkansas, Texas, and Oklahoma were documented and attributed (Ellsworth 2013) to increased deep injection of wastewater and hydraulic fracturing, as part of the unconventional oil and gas production.

Class II underground injection control (UIC) wells are used to dispose saltwater that originates as "flow-back" water and "produced" water as part of hydrocarbon production. Usually, the water is injected into saline aquifers, sedimentary formations with relatively high porosity and permeability (National Research Council, 2012). Murray organized the Class II UIC well data for 2010 – 2013 by geological zones of completion in Oklahoma. According to data from Oklahoma Corporation Commission (OCC), the Arbuckle Group is the predominant formation used for saltwater disposal in central Oklahoma. From 2010 to 2013, 14.47%-20.86% of active SWD wells were completed in the Arbuckle group, but received 51.74% to 61.94% of the injected water volume (Murray 2014). Taken advantages of availability of injection well data and the seismicity data in Oklahoma, Walsh and Zoback (Walsh and Zoback 2015) compiled published data of monthly aggregate injection of disposal wells, magnitude, times of occurrence of earthquakes, and precise locations of the earthquakes and all injection wells in these area. The results show that three most seismically active study areas are the Cherokee area, Perry area and Jones area. It appears the seismicity increased in response to increases in injection rates. On the other hand, less seismic areas were those with less SWD. At the same year, (McNamara, Rubinstein et al. 2015) published earthquake hypocenter locations and focal plane mechanisms in central Oklahoma, and have shown the vast majority of earthquakes in central Oklahoma to be relatively shallow (less than 6 km depth) and limited to the upper portion of the crystalline basement with some seismicity reaching into the overlying sedimentary sequences, or Arbuckle group. The reactivation of pre-existing faults seems to play an important role in recent Oklahoma earthquakes. This is based on the experience in the Rocky Mountain Arsenal where injection into the crystalline basement was

believed to have caused significant earthquakes increase in the Denver area (Healy, Rubey et al. 1968).

Many other researches results have been published suggesting a link between increase seismicity and injection wells in Oklahoma. e.g., Keranen et al. (2013) suggested a link between the November 2011 event in Prague area (magnitude of 5.7) and many aftershocks and injection-induced slip on a splay of Wilzetta fault, which extended into crystalline basement (Keranen, Savage et al. 2013). The main mechanism appears to be pressure increase in the basement, however a thermal stress component may also be operating (Ghassemi, Tarasovs et al. 2007);(Safari and Ghassemi 2016);(Safari and Ghassemi 2015). When the local geothermal gradient of $27\,^{o}C/km$ (Watson and Harrison 1983) is applied, the earthquake nucleation would be favored at depths of 2-10 km, which match the depth of basement rock in Oklahoma.

Advanced numerical modeling is ongoing to simulate these processes (e.g. Cheng and Ghassemi, 2017). Such modeling works need input data regarding intact and fracture properties. Therefore, laboratory characterizations has been conducted to provide reliable parameters. The laboratory characterization program includes a series of rock mechanical experiments to determine important rock and fracture properties of samples from the Arbuckle Group and crystalline basement of Oklahoma.

Important Laboratory Characterizations

The first classic triaxial test was introduced by Karman in 1911. He successfully tested the rock samples of Carrara marble used a newly designed method, of which a cylindrical rock specimen was put under uniform confining. Then, with confining pressure constant,

the sample was gradually compressed by an increasing axial load applied by an independently controlled piston. In this way, the intermediate and minimum principal stresses, σ_2 and σ_3, are equal to each other. And the maximum principal stress, σ_1, varies. Although called a "triaxial" test, only two of the principal stresses are adjusted independently. However, since it is a relatively easy method to research rock deformation in the laboratory, the technique is still widely used today. True triaxial testing can be done using a polyaxial cell (Haimson and Chang 2000)(Vachaparamphil and Ghassemi, 2017).

In the history of rock mechanics, the triaxial compression test has been used to find out many important properties of different type of rocks. For example, Handin and Hager Jr (1975) tested different types of sedimentary rocks, including anhydrite, dolomite, limestone, sandstone, shale, and siltstone, and observed that the ultimate strength increases with increasing confining pressure for all the tested samples. Also, ductility increases with increasing confining pressure for some types of rock (Handin and Hager Jr 1957). Paterson conducted a series of triaxial compression tests on Wombeyan marble under various confining pressure. He has shown that rock behavior transitions from brittle to very ductile with the increment of applied confining pressure (Paterson 1958).

The failure envelope is among the most essential properties of rock. Conventional methods to obtain failure envelope require multiple triaxial tests under various confining pressures. However, despite the potentially higher cost of time and labor, the quality of results is affected by rock heterogeneity. Especially for reservoir core samples, the feasibly of conventional method is always limited due to lack of availability of sufficient number of samples.

An alternative is the multistage triaxial test. The multistage triaxial test is an important experimental method in laboratory characterization program for obtaining elastic modulus and strength properties of intact rock specimens. In such a test, a single specimen is compressed at several designated confining pressures, or stages, and unloaded after specific unloading criterion been reached for each non-failure stage. These stages are followed by a final stage in which the specimen is compressed until failure. Thus, the mechanical properties of rock at different confining pressures cane be determined from only one sample, and the failure envelope can be estimated from the rock behavior in all stages.

The idea of multistage test was introduced by Kovari and Tisa (1975). But unlike the today's more advanced multistage strategy, their "Multiple Failure State test", used an unloading criterion based on when the sample exhibits sings of approaching failure. Kim and Ko (1979) compared the cohesion and friction angle obtained from such tests to those from single-stage tests for Pierre shale, Raton shale, and Lyons sandstone. According to their observation, the very brittle Lyons sandstone displayed errors as large as 38%. They suggested the effectiveness of multistage triaxial testing depends on rock type and its mechanical properties such as brittleness and hardness. However, for Pierre and Raton shale, the method resulted in 14% error in cohesion(Kovari and Tisa 1975), (Kim and Ko 1979).

The imperfect prototype of multistage testing indicated that unloading the sample at a sign of failure (in the tests conducted by Kim and Ko (1979), this was defined as the stress-axial strain curve apart from linearity) was too late and the rock had already formed

irreversible or permanent damage. Later development suggested using the volumetric strain as the monitoring parameter.

The volumetric strain is defined as the change in volume divided by the original sample volume, or $\varepsilon_{vol} = \frac{\Delta V}{V}$, and can be simplified as $\varepsilon_{vol} = \varepsilon_1 + 2\varepsilon_2$ of the cylinder specimen in triaxial tests, where ε_1 is axial strain and ε_2 is radial strain. In 1966, Brace et al. published the famous study of the relationship between the volumetric strain and fracture initiation. In their study, within a full load-to-failure process, the stress-strain curve can be divided into four stages as shown in Fig. 1. Stage I and II represent primarily elastic behavior without irreversible changes. In region III, crack growth and new faults occur in region IV ultimately lead to failure (Brace, Paulding et al. 1966). One year later, Bieniawski suggested a similar theory based on theoretical and experimental analysis. In more detail, he divided the region III of Fig. 1 into two separate regions, ③ and ④ of Fig. 2. The two regions are divided by a critical stress point, before which the cracks propagation is stable and can be controlled; beyond that critical point, the cracks become unstable and fracture propagation is unstable (Bieniawski 1967).

With gradual understanding of the role of crack initiation and propagation in volumetric strain behavior, Crawford and Wylie (1987) were the first to use the volumetric strain as the monitoring parameter in a multistage triaxial test. They suggested a modified multiple failure state testing method (MFS) in which the stopping criterion is the point where the volumetric strain returns to zero. The applicability of this stopping criterion was tested on two types of rock, Berea sandstone and Lac du Bonnet granite, subjected to both MFS method and the single stage testing method. As the result, the modified method worked quite well for Berea sandstone. But for Lac du Bonnet granite, it was unsuitable since it

was not possible to reach zero volumetric strain point without causing sample failure (essentially no dilation was observed). Although this method was imperfect, the author proposed to use maximum volumetric strain as an alternative to stopping criterion for the Lac du Bonnet granite, which is quite similar to the method that is being used today (Crawford and Wylie 1987).

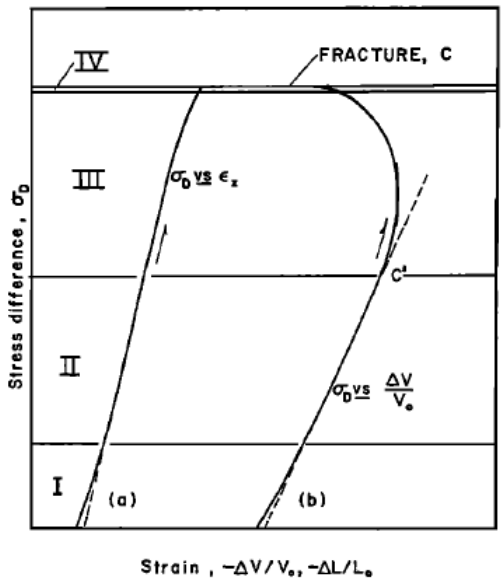

Fig. 0-1 Idealized axial strain and volumetric strain plotted against stress difference divided into four regions. (Brace, Paulding et al. 1966)

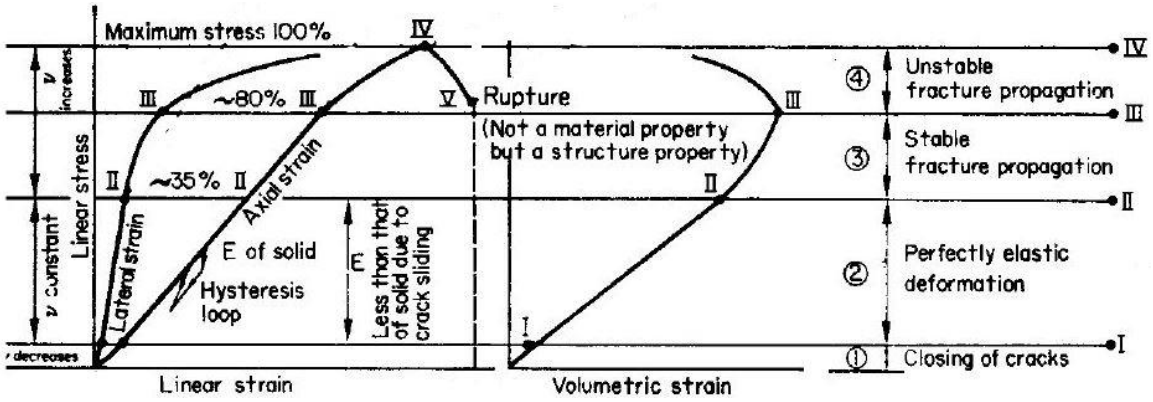

Fig. 0-2 Mechanism of brittle fracture of rock in multiaxial compression (Bieniawski 1967)

In our testing program, the volumetric strain deflection point is used as the stopping criterion in each non-failure stage. The method was firstly proposed by Pagoulatos (2004) in his M.S. thesis and published by Tran et al. afterwards (2010). The method has been successfully applied to different types of rocks, e.g. Newberry tuff (Wang, Jung et al. 2016), and various types of shale (Zhi et al., internal report-OU RSSRG). Theoretically, the selected unloading criterion ensured the compression halted at point III in the Fig. 2 for every non-failure stage. Because no unstable fracture propagation occur before this critical stress level, the quality of multistage triaxial test is considerably improved.

Through multistage triaxial testing, beside with failure envelope and failure properties such as cohesion and friction angle, two essential parameters that describe rock elastic behavior, Young's modulus (E) and Poisson's ratio (ν), are also determined from the stress-strain behavior during the test. The parameters obtained in such mechanical testing method are known as *static elastic parameters*. Another way to characterize those elastic parameters is to calculate them from direct measurements of ultrasonic compressional wave (P-wave) and shear wave (S-wave) velocities through the sample. In this case, the parameters are referred as *dynamic elastic parameters*. Both the static and dynamic elastic parameters are measured in our testing program. The relationship of the elastic constants obtained from the different measuring techniques is discussed in detail later in the thesis.

The use of dynamic methods to obtain mechanical properties, such as Young's modulus, Poisson's ratio, shear modulus, bulk modulus, and others, have been used in the laboratory and field since early 1900's. Due to the fact that the dynamic measured properties are calculated from the wave velocities which do not usually require laboratory testing conditions, the theory has also been developed in acoustic well loggings in the

petroleum industry to obtain in-situ mechanical properties. In general, the laboratory dynamic measurement use different wave frequencies compared to the well loggings. With respect to the static test methods, the dynamic methods have two salient advantages, such as easier to obtain and non-destructive. In the petroleum industry, due to the high cost to retrieving cores for laboratory measures, the wave velocities from well logging are probably the most common data for mechanical property determining. In our testing program, the dynamic and static elastic properties of rocks are determined at the same time. By comparing the results, we can further understand the dynamic-static relations particularly for the targeted formation rocks. The effect of confining pressures on dynamic measured properties will also be discussed. All the test results will help the future understanding of well logging data from Arbuckle Group and the crystalline basement in Oklahoma.

The measurements of acoustic wave velocities through rock materials can be tracked back to early 1900's. Much research was conducted at that time by using dynamic method to determine rock properties both in the laboratory and in-situ. As early as 1935, Weatherby and Faust (1935) collected compressional wave velocity data from fifty wells and found out the P-wave velocities in geological sequences of sandstone, shale, and limestone were related to their geological age of the beds (Weatherby and Faust 1935). Initially, only the compressional wave was used due to the restrictions of the technologies. Then, as the theory and new instruments developed, shear wave was gradually understood and used to obtain the dynamic properties more precisely. Peselnick and Zietz (1959) made use of shear wave velocities to determine the elastic properties of three pieces of fine grained, homogeneous, and well compacted limestone (Peselnick and Zietz 1959). Through both

compressional and shear wave velocities, the complex moduli of elasticity of those rocks were obtained. Just like the dynamic testing method we are using today, the essential of measuring the rocks' dynamic mechanical properties is to obtain the wave velocities for both compressional and shear waves through rocks.

The acoustic wave velocities through rock samples can be measured in different ways in the laboratory. Successfully measurements were reported with various testing methods, such as the resonance method (Gardner, Wyllie et al. 1964), the rotating-plate technique (King and Fatt 1962) and the pulse first-arrival technique (Hughes and Cross 1951). The last technique is the most widely used one today and is utilized in our testing program due to many limitations and complexity of the previous two techniques. In the resonance method, the effect of the jacket on the resonant frequency could not be ignored so that a correction must be used. And in the rotating-plate method, the specimen is required to be in thin parallel-sided shape and rotating in the specific path to produce desired ultrasonic energy. Such measurements required special testing apparatus and sample preparations that do not compatible with other measurements in our testing program. However, for the pulse first-arrival technique, the experimental setup can be easily modified for the multi-stage triaxial test setups – to additionally attach the ultrasonic transduces within the pair of platens in the static mechanical test. Moreover, the sample preparation of this dynamic method is compatible with the conventional triaxial testing method and do not introduce new error. Simply, the pulse first-arrival technique makes it possible for us to obtain the samples' dynamic and static properties at the same time, so that the relationship of static and dynamic measured rock properties can be compared.

The relationship of static and dynamic measured elastic properties gained its popularity in the past few decades. Many scientists devoted to find a comprehensive relationship that could be valid for all different types of rocks. Because if such relationship can be found, the static elastic properties of rocks could be predicted much easier from dynamic measured properties, instead of using the more expensive and time-consuming static laboratory mechanical tests. Different authors have proposed various relations in many different correlation types. For example, some proposed static-dynamic correlation is linear, e.g. (Al-Shayea 2004) (Assefa, McCann et al. 2003); or in quadratic correlation, e.g. (Brotóns, Ivorra et al. 2013); and in exponential correlation. e.g. (Eissa and Kazi 1988). However, the massive researches only proved the value of the static modulus of elasticity cannot be correlated using one single relationship valid for all different types of rock, as proposed by Eissa and Kazi (1988) after performed a statistical analysis using 76 observations from three different sources of information. However, it is still possible and meaningful to propose the correlation that is valid only for certain rock types. In this study, the samples were collected from two neighboring geological sequences in Oklahoma. Hence, because the static-dynamic relation revealed in our study is pointed to for specific rock types, it would be particularly beneficial to the researches and applications in Oklahoma.

Fracture Properties

Previous discussions focused on laboratory characterizations of intact rock properties. However, the behavior of rock mass depends on both the properties of its intact material and the properties of the defects within the rock such as joints, discontinuities, bedding planes and fractures (Rosso 1976). Compared with intact material properties, the

cognition of properties of fractures inside the rock is usually with more difficulties. Generally, failure in rock has occurred in either shear or tensile mode. However, in deep subsurface, high compressive stresses exist so that shear failure can predominate. Although it is difficult to produce tensile stresses under such stress condition (Maurer 1965), hand high pore pressure can cause tensile fracturing.

In our testing program, intact rock samples were tested using multistage triaxial testing method until shear failure occurred. For several tested samples, a single fracture was induced which obliquely cut through the middle of the cylindered sample. These single fracture failure cases are very valuable since their fracture properties tend to be more close to the natural faulting and can be characterized using laboratory method.

Two different laboratory techniques are commonly used for determining the fracture properties: direct shear testing and triaxial shear testing. For direct shear testing, the apparatus of "direct shear boxes" are required, which including an upper box and a lower box. Then the process of joint sliding can be simulated through the relative motions of the two boxes. As the *Standard Test Method for Direct Shear Test of Soils under Consolidated Drained Conditions* (ASTM 1994) suggested, the minimum specimen diameter for circular specimens shall be 2.0 inches in a direct shear test. Thus, because the specimens we use are all 1 inch in diameter, the triaxial shear testing technique is favorable for fracture properties determination in our testing program.

In laboratory shear testing, both the stiffness properties and the strength properties of a rock joint or fracture are determined. This requires the measurements of the loads and displacements on the rock joint or fracture in both the shear and normal directions. In triaxial shear testing, displacement measurements are made in different ways, such as

using clip gages across joints (Swanson and Brown 1972), using a dialatometric device and a displacement transducer (Wawersik 1974). or a mechanical contact cantilever system (Rosso 1976). The latter is used in our tests. In such cantilever system, a ring shaped apparatus with two pairs of transverse cantilevel beams were designed to monitor the fracture sliding of a cylindered jointed rock sample. More details of the test setups will be introduced in the following chapters. Rosso (1976) has validated this technique by comparing the obtained joint stiffness properties to the properties measured by a direct shear test. Good agreement in shear stiffness values were observed. However, those measured stiffness properties shown considerable differences with the values obtained from in-situ or measured by the triaxial shear testing using clip gages across joints. It was considered that the method Rosso proposed better represents the true joint stiffnesses because his method measures the displacement closer to the actual shear plane.

The characterization of shear strength envelope of rock joint is significant for reservoir simulation and seismicity research because it demonstrates the stress condition of which the fault sliding initiates. In our tests, since the strength envelope of the joints are desired and there was no identical naturally induced joints for multiple measurements, the multistage strategy was also applied to triaxial shear testing. The multistage triaxial shear testing has been successfully used in the laboratory for measuring the joint properties of different types of rocks, including Newberry tuff, Welded tuff and various types of shale (Li, Wang et al. 2012); (Wang, Jung et al. 2016); (Ye, Ghassemi et al. 2016).

For naturally induced joints, due to the effect of joint roughness, the shear strength envelop is not linear. As shown in the Fig. 1-3, although at high normal stresses it was known that Coulomb relationship would be valid since the shear motion tend to crush the

asperity rather than ride over them, at zero normal stress, however, the shear strength of opened rock joint is turned to be zero (Barton 1976), which means at low normal stresses the shear envelope is not just extension from it at higher normal stresses. In other words, non-linear models were needed to explain frictional behavior both for low and high stress levels.

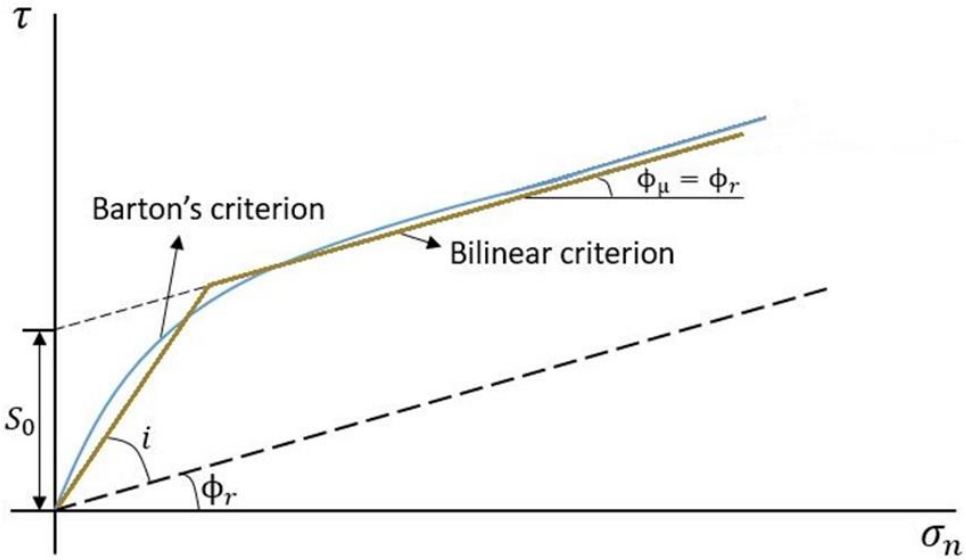

Fig. 0-3 Different shear strength criteria of rock joints

Many models have been proposed to describe the rock joint strength behavior. For instance, Patton (1966), proposed a bilinear shear strength criterion for rock joints, described as in Eqn. (1) and (2).

$$\tau_p = \sigma_n \tan(\phi_\mu + i) \quad (1)$$

$$\tau_p = S_j + \sigma_n \tan(\phi_r) \quad (2)$$

where, Eqn. (1) is for small normal stress, Eqn. (2) for large normal stress, and ϕ_μ is the friction angle of an ideally smooth joint surface, i is the average asperities inclination angle from the mean joint plane (Patton 1966).

However, Barton (1976) has argued that the actual value of i for a given joint surface is difficult to estimate without performing a shear test. More importantly, a curved peak strength envelope is more likely to demonstrate the relationship between shear and normal stress from many observations, e.g. (Jaeger 1971), (Landanyi and Archambault 1970). Barton (1976) has proposed the famous empirical laws of friction and fracture - Barton's model:

$$\tau = \sigma_n \tan\left(JRC\ log_{10}(\frac{JCS}{\sigma_n}) + \emptyset_b\right) \quad (3)$$

where JRC and JCS are two empirical parameters proposed by Barton (1976). JRC represents the "joint roughness coefficient", scaled from 20 to 10, indicating roughest joint surface to the smoothest joint surface. And JCS represents the "joint wall compressive strength", which is a strength parameter that related to the UCS, unconfined compressive strength of rock, and weathering conditions of the joint surface.

The Barton's model has been selected to interpret the joint strength behavior in our testing program. From the shear and normal stresses we measured at the point of joint slipping, the shear strength envelope of jointed rock can be estimated using curve-fitting method. Thus, those empirical parameters can be determined from the back-analysis. Barton has constructed complete physical descriptions and systematic methods to measure those parameters. Thus, unlike the many parameters proposed in other models, the empirical parameters in Barton's model were more generally used in numerical simulations related

with joint deformations. More details about Barton's model and the descriptions of the empirical parameters he proposed will be introduced with more details later on in the thesis.

1.2 Study Objective

The goal of this study is to characterize the geomechanical properties of the Arbuckle Group and the crystalline basement rocks and fractures using laboratory testing. This goal will be achieved by:

- Collecting and preparing samples for laboratory experiments. Describing weight, hardness index, and condition before of each sample
- Conducting triaxial multistage tests on the samples while measuring the ultrasonic compression and shear wave velocities at designated confining pressures
- Obtaining elastic parameters from both static and dynamic experimental measurements, and studying the static-dynamic relation as well as the effects of different confining pressures and lithology
- Constructing failure envelopes for tested samples and determining the strength properties such as cohesion and internal friction angle
- Obtaining jointed samples from previous triaxial tests and conducting multistage shear tests on these samples with naturally induced joints
- Constructing shear envelops for tested samples with Barton's model and calculating important fracture properties such as normal and shear stiffness.
- Evaluating potential relations among all measured properties

Chapter 2 Theoretical Background

2. 1 Mechanical properties

Compressive strength, Young's modulus, Poisson's ratio, failure envelope, angle of internal friction and cohesive strength are some of the most commonly required mechanical rock properties for design in activities such as drilling, hydrocarbon producing and hydraulic fracturing.

Both static and dynamic elastic constants, such as Young's modulus and Passion's ratio, are obtained from the multistage triaxial testing while the ultrasonic compression and shear wave velocities are continuously measured. During the test, designated confining pressure, σ_c, is applied. Then the axial compressional stress, σ_1, is gradually increased until the predetermined stopping criterion (onset of dilation) is reached, except for in the last failure stage where the sample will be compressed until failure. The applied stress and the resulting strains are monitored. The strain is defined as the change of the length over the initial length due to the applied stress change. The axial strain, ε_1, which has the same direction as the applied compressional stress, σ_1, and the radial strain, ε_2, which reflect the circumference change of the cylinder, as well as the volumetric strain, ε_v, which is calculated from the axial and radial strain and describes the change in sample volume are recorded and displayed in the real time.

2.1.1 Elastic Rock Properties

In physics, elasticity is the ability of a body to resist a distorting influence or deforming force and to return to its original size and shape when that influence or force is removed.

In general, rock is not ideal elastic material. Hence, some assumptions are frequently used while determining the elastic rock properties (1) linear elasticity, (2) isotropic, and (3) small deformations.

The rock elastic properties are usually described by elastic constants such as Young's modulus (E) and Poisson's ratio (ν). Other related parameters include the Bulk modulus (K), Shear modulus (G), and Lame's first parameter (λ). For homogeneous isotropic linear elastic materials only the first 2 are needed and can be used to calculate the others. Usually, the measurements of elastic properties of rock are restricted to the linear portion of the stress-strain plot, where the rock behavior can be considered as linearly elastic.

Young's Modulus

When a rock specimen is subjected to load of compression or tension within its elastic range, the ratio of the stress to the strain in the direction of applied load is its Young's modulus, or modulus of elasticity, as in equation (2.1).

$$E = \frac{\sigma_1}{\varepsilon_1} \tag{2.1}$$

where σ_1 is axial stress and ε_1 is axial strain.

The Young's modulus is also an essential attribute of rock that is controlled by rock texture, structure, and stress. It is also affected by the conditions of rock such as water saturation and pore pressure. Moreover, for laboratory characterization, the value of Young's modulus varied by different ways to extract information from the stress-strain curves of the tests. There are three most commonly used methods to calculate Young's modulus, as described below and shown in Fig. 2-1:

Tangent Young's modulus at a stress level that is come fixed percentage, usually 50% of the maximum strength, as in Fig. 2-1(a);

Average Young's modulus which is the average slope of the straight-line portion of the stress-strain curve, as in Fig. 2-1(b);

Secant Young's modulus, usually from zero stress to some fixed percentage of maximum strength, as in Fig. 2-1(c).

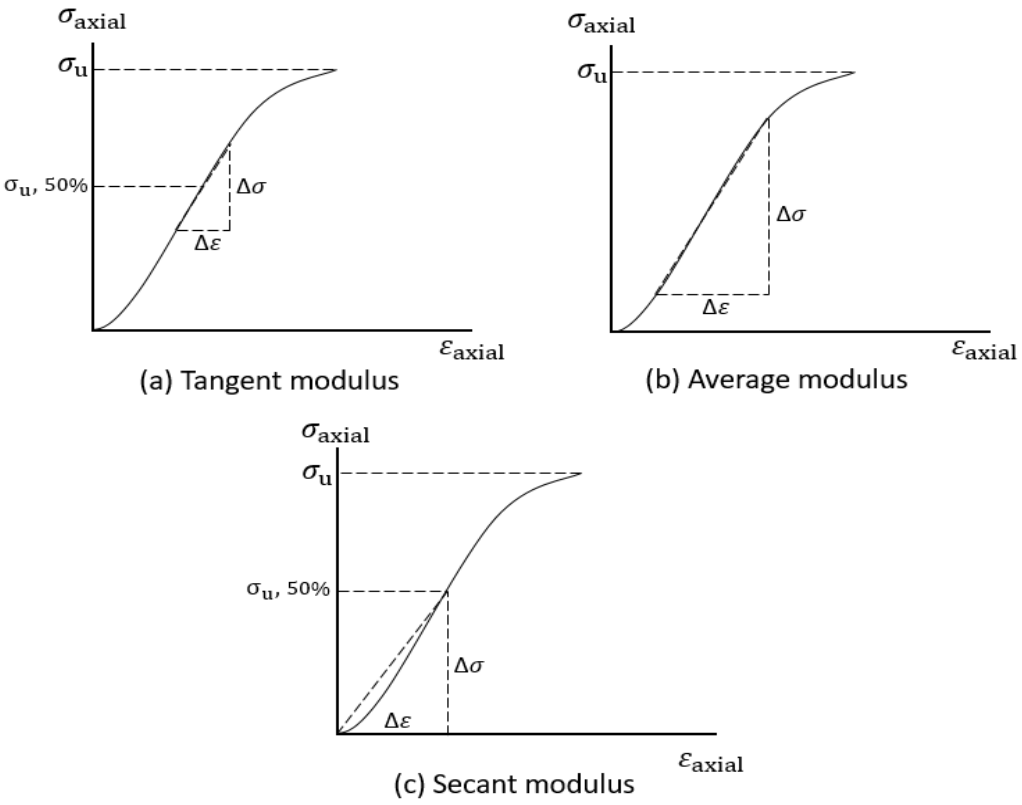

Fig. 0-1 Methods of calculating Young's modulus from axial stress-strain curve

Poisson's Ratio

The Poisson's ratio (v) is defined as the signed ratio of transverse strain to axial strain. It is a measure of the Poisson effect, the phenomenon in which a material tends to expand in directions perpendicular to the direction of compression.

In the laboratory characterization, the value of Poisson's ratio, ν, is greatly affected by nonlinearity at low-stress levels in the axial and lateral stress-strain curve. ASTM Designation D7012-14 suggest the desirable calculation of the Poisson's ratio as in equation (2.2).

$$\nu = \frac{slope\ of\ axial\ curve}{slope\ of\ lateral\ curve} = -(\frac{\varepsilon_2}{\varepsilon_1}) \tag{2.2}$$

where ε_2 is lateral strain and ε_1 is axial strain.

Shear and Bulk Moduli

The shear modulus (G) describes the stiffness of rock bearing shear force, and the bulk modulus (K) measures how it resistant to hydrostatic compression. Both of the moduli are not directly measured in triaxial compression testing, however, they can be calculated using the equation (2.3) and (2.4) in terms of the Young's modulus and Poisson's ratio, if isotropic is assumed:

$$G = \frac{E}{2(1+\nu)} \tag{2.3}$$

$$K = \frac{E}{3(1+2\nu)} \tag{2.4}$$

where, E is Young's modulus, and ν is Poisson's ratio.

Dynamic Moduli

Dynamic properties are obtained using pulse velocities measurements of rock specimens. The pulse velocities of compressional wave, P-wave and shear wave, S-wave are computed from the travel times determined from the laboratory testing using pulse first-arrival technique (Hughes and Cross 1951). The dynamic moduli, or ultrasonic elastic constants can be calculated by the equations (2.5) to (2.8) (ASTM 2008):

Dynamic Young's Modulus,

$$E_{dyn} = \frac{\rho V_s^2 (3V_p^2 - 4V_s^2)}{V_p^2 - V_S^2} \tag{2.5}$$

Dynamic Poisson's ratio,

$$\nu_{dyn} = \frac{V_p^2 - 2V_s^2}{2(V_p^2 - V_s^2)} \tag{2.6}$$

Dynamic Shear modulus,

$$G_{dyn} = \rho V_S^2 \tag{2.7}$$

Dynamic Bulk modulus,

$$K_{dyn} = \frac{\rho(3V_p^2 - 4V_s^2)}{3} \tag{2.8}$$

where ρ is bulk density of corresponding specimen, and v_p is compressional wave velocity, and v_s is shear wave velocity.

Since rock is not ideal material thus cannot be perfectly isotopic and linearly elastic. Also, due to the effect of micro-fractures, the dynamic and static elastic properties usually do not match. Both methods are used for obtaining the elastic moduli of rock samples in out testing program for comparison purposes.

Anisotropic Stiffness Matrix

Seismic anisotropy in underground sedimentary sequences is important to petroleum exploration and production and will affect the interpretation of seismic data. The Thomsen parameters, ε, γ, δ are widely used to describe an anisotropy material. The idea of Thomsen's anisotropy parameter is to separate the influence of the anisotropy from the "isotropic". The dimensionless parameters: ε, γ, and δ go to zero for isotropic media. The magnitudes of the parameters therefore characterize the level of the anisotropy. For the physical meanings, ε and γ define P- and S-wave anisotropies, respectively. The meaning of δ is less transparent, indicating the second derivative of the P-wave phase-velocity function at vertical incidence.

When the ultrasonic wave velocities are obtained from three directions, perpendicular, parallel and with 45° angle to the symmetric axis, the anisotropy parameters are able to be calculated for transversely isotropic material: (Thomsen 1986) (Mavko, Mukerji et al. 2009)

$$c_{11} = \rho\, V_p^2(90°) \tag{4.1}$$

$$c_{12} = c_{11} - 2\rho\, V_{SH}^2(90°) \tag{4.2}$$

$$c_{33} = \rho\, V_p^2(0°) \tag{4.3}$$

$$c_{44} = \rho\, V_{SH}^2(0°) \tag{4.4}$$

$$c_{66} = \rho\, V_{SH}^2(90°) \tag{4.5}$$

$$c_{13} = -c_{44} + \sqrt{4\rho^2 V_p^4(45°) - 2\rho\, V_p^2(45°)(c_{11} + c_{33} + 2c_{44}) + (c_{11} + c_{44})(c_{33} + c_{44})} \tag{4.6}$$

Then, the dynamic Young's modulus for the material in vertical and horizontal directions are:

$$E_{perp.} = C_{33} - \frac{2C_{13}^2}{C_{11}+C_{12}} \tag{4.7}$$

$$E_{para.} = C_{11} - \frac{C_{13}^2(-2C_{11}+C_{12})+C_{12}(-C_{33}C_{12}+C_{13}^2)}{C_{11}C_{33}+C_{13}^2} \tag{4.8}$$

And the anisotropy parameters can be determined as:

$$\varepsilon = \frac{c_{11}-c_{33}}{2c_{33}} \tag{4.9}$$

$$\delta = \frac{(c_{13}+c_{44})^2-(c_{33}-c_{44})^2}{2c_{33}(c_{33}-c_{44})} \tag{4.10}$$

$$\gamma = \frac{c_{66}-c_{44}}{2c_{44}} \tag{4.11}$$

2.1.2 Compressive Strength

The strength is the ability of a material to resist externally applied forces. In engineering practice, strength maybe regarded as the force per unit area necessary to bring a material about rupture at given conditions.

Rock strength is one essential attribute that governed by the mineral composition and structures. The laboratory characterized rock strength is somewhat relative in that it would be different if any of many governing parameters such as the size of rock specimen,

load rate, stress condition, temperature, and fluid content change. Thus, the strength properties on an intact laboratory rock specimen may be different from the strength of the in-situ rock from which the specimen was sampled.

In rock mechanics, several experiment methods have been suggested with specific standards and requirements to ensure the consistency of measurement from laboratory to laboratory. In our testing program, the strength is determined in the failure stage of the multistage triaxial compression test, namely, triaxial compressive strength. In general, the relation of stress and strain in the direction of compression during a triaxial test is like in Fig. 2-2(a), where the ultimate strength is simply the maximum supported load before failure and losing consistency. In some situations when the rock is ductile, the stress-stain figure can also be similar to that in Fig. 2-2(b) and the rock can take permanent deformation without losing its ability to support load. In our tests, the test is usually stopped when the strain has reached a value of 2%.

With the monitored confining pressure and the measured ultimate compressive strength, the shear strength of the rock is also determined according to Mohr-Coulomb theory. The determination of shear strength from the ultimate compressive strength will be introduced later in this chapter.

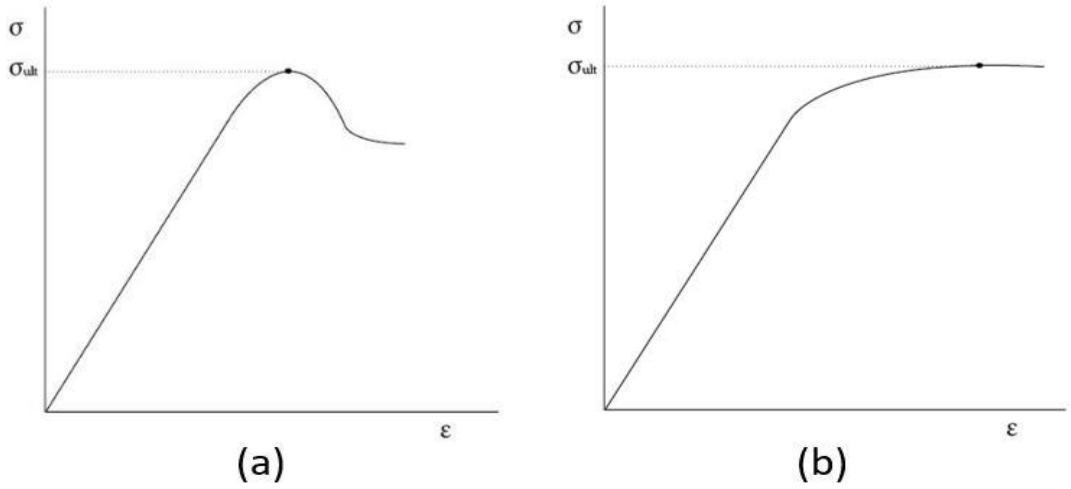

Fig. 0-2 The deformations behavior for rocks in triaxial compression

2.1.3 Mohr-Coulomb Failure Envelope

From a triaxial compression test, the effective normal (σ_n) and shear stress (τ) on the failure plane can also be calculated using the maximum (σ_1) and minimum principal stress (σ_3) by projecting forces acting on the free body rock element for equilibrium. The maximum and minimum principal stresses are equivalent to the triaxial compressive strength and the confining pressure of the failure stage respectively. As shown in Fig. 2-3(b), the effective normal and shear stresses can be calculated by the equations (2.9) and (2.10), as a function of the angle of failure (θ):

$$\sigma_n=\frac{\sigma_1+\sigma_3}{2}+\frac{\sigma_1-\sigma_3}{2}cos2\theta \tag{2.9}$$

$$\tau=\frac{\sigma_1-\sigma_3}{2}sin2\theta \tag{2.10}$$

Hence, the triaxial compression test indirectly gives the shear strength of the rock, expressed by the equation of Mohr-Coulomb theory as:

$$\tau = \sigma_n \tan\phi + c \tag{2.11}$$

where ϕ is angle of internal friction and c is the cohesion.

Fig. 2-3(a) represents a cylindered specimen under the triaxial testing condition. The uniform confining pressure is kept constant around the specimen making the intermediate and minimum principal stresses, σ_2 and σ_3, to be equal to each other. The maximum principal stress, σ_1, is applied in axial direction of the specimen.

This stress state can be represented by one circle in a normal stress vs shear stress plot, also known as the Mohr's circle. The Mohr's circle is constructed as in Fig. 2-3(b), where the two intersections of the circle with x-axis are σ_3 and σ_1, respectively. The center of the Mohr's circle is $\frac{\sigma_1+\sigma_3}{2}$. When the σ_1 is the compressive strength of the specimen and angle of the failure plane is known, the corresponding normal and shear stresses act on that plane can be found as in Fig. 2-3(a) and (b), where θ is the angle of failure plane, and α is the angle of the normal to the failure plane with the horizontal. In the Mohr's circle, the angle of failure plane, θ, measured counterclockwise from σ_1, and α is measured from pole of normal, n*.

Doing this for multiple samples at different values of confining pressure (σ_3) yields a series of Mohr's circles are obtained as those shown in the Fig. 2-3(c). The often linear failure envelope is called the Mohr-Coulomb failure envelope and is constructed by drawing the best-fit straight line that tangent to those circles. The angle of the line with the horizontal is the internal friction angle, ϕ; the intercept of the line with vertical axis is the cohesion of the rock, c.

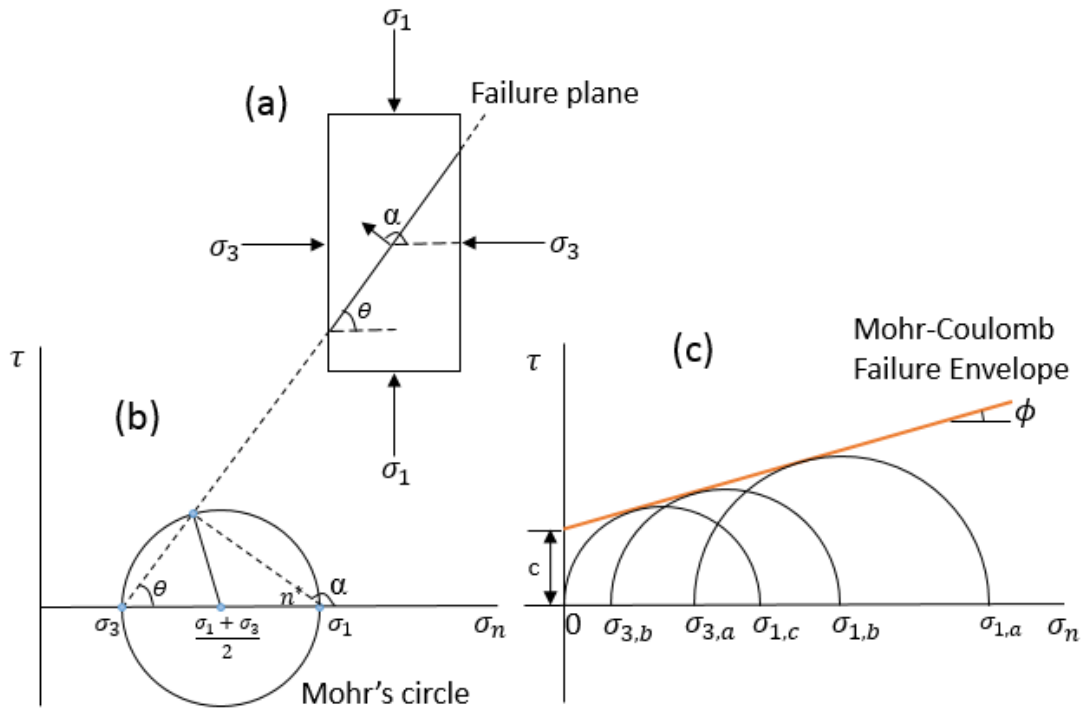

Fig. 0-3 Mohr's Circles and Mohr-Coulomb Failure Envelope

The conventional method to obtain the Mohr-Coulomb failure envelop requires triaxial compression tests on multiple samples of the same rock, which requires good sample availability and could suffer from heterogeneity of different samples. Fig. 2-4 shows another method to construct Mohr-Coulomb failure envelop from a multistage triaxial test using only a single rock specimen. In the figure, there are five 'stages', with four non-failure stages and one failure stage at different confining pressures (σ_3). The Mohr's circles for non-failure stages are constructed using the axial stress (σ_1) at the volumetric strain deflection point in each stage instead of the point of ultimate strength. Mohr's circle for the failure stage is also obtained as the grey dash line. With the first five Mohr's circles, a best-fit tangent line is constructed. This is not a failure envelop, but "the envelope of volumetric strain deflections". This envelope is parallel to (is assumed to be),

but lower than the actual failure envelope. Note the sample is brought to failure in the last confining pressure stage, which yields both stress at failure and at the volumetric strain deflection point. The Mohr's circle of rock failure is also obtained, drawn in blue solid line in the figure. Then, the failure envelope of sample is obtained by shifting "the envelope of volumetric strain deflections" so that it becomes tangent to the real Mohr's circle from the actual failure stress.

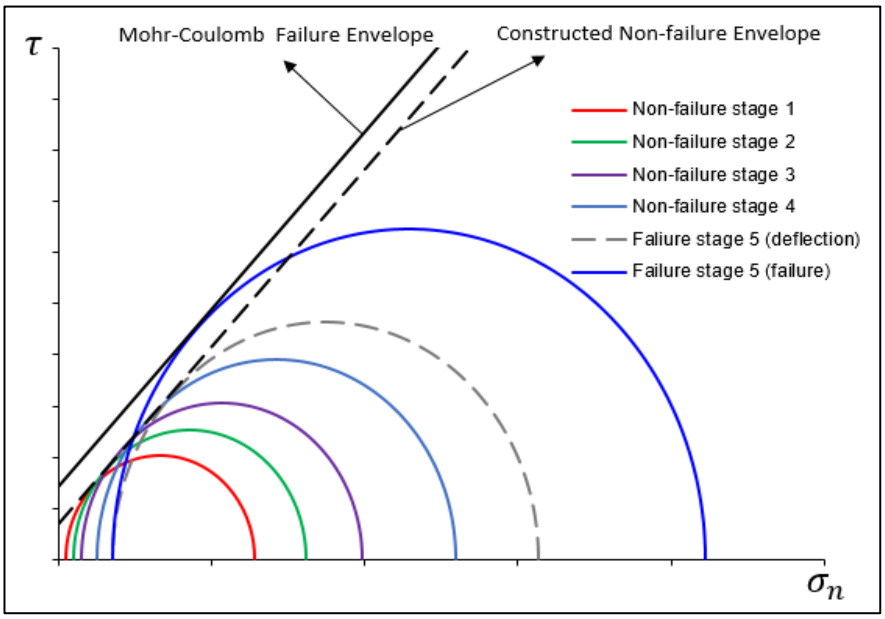

Fig. 0-4 Construction of Mohr-Coulomb envelope from a multistage triaxial test

Preliminary research has been conducted on a series of mechanical tests on Berea sandstone to validate the major assumption of the multistage triaxial compression test – the failure envelope has the same slope with the non-failure envelope obtained from the rock dilation. Pagoulatos (2004) has compared the experimental results between multistage and single stage mechanical testing. It turns out the stress difference between the stress at the deflection and failure can be seen as confining pressure independent for

confining pressures between 0 to 40 MPa. The stress difference has also been plotted against different rock properties, including clay content, elastic modulus, porosity, and permeability. And no meaningful correlation was observed. In the same research, they obtained failure properties of the conventional testing method have $\pm$7.4% uncertainty in cohesion and $\pm$1.6% in internal friction angle due to heterogeneity. However, the obtained UCS from both methods are closely comparable, with only 0.7% difference.

2.2 Fracture Properties

The fracture properties are obtained using a triaxial shear testing method in our laboratory characterization program. The triaxial shear test using a mechanical contact cantilever system was proposed by R. S. Rosso (1976). As shown in the Fig. 2-5, the system consists of a ring with four strain-gaged steel cantilever beams mounted perpendicular to the plane of the ring used to measure the sliding of the joint. The free ends of two pairs of transverse cantilever beams have screws mounted on them to contact the side of the specimen. The output from the cantilever system report the relative displacements between points A and B (d_3), C and D (d_2), respectively. As shown in the diagram on the right of figure, A and B are cross the joint surface; C and D are on the same side of the joint surface, usually 2 mm below (or above) the joint surface. So, at the moment of joint sliding, the change in d_3 would be much bigger thand_2. By monitoring the two transverse displacement, d_3 and d_2, during the testing, we can diagnostic the sliding of the rock joint.

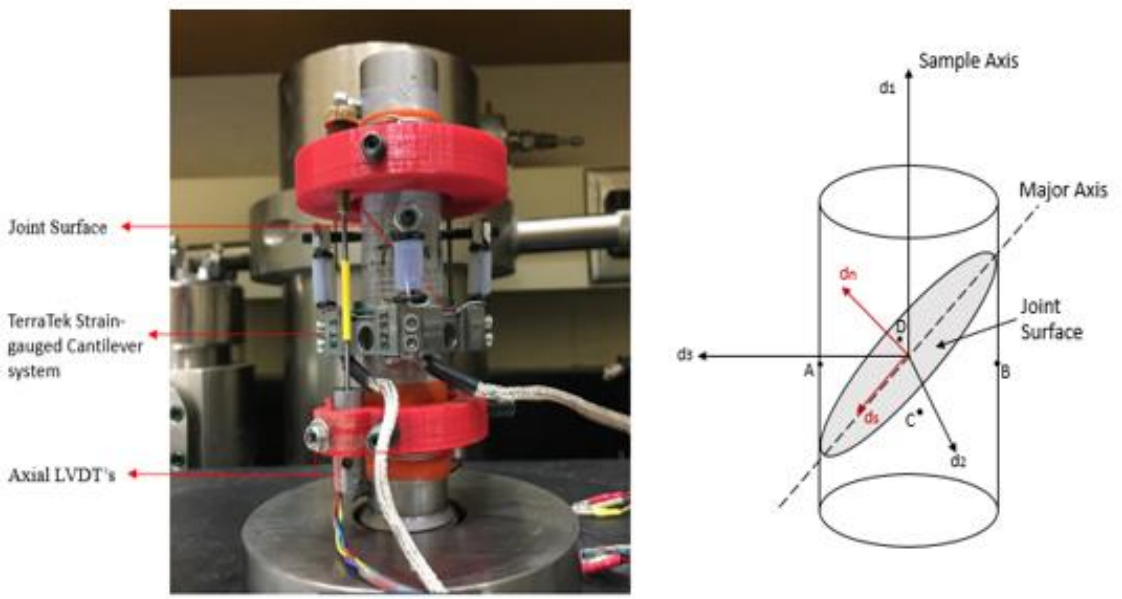

Fig. 0-5 Schematic of Rock Joint Test with contact Cantilever system

In the triaxial shear testing, beside with the two transverse displacements, the confining pressure (σ_3), axial load (σ_3), and axial displacement (d_1) are also measured. The calculation of fracture properties are based on those measurements.

Notice that, the cantilever contact at point A may slide along the specimen during the test. This could introduce an error in d_3. However, Rosso (1974) proved that it only contributed less than a 1% error in the displacement measurement.

2.2.1 Fracture stiffness

The stiffness is the ratio of the force applied on the body to the displacement produced by the force along the same degree freedom. It represents the resistance to an applied fore. As applied to the fracture and joint of rock, the stiffness in normal and shear directions along joint or fracture surface are two of the most need properties. Equation (2.12) and (2.13) gives the normal and shear stiffness by the definition:

$$K_n = \frac{\sigma_n}{d_n} \tag{2.12}$$

$$K_s = \frac{\tau}{d_s} \tag{2.12}$$

where K_n and K_s are normal and shear stiffness, σ_n and τ are normal and shear stresses, and d_n and d_s are the displacements in corresponding normal and shear directions.

To calculate the stiffness values, the stresses and displacements in normal and shear directions along fracture or joint surface are required. The normal and shear stresses on the joint surface in the triaxial testing are represented by equations (2.9) and (2.10) in the previous section. The corresponding displacements measured during testing, however,

consist of two parts: (1) the elastic contribution, which is the elastic deformation of competent rock; and (2) the absolute deformation of rock joint. To calculate the absolute axial displacement caused by joint movement, the intact rock deformation in axial direction under axial stress must be subtracted from the total axial displacement obtained from the axial LVDT (d_1), which is the part after minus sign in the equation (2.13). Similarly, the transvers displacement caused by joint movement is obtained by the total displacement (d_3) minus the rock deformation only caused by axial stress change (d_2):

$$v = d_1 - \frac{\sigma_1}{E} \cdot L \tag{2.13}$$

$$d_{transverse} = d_3 - d_2 \tag{2.14}$$

where, d_{axial} is the absolute axial displacement of rock joint; $d_{transverse}$ is the absolute transverse displacement of rock joint; d_1 is the measurements of axial displacement; d_2 and d_3 are the of transverse displacements measured by two pairs of the cantilever beams; σ_1 is axial stress; E and L are the elastic modulus and the length of the jointed rock sample.

Finally, as in Fig. 2-6, projecting the displacements with respect to the joint surface, we have:

$$d_n = \left(d_1 - \frac{\sigma_1}{E} \cdot L\right) sin\theta - (d_3 - d_2)cos\theta \tag{2.15}$$

$$d_s = \frac{(d_3 - d_2) + d_n cos\theta}{sin\theta} \tag{2.16}$$

where θ is the inclination angle of joint plane.

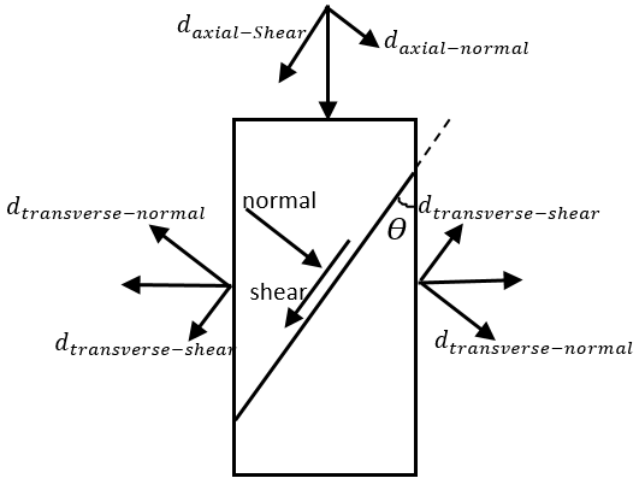

Fig. 0-6 Displacements projection in normal and shear directions

2.2.2 Barton's Shear Strength Criterion

Although in some situations, the linear Mohr-Coulomb failure envelope is valid to describe the shear strength of a jointed rock, such as at very high normal stresses, or for saw-cut samples with very smooth joint surfaces; For most natural rough joint surfaces, a curved peak strength envelope is needed to describe the frictional behavior both for low and high stress levels. Fig. 2-7 presents several famous shear strength criterion for jointed rocks.

In order to determine the best failure envelope of the jointed rocks, we selected the widely used Barton's shear strength criterion, as described in equation (2.17):

$$\tau = \sigma_n \tan\left(JRC\ log_{10}\left(\frac{JCS}{\sigma_n}\right) + \phi_b\right) \tag{2.17}$$

where, JRC and JCS are two empirical parameters proposed by Barton (1976) that will be described below, and ϕ_b is the angle of shearing resistance mobilized at high normal

stress levels at which all dilantancy effects are suppressed as all the asperities are sheared off forming a smooth shearing plane.

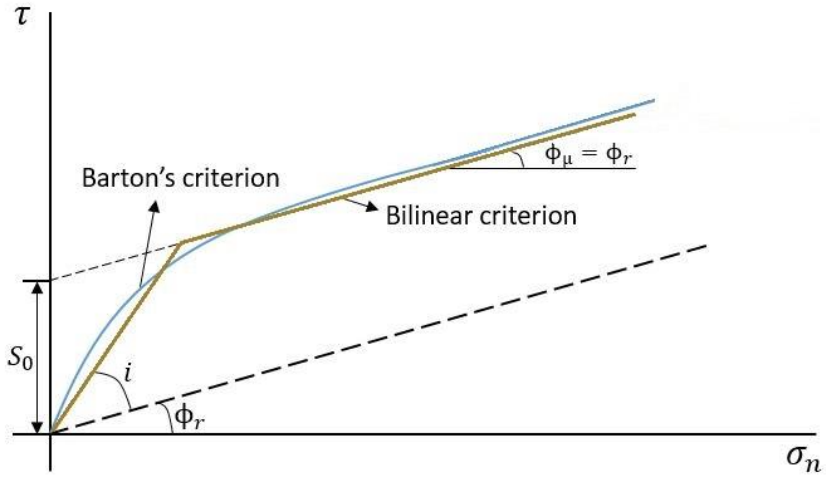

Fig. 0-7 Different shear strength criteria of rock joints

The JRC, or joint roughness coefficient, represents a sliding scale of roughness which varies from approximately 20 to 0, from the roughest to the smoothest. Typical roughness profiles and their corresponding JRC values were suggested as in Fig. 2.7(Barton and Choubey 1977). The JCS, or joint wall compressive strength, is equal to the unconfined compression strength of rock if the joint is unweathered. For a weathered the joint walls, it may reduce to approximately 1/4 of the unconfined compression strength value. Both empirical parameters have well established physical meanings and are widely used for predicting the initiation of fracture sliding. From laboratory triaxial shear test, The Barton's shear strength envelope and the JRC, JCS values will be obtained from back-analysis.

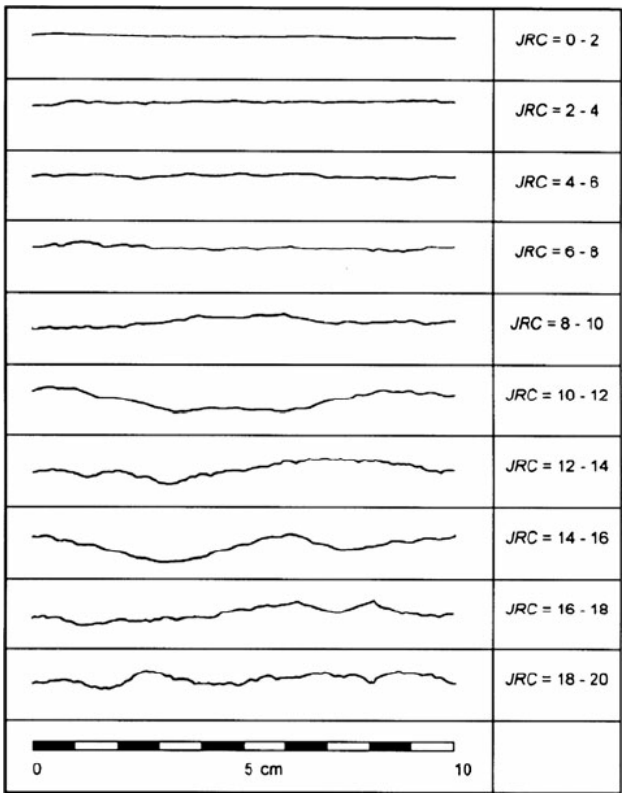

Fig. 0-8 Typical roughness profiles and their corresponding JRC values (Barton and Choubey 1977)

Chapter 3 Sample Preparation and Characterization

3.1 Rock Types

The Arbuckle Group

The Arbuckle group is a major geological formation in the midcontinent of the United States that underlies several important petroleum producing zones, such as West Mayfield in Anadarko basin, Wilburton in the Arkoma basin and Cottonwood Creek in Ardmore basin (Fritz et al., 2013). In Oklahoma, the Arbuckle group underlies nearly the entire state. The structure map in Fig. 3-1 presents the distribution of the Arbuckle group in Oklahoma. As shown in the structure map, the Arbuckle majorly outcrops in four areas in Oklahoma: (1) the Wichita Uplift geologic province of southwestern Oklahoma; (2) the Arbuckle Uplift geologic province of south-central Oklahoma; (3) the Ozark Uplift geological province of northeastern Oklahoma; and (4) the Ouachita Uplift geological province of southeastern Oklahoma.

Because actual core from well is not available, we made use of a block collected from outcrops in the Arbuckle Mountains in south-central Oklahoma along the I-35 in north of Carter County in the Arbuckle Uplift geological province, where Morgan (2014) has identified it as sections of the lower Arbuckle Group. Moreover, for the outcrops along the road where highway construction exposed the rocks, the rock was not highly weathered and more closely resembled the OPIC cores (Morgan and Murray 2015). The collected block is shown in Fig. 3-4.

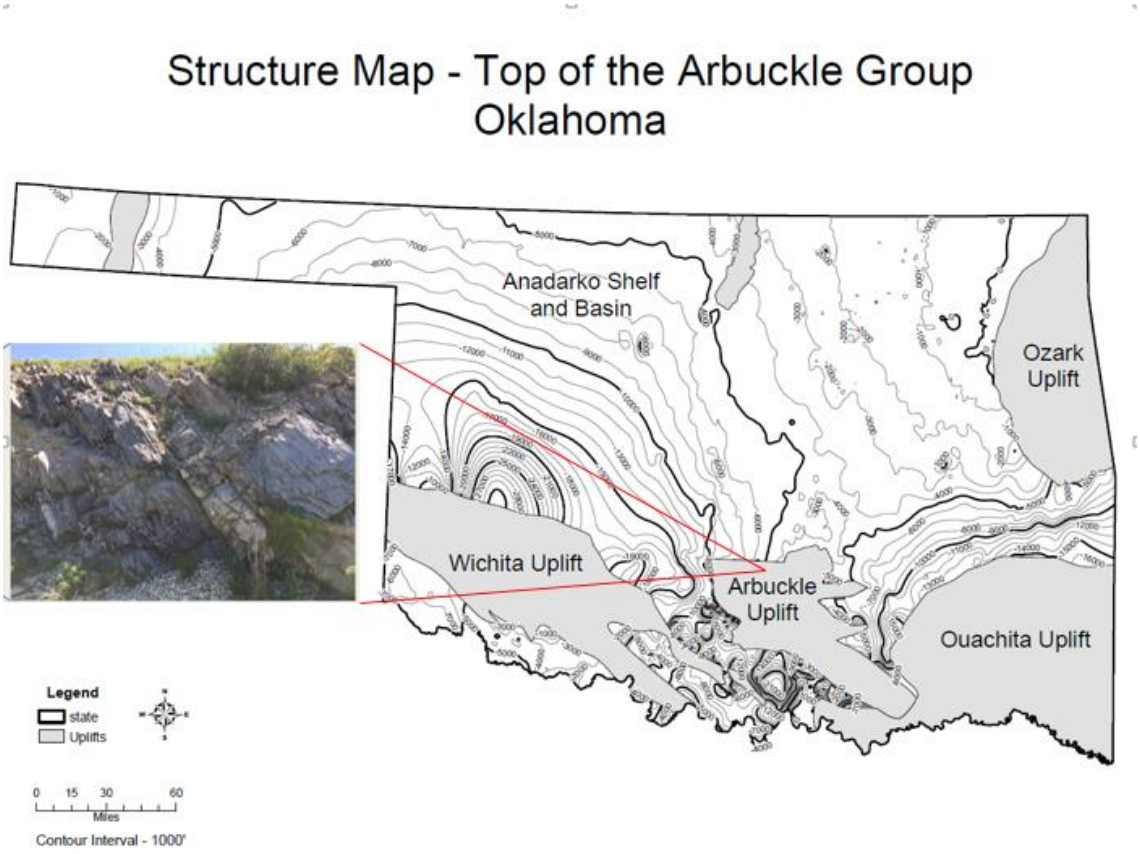

Fig. 0-1 Top of the Arbuckle Group Oklahoma (map from Oklahoma Geological Survey)

Crystalline basement of Oklahoma

In geology, *basement* refers to the rocks below a sedimentary platform. Generally, the basement rocks are crystalline (igneous and metamorphic). The crystalline basement of Oklahoma consists of various Cambrian and Precambrian rocks, including granite, gabbro, basalt, rhyolite and many others. Many crystalline rocks, such as granites and basalts are commonly used as building stones. Thus, many types of basement rocks are available in local quarries taking advantages of construction industry in Oklahoma. Two

types of crystalline basement rocks have been collected for the study purposes - Troy granite and Roosevelt Gabbro.

Basement rocks of Precambrian age are exposed in only two parts of Oklahoma. The major one is the eastern Arbuckle Mountains, as shown in Fig. 3-2 (Bickford and Lewis 1979). The Troy granite used in our study was collected from the quarry operated by Martin-Marietta Material Co. The location where the sample was collected is marked by a red star in the figure.

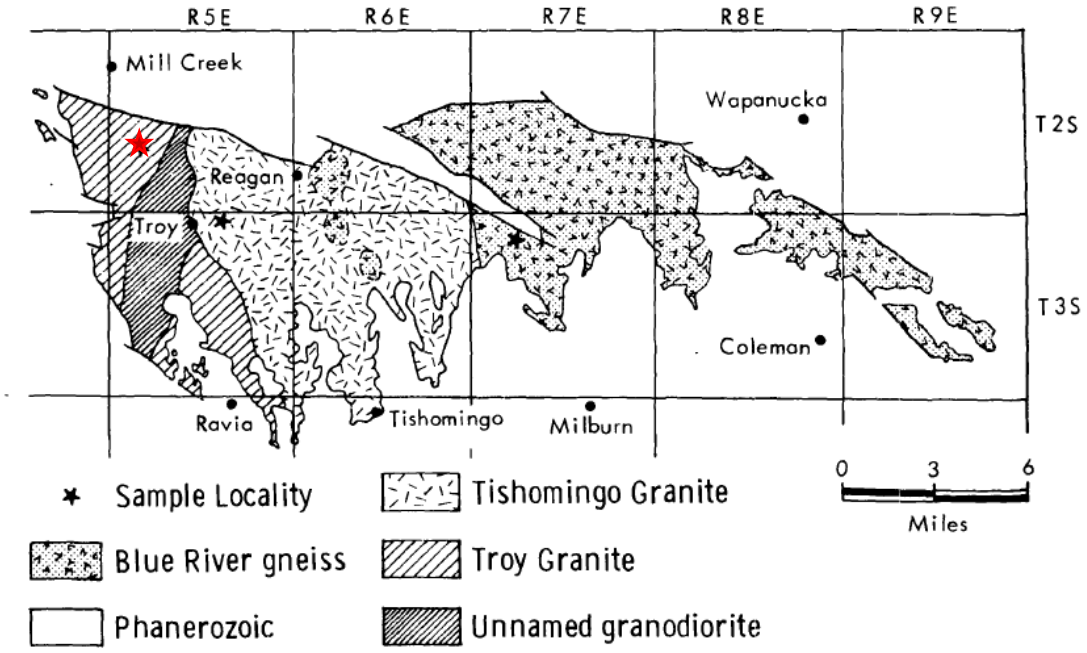

Fig. 0-2 Map of Oklahoma showing locations of exposures of Precambrian rocks (Bickford, 1979)

The second type of basement rock used in our study is the Cambrian Roosevelt gabbro. The sample was collected from the Wichita Mountains area close to the Meers fault. Fig. 3-3 shows the locations where the Roosevelt gabbro located. The sample of our testing

was collected from the quarry operated by Dolese Bros Co. Both basement samples were extracted from 50 to 100 feet depth of underground with minimal weathering.

The collected blocks are shown in the Fig. 3-4.

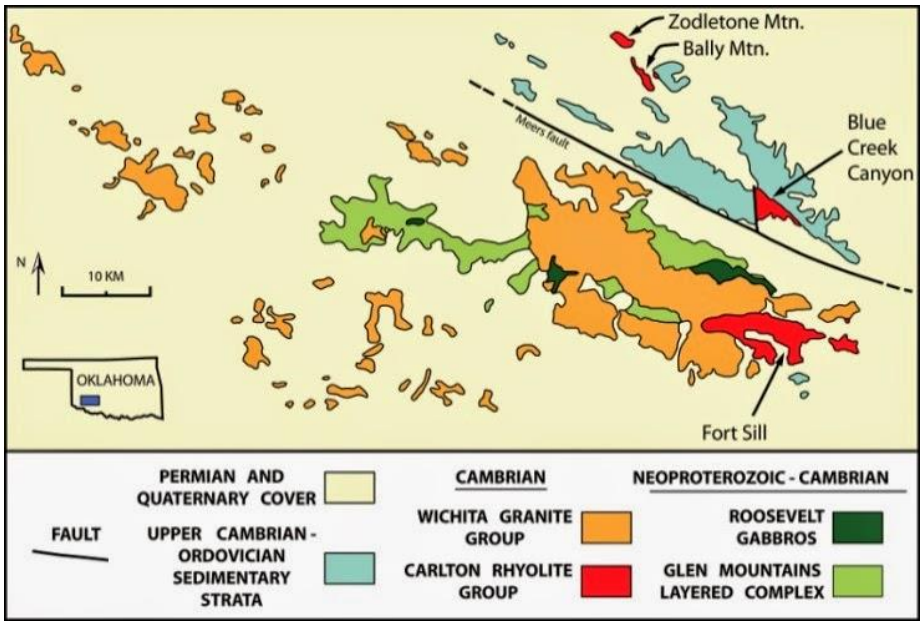

Fig. 0-3 Geological map of the Wichita Mountains (Powell et al., 1980 modified by Hansen et al., 2011)

Fig. 0-4 Samples collected from Arbuckle group and the basement

3.2 Rock Sample Preparation

Although the rock blocks were extracted from zones with minimal weathering, any weathered sections were first removed to expose a relatively fresh surface (about 0.5 inch thickness of exposed side on the block of Arbuckle Group was removed). Then, multiple right circular cylindered specimens were extracted using the *Cincinnati Bickford Super Service* drill with one-inch-inner-diameter diamond core bit. Specifically for the block of lower Arbuckle Group, the sedimentary bedding planes can be visually observed. Eighteen cylindered specimens were extracted from perpendicular, parallel and with 45° angle with respect to the bedding planes direction.

After coring, samples were subjected to further trimming to fulfill the standards of the testing, including cutting, grinding, and drying. The machine used for end surface treatments is *Brown & Sharpe 818 Micromaster®* surface grinder. And they were put in *FisherScientific Isotemp® Model 281A* vacuum oven for 8 hours before setting up to ensure dried conditions. The samples were prepared according to the standards listed in below, based on suggestions of: (1) *Standard Test Methods for Compressive Strength and Elastic Moduli of Intact Rock Core Specimens under Varying States of Stress and Temperatures (ASTM D7012-14(2014);* and (2) *ISRM: Suggested Methods for Determining the Strength of Rock Materials in Triaxial Compression: Revised Version (1983):*

- The specimens for each sample shall be selected from cores representing a valid average of type of rock under consideration, usually achieved by visual observation of mineral constituents, grain size and shape, partings and defects;

- Test specimens shall be right circular cylinders having a length to diameter ratio of between 2.0 and 3.0 to avoid the pressure cone phenomenon;
- The ends of the specimens shall be cut and ground parallel to each other and at right angles to the longitudinal axis;
- The ends of the specimen shall be flat to ±0.01 mm and shall not depart from the perpendicular to the longitudinal axis of the specimen by more than 0.001 radian;
- The sides of the specimen shall be smooth and free of abrupt irregularities and straight to within 0.3 mm over the full length of the specimen;
- The use of capping materials or end surface treatments other than machining is not permitted.

The picture was taken for each specimen before any testing, as shown in Fig. 3-5 and Fig. 3-6. Note that, in Fig. 3-5, samples #1 - #6 were extracted along the direction that perpendicular to the bedding planes; #7 - #12 were extracted with 45° angle with respect to the beddings; and #13 - #18 were along the direction that parallel to the beddings.

In Fig. 3-6, the samples in first row are Troy granite, and the second are Roosevelt Gabbro. Sample #22, #23 and #24 were intentionally extracted with clear weak planes intersected, marked with red dot line in the figure. The results of the defective specimens will be compared to the normal specimens in order to research the effect of pre-existing weak planes on rock properties.

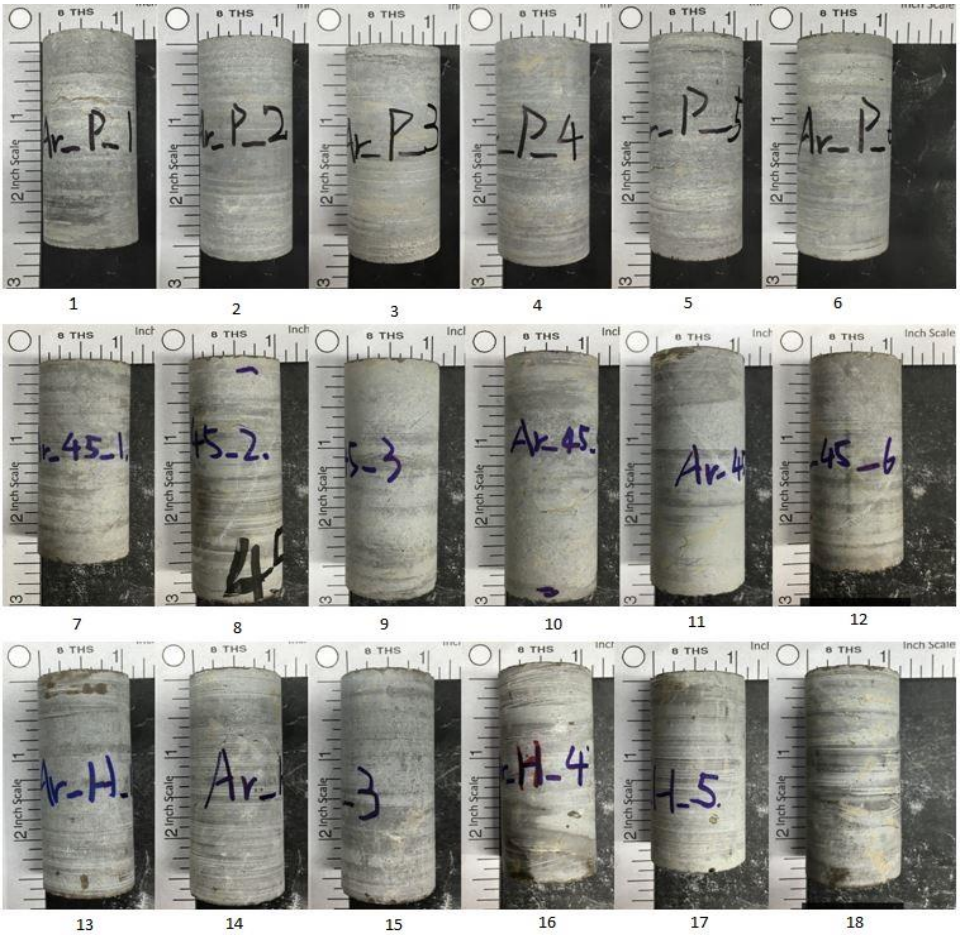

Fig. 0-5 Prepared specimens from lower Arbuckle Group

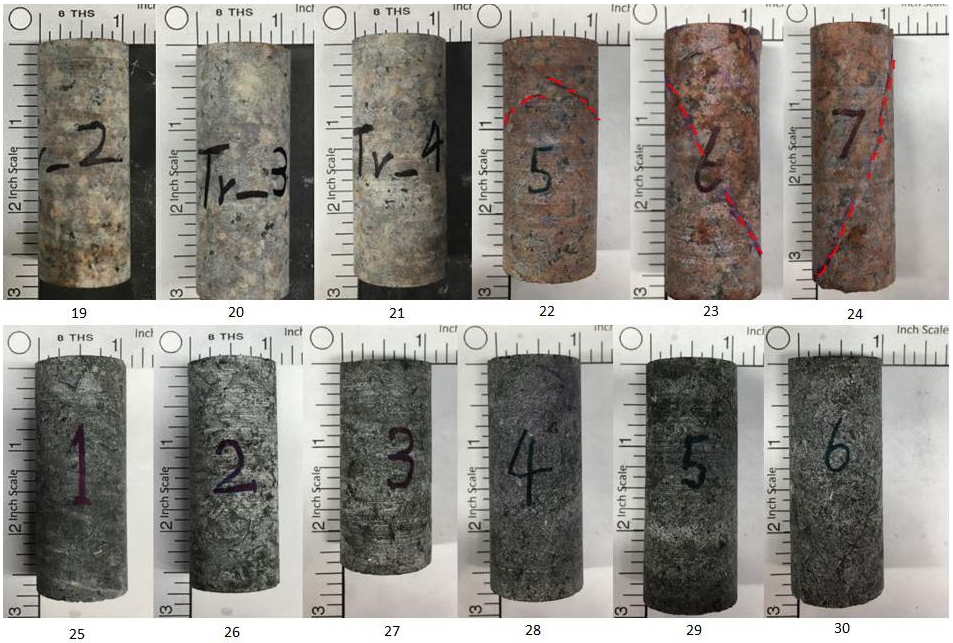

Fig. 0-6 Prepared specimens from basement

3.3 Sample Characterization

The important parameters and index properties of each cylinder specimen are measured and summarized in the Table. 3.1, and Table 3.2, including its dimensions, weight, density, and the hardness index. The value of hardness index is obtained by the *Procerq Portable Material Hardness Tester*. The measured hardness indexes are only used for qualitative comparison purposes among the tested cylindered samples due to the general measurement using such technique require a minimum weight of sample to be 5 Kg.

Table 0.1 Basic parameters of prepared specimens-Arbuckle Group

Sample Number	Direction	Length (mm)	Diameter (mm)	Weight (g)	Density (g/cc)	Hardness Index
1	Perp.	55.36	25.13	73.36	2.67	627
2	Perp.	57.56	25.14	76.6	2.68	648
3	Perp.	55.82	25.13	74.19	2.68	664
4	Perp.	57.63	25.13	76.47	2.68	661
5	Perp.	57.35	25.13	76.31	2.68	652
6	Perp.	56.55	25.13	75.08	2.68	648
7	45°	54.23	25.24	72.74	2.68	662
8	45°	65.28	25.24	87.44	2.68	661
9	45°	61.89	25.24	82.97	2.68	677
10	45°	63.54	25.23	85.17	2.68	659
11	45°	61.75	25.24	82.62	2.67	652
12	45°	55.66	25.24	74.72	2.68	656
13	Parallel	59.40	25.27	79.69	2.67	618
14	Parallel	59.69	25.27	79.79	2.67	651
15	Parallel	58.30	25.28	78.02	2.67	654
16	Parallel	54.48	25.23	72.83	2.68	667
17	Parallel	54.34	25.22	72.68	2.68	643
18	Parallel	51.91	25.24	69.53	2.68	645

Table 0.2 Basic parameters of prepared specimens-basement

Sample Number	Rock Type	Length (mm)	Diameter (mm)	Weight (g)	Density (g/cc)	Hardness Index
19	Granite	62.62	25.28	82.07	2.61	843
20	Granite	63.92	25.29	84.02	2.62	857
21	Granite	61.12	25.27	80.17	2.62	839
22	Granite	59.89	25.29	78.80	2.62	798
23	Granite	67.41	25.24	88.31	2.62	869
24	Granite	75.57	25.26	98.96	2.61	839
25	Gabbro	62.19	25.20	88.33	2.85	776
26	Gabbro	61.86	25.15	87.78	2.86	725
27	Gabbro	54.02	25.18	77.68	2.89	740
28	Gabbro	60.96	25.26	85.21	2.79	778
29	Gabbro	63.67	25.24	90.23	2.83	740
30	Gabbro	62.34	25.27	87.45	2.80	766

Powder X-ray Diffraction (XRD) minerology analysis has been performed on the samples which extracted from the same block for each type of rock, as summarized in table 3.3 below. According to the XRD minerology, the Troy granite consist of large amount of feldspar (62%) and quartz (32%), the lower Arbuckle Group sample is dominated by Calcite (91%), and the Roosevelt gabbro is dominated by feldspar (94%).

Table 0.3 XRD minerology of each type of rock

	The Arbuckle Group	**Troy Granite**	**Roosevelt Gabbro**
Quartz	9%	32%	0
Plagioclase	0	27%	82%
K-Feldspar	0	0	0
Calcite	91%	0	0
Dolomite	0	0	0
Pyrite	0	0	0
Chlorite	0	2%	0
Halloysite	0	0	0
Mica	0	4%	1%
Illite	0	0	0
Kaolinite	0	0	3%
Smectite	0	0	0
Vermiculite	0	0	0
Total Clay	0	6%	4%
Total Feldspar	0	62%	94%
Total Carbonate	91%	0	0
Other	9%	32%	2%

Petrographic thin sections were also made for each type of the rock. Fig. 3-7 and Fig. 3-8 show the thin section pictures of samples from the Arbuckle Group and two types of crystalline basement rocks, respectively.

According to the thin sections in Fig. 3-7, for Arbuckle Group samples, the formation are dominated by fine-grained lime-mud matrices. Fractures and small vugs are widely distributed, filling or lining with dolomite or calcite cements. There are also small opened fractures exist, as shown in the center of picture 3. Picture 3 and 4 indicate uneven distribution of the materials as in their left parts, where larger rounded particles concentrate and provide interpartical porosities. Also exist areas as in picture 5, where

dominated by fossils and silt materials with carbonate cements in some parts. As a conclusion, the Arbuckle samples contain complex micro structures with various sized lime-mud matrices and unevenly distributed vugs, fractures and cements. The porosity is provided by vugs, fractures, as well as interpartical pores in some parts.

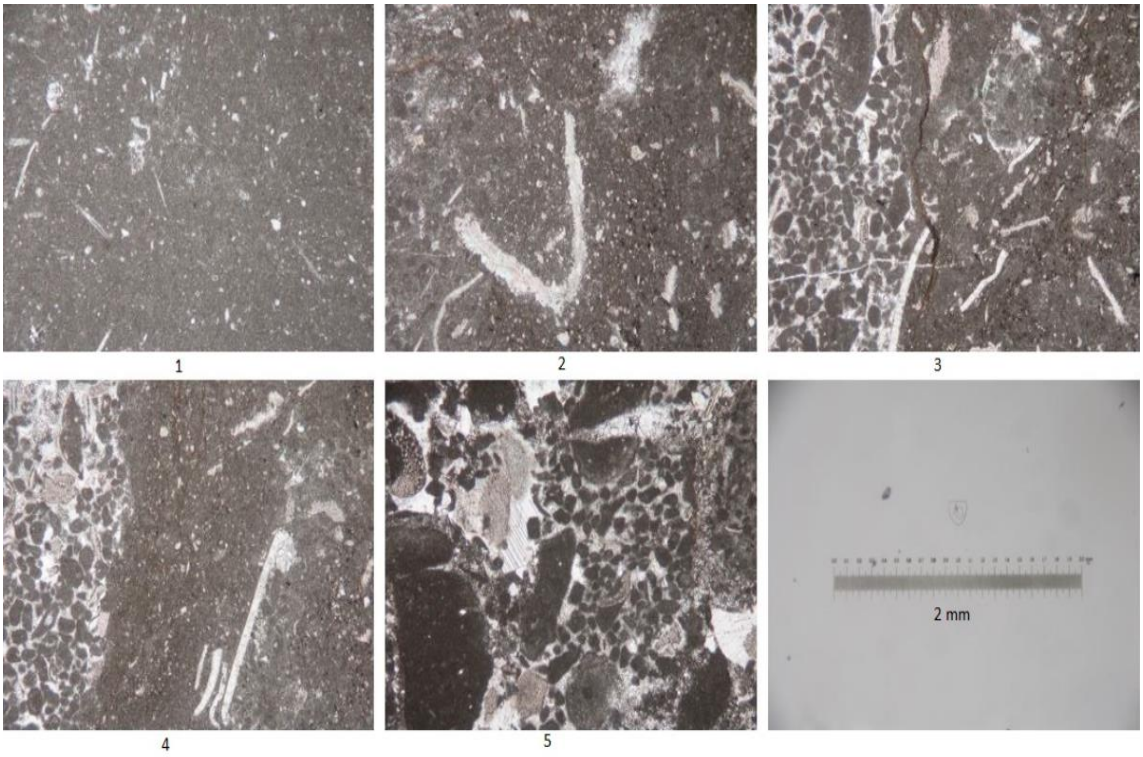

Fig. 0-7 Petrographic thin sections for Arbuckle samples

Fig. 3-8 shows thin-section views of the basement rocks. Images (1) and (2) are for Troy granite, and images (3) and (4) are for Roosevelt gabbro. As shown in the figures, Troy granite has medium- to coarse-grained, and the Roosevelt gabbro is coarse-grained. Both basement rocks show crystalline textures. Crossed polarized light (xpl) shows quartz (Q) and feldspar (F) occupy most of the thin section area of the Troy granite (lamellar twinning in some grains in (1) and (2)), and feldspar is dominant in the Roosevelt gabbro

(lamellar twinning in almost all grains in (3) and (4)) thin section. Most grains we observed in thin sections of Roosevelt gabbro are the plagioclase.

The permeability and porosity of those rocks should be extremely small for both types of basement rocks as the grains are tightly attached.

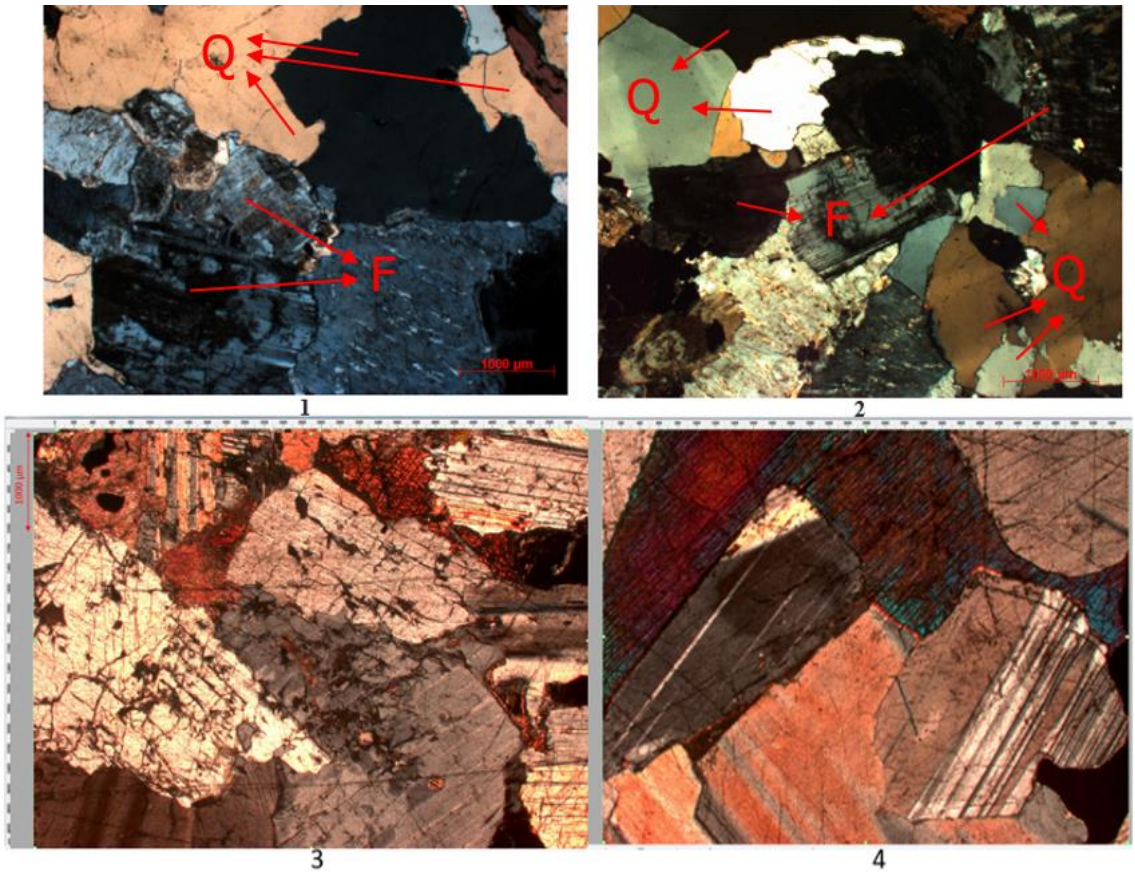

Fig. 0-8 Petrographic thin sections for basement samples

At last, the porosity of each type of rock has been estimated using the gas expansion method. The measurements were carried out on four 1-inch-diameter cylindered samples extracted from the same rock blocks where the tested specimens were extracted: two from the lower Arbuckle Group block, one from Troy granite, and one from the Roosevelt gabbro. The measured porosity for the two Arbuckle Group samples are 2.56% and 2.93%; 2.11% for the Troy granite, and 1.84% for the Roosevelt gabbro. However, the

system is designed for higher porosity rocks (greater than 1%) and has high system error (about $\pm$1% porosity). Thus, the obtained porosity values of our samples should only be used for qualitative comparison purposes. The actual porosity of the three types of rock should be smaller than the measured values above.

Chapter 4 Characterization of Intact Rock Geomechanical Properties

4.1 Experimental setup

Characterization intact rock properties require experimental setup for both triaxial compression test and ultrasonic measurements. The test system (Fig. 4-1) set up consist of:

- An MTS Model 816 test system with a force capacity of 1048 kN force with an MTS 20.000 psi pressure vessel
- A computer with MTS series 793™ controller software for test control and data acquisition
- A HP 8116A pulse function generator
- An Olympus voltage preamplifier
- A Tektronix MDO3022 mixed domain oscilloscope
- A computer with Tektronix OpenChoice Desktop software for dynamic data recording

Additionally, as shown in Fig. 4-2 and Fig. 4-3, the sample setup consists of:

- A pair of GCTS dynamic platens with ultrasonic transducers (P, S1, and S2: 156 Hz – 40 MHz, 16bit)
- Two Linear Variable Differential Transformer (LVDT) extensometers for axial displacement measurement
- A Circumferential (LVDT) Extensometer Chain measuring radial displacement

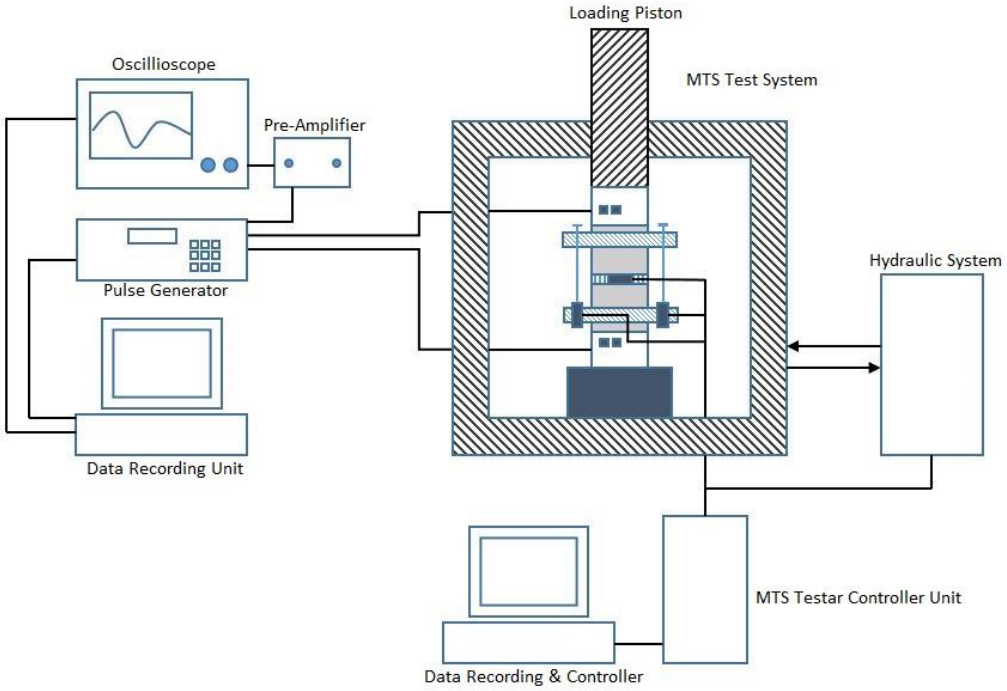

Fig. 0-1 Schematic diagram of equipment setup

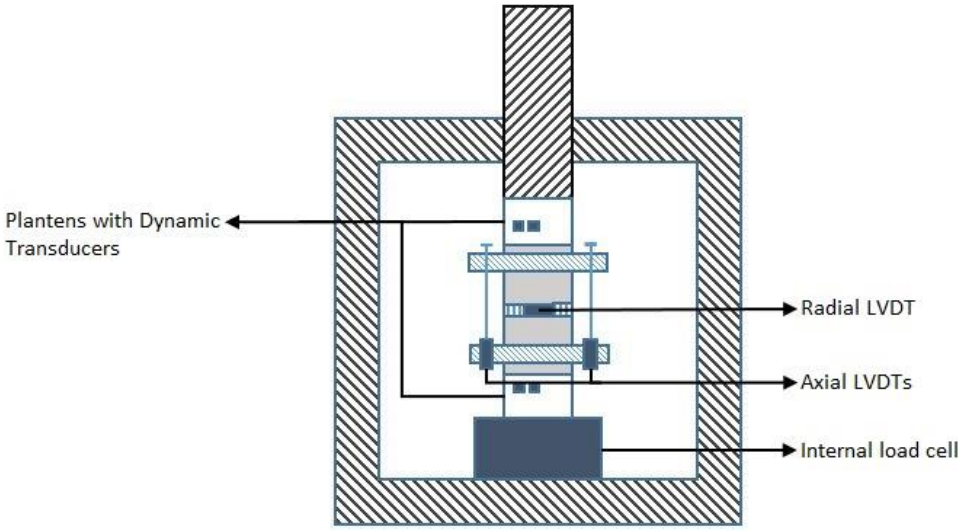

Fig. 0-2 Schematic diagram of sample setup

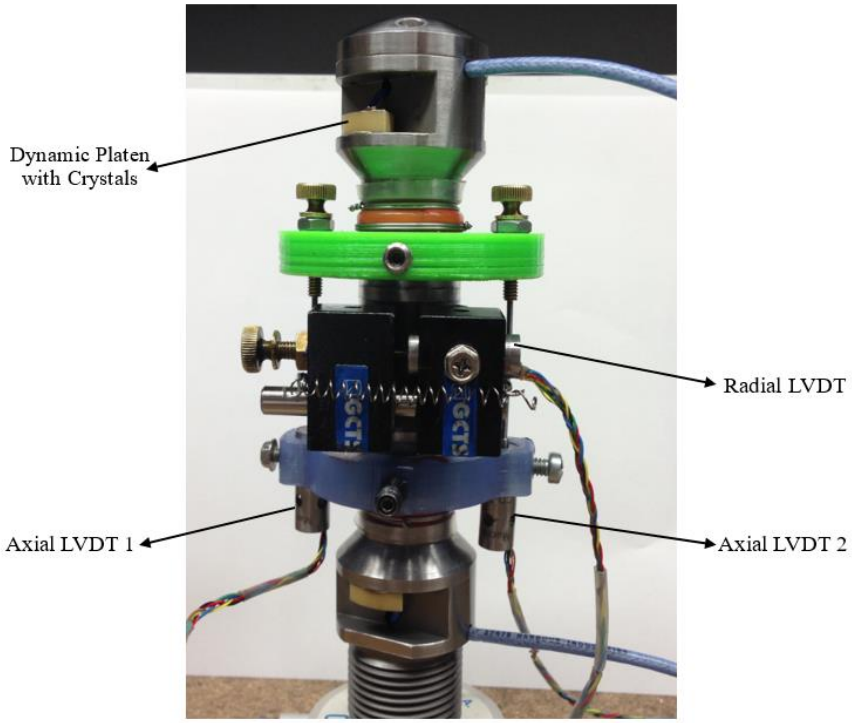

Fig. 0-3 Picture of sample setup

To setup the sample, a pair of GCTS dynamic platens are placed on top and bottom of the sample. Fig. 3-4 is the sample after the completing the following steps: (1) place the platens with dynamic transducers o top and bottom of the sample; (2) install polyeofin tubing jacket (using heat shrinking) to provide isolation from the confining fluid; (3) clamp the ends of the jacket on the silicone tape strips with stainless steel wires; (3) install two fully calibrated LVDTs measuring axial displacements are fixed in a pair of 3D-printed PLA material rings in perpendicular to longitudinal axis of the sample; (4) attach a third calibrated radial displacement measuring LVDT to a chain which was wraps around the sample at its center. The calibration information of the three LVDTs will be detailed in the Appendix. C. When the sample is ready to be tested, it is placed into the MTS triaxial cell on top of the internal load cell, and then loading procedures begin.

4.2 Testing Procedures

After the sample was properly put inside the cell, the connections for three LVDTs, load cell, and dynamic measurement system shall be completed. The readings of 3 LVDTs and the load cell should be adjusted to the initial position (all readings should be close to 0). And, the ultrasonic wave form shall be displaced on the oscilloscope. Once the signals of each connection described above have been checked, the MTS series 793™ controller software will be used to control the test step by step with the following process:

1) The pressure vessel is closed and the bolts on the cell are tightened to ensure good sealing. Then the vessel is filled with hydraulic oil
2) Confining pressure is increased to the first-stage hydrostatic testing pressure
3) The ultrasonic waves are displayed on the oscilloscope. When the hydraulic pressure becomes stable, the wave forms are recorded with Tektronix OpenChoice Desktop software in the computer
4) Apply a small axial load (usually 1 MPa) to the sample. By applying this load, the contact between the piston and the sample is established
5) The axial load is increased at a constant axial strain rate to the point at which the volumetric strain stop increasing with the increasing axial stress (inflection point) while confining pressure is held constant. The inflection point can be read in the real-time stress-strain plot during the testing
6) If the test stage in the non-failure stage, lower the axial stress until a hydrostatic state is reached again. Then, increase the confining pressure to the next-stage hydrostatic testing pressure and repeat step 3;

7) If the test stage in the final failure stage, unload axial stress to reach a hydrostatic state, change the confining pressure to the required value for the failure stage
8) Increase the axial load at a constant rate of strain until the specimen fails while the confining pressure is held constant
9) Reduce axial stress to the initial hydrostatic condition after sample fails, then reduce the confining pressure to zero and disassemble sample

Unless noted otherwise, the axial strain rate is $5 \times 10^{-6}\ strain/s$ and is kept same in every stage of each test.

4.3 Dynamic testing

4.3.1 Ultrasonic Wave Velocities

Using an ultrasonic sampling rate of 250 KHz, the measured compressional and shear wave velocities of 18 samples from the Arbuckle Group are plotted in the Fig. 4-4 and Fig. 4-5 in terms of effective confining pressures, respectively. The sampling directions are distinguished by different marks: **circles** for perpendicular samples (number #1 - #6); **crosses** for 45° samples (number #7 - #12); and **triangles** for parallel samples (number #13 - #18). The same color and data marker schemes are used for all confining pressures.

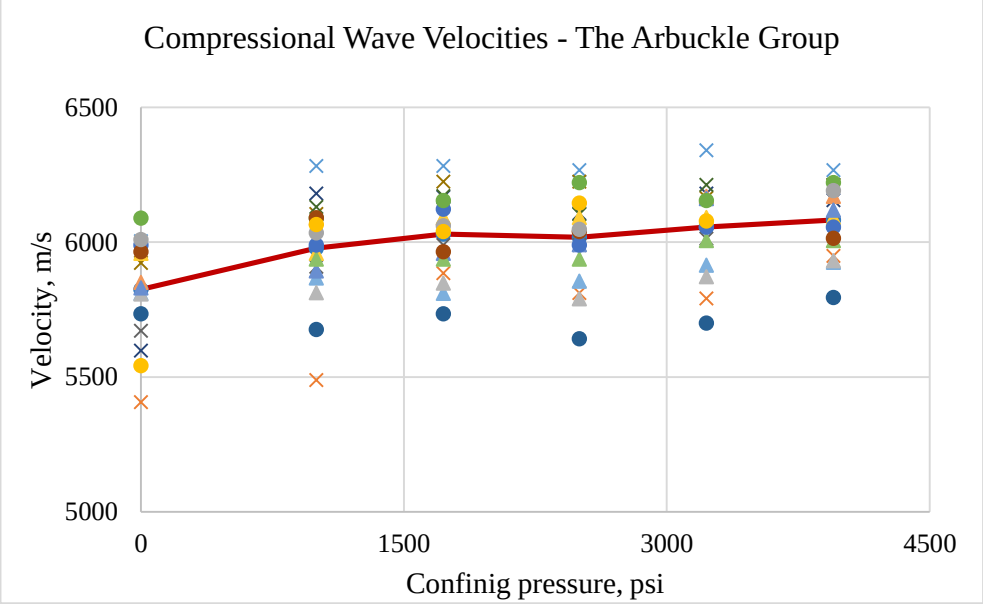

Fig. 0-4 P-wave velocities for Arbuckle samples

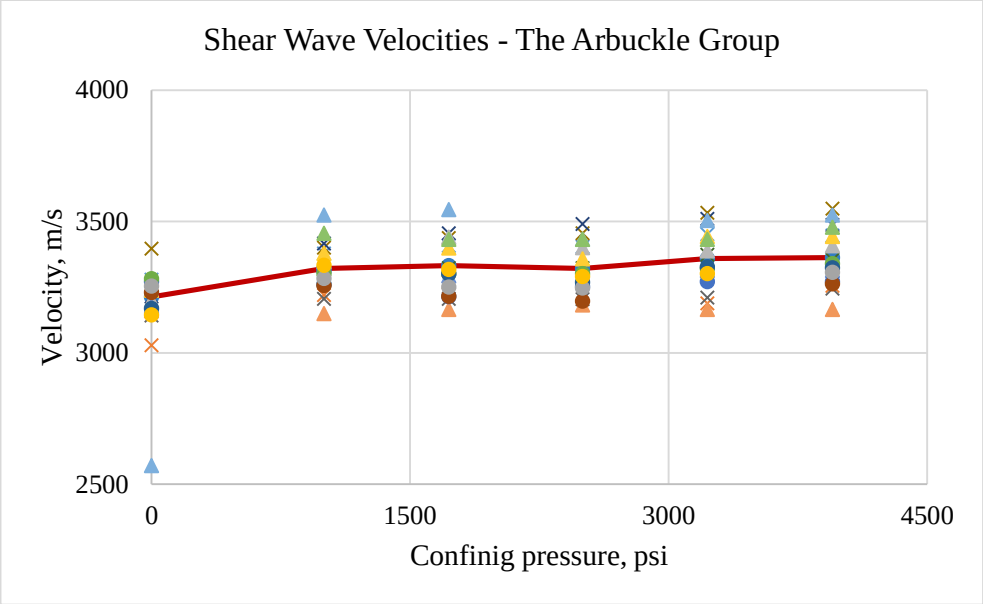

Fig. 0-5 S-wave velocities for Arbuckle samples

As shown in the Fig. 4-4 for the compressional wave, the velocities at zero confining pressure vary between 5407.31 m/s to 6089.58 m/s with an average value of 5824.55 m/s. As confining pressure increases, the values first slightly increased, then become stable at effective confining pressures above 1725 psi. At the highest applied confining pressure of 3950 psi, the compressional wave velocities are within the range of 5794.60 - 6268.11 m/s with an average of 6081.96 m/s. The line in the figure represents the average speed at different confining pressures.

A similar trend can be observed in Fig. 4-5 of shear wave velocities. At zero confining pressure, an abnormal low value was obtained as 2570.60 m/s, which has been omitted for calculating average velocities. The abnormal low value could be due to poor surface contact and/or opened micro fractures at zero confining pressure. The average shear velocity is 3212.48 m/s at zero confining pressure and 3362.97 m/s at the highest applied confining pressure.

The velocity figures imply the tested Arbuckle Group samples are well cemented and dense. And, because it is hard to distinguish the data from samples of different directions, the anisotropy appears insignificant.

For the crystalline basement, only nine samples were subjected to ultrasonic measurements: six Roosevelt gabbro (sample 25-30) and three Troy granite (sample 22-24). For those samples, the measurements at zero confining pressure suffered from large signal noises which might be caused by poor surface contact. Thus, due to the large uncertainties at zero confining pressures, most measurements were only performed at four confining pressure stages: 1000, 1500, 2500, 3500 psi. Shown in the Fig. 4-6 and Fig. 4-7, the **circles** represent the gabbro samples, and the **crosses** represent the granite samples.

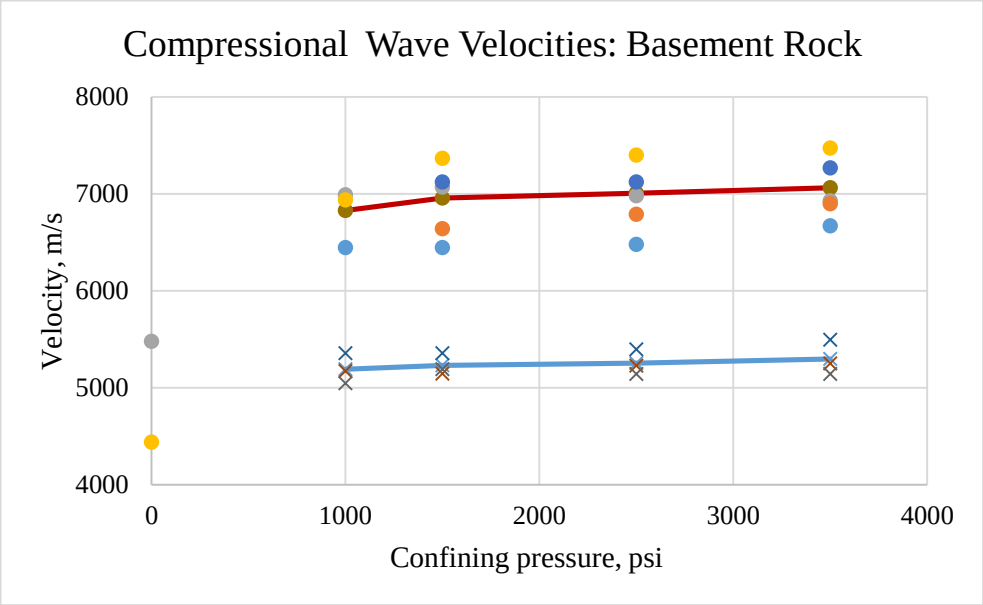

Fig. 0-6 P-wave velocities for basement samples

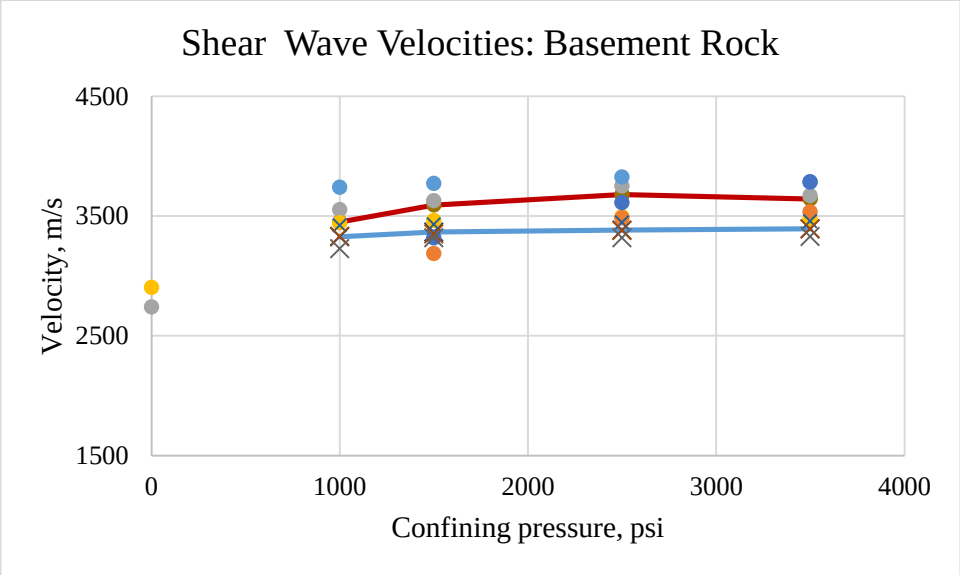

Fig. 0-7 S-wave velocities for basement samples

Although both of these rocks originate from the basement, the compressional wave velocities are distinguished between two different types. The gabbro samples have higher compressional wave speed, with an average of 7060.95 m/s at 3500 psi confining pressure, compared with 5295.31 m/s for the granite. The average values at different confining pressures for gabbro and granite are shown in the figure with red and blue line, respectively. On the other hand, the shear wave velocities of these two rock types show no such differences, as the average speed at 3500 psi confining pressure is 3583.03 m/s for gabbro and 3393.86 m/s for the granite. And in general, very small or no pressure dependence was observed for the measured velocities of the basement samples once the pressure reached 1000 psi. According to Schön (2011), there is always a good correlation between velocity and density. Moreover, the ultrasonic velocities decrease with increasing fracturing or porosity, and increase from felsic to mafic types. From the characterization in Chapter 3, the Roosevelt gabbro has the highest density, lowest

porosity, and highest feldspar contents. Thus, the high ultrasonic velocity of Roosevelt gabbro can be explained.

As a conclusion, the Roosevelt gabbro has the highest compressional and shear wave velocities among all three types of samples. The rock types can be easily distinguished from P-wave velocities. The S-wave, however, do not vary much, especially for the Arbuckle Group samples and Troy granite which have very similar S-wave velocities. For each type of rock, no obvious pressure dependence is observed except for it from zero to the second least pressure stage. The small jump between the values at zero confining pressure maybe caused by bad surface contact or opened micro fractures. Thus, the dynamic moduli calculation would not include the velocities measured at zero pressures.

4.3.2 Dynamic moduli

Equation (2.5) – (2.8) are used to determine the dynamic moduli, or dynamic elastic constants: Young's modulus (E_{dyn}), Poisson's ratio (ν_{dyn}), Bulk modulus (K_{dyn}) and Shear modulus (G_{dyn}) from obtained compressional and shear wave velocities of tested samples. Depending on the signal quality, the uncertainties up to ± 0.2 μ seconds and ± 0.5 μ seconds for compression and shear wave travel time exist. These corresponded to uncertainties in elastic parameters are as large as 10 %, which usually exists at zero confining pressure. While at higher effective stress, the signal quality is usually much better, and the shear wave reading uncertainties quickly decrease to ± 0.2 μ seconds, and provide more reliable results at high confining pressures. The uncertainties of elastic parameters are about 5% at high confining pressures.

Table 4.1 concludes the determined dynamic moduli for 27 tested samples. The velocities used to calculate the dynamic moduli are the average values at non-zero confining pressures. As the Roosevelt gabbro samples have much higher density and wave velocities compared with others, the calculated elastic constants are extremely high, even over 100 GPa for sample #27. The Arbuckle samples have similar dynamic Young's moduli with the Troy granites; but the Poisson's ratio of the Troy granite is much lower than other types of rock.

Table 0.1Dynamic elastic constants for 27 samples

Sample Number	**Density (g/cc)**	E_{dyn} **(GPa)**	ν_{dyn}	K_{dyn} **(GPa)**	G_{dyn} **(GPa)**
1	2.67	73.61	0.29	59.58	28.44
2	2.68	76.32	0.30	62.75	29.42
3	2.68	72.80	0.25	48.54	29.12
4	2.68	72.72	0.30	60.00	28.01
5	2.68	74.39	0.30	60.94	28.69
6	2.68	75.77	0.29	59.98	29.38
7	2.68	80.78	0.29	64.25	31.30
8	2.68	71.54	0.27	52.19	28.13
9	2.68	71.89	0.30	59.39	27.69
10	2.68	82.16	0.27	59.41	32.36
11	2.67	81.55	0.27	58.35	32.18
12	2.68	76.87	0.29	62.31	29.69
13	2.67	80.30	0.22	48.40	32.82
14	2.67	70.47	0.32	64.21	26.75
15	2.67	76.75	0.25	50.34	30.80
16	2.68	78.90	0.27	57.19	31.06
17	2.68	74.94	0.29	58.45	29.13
18	2.68	79.54	0.25	52.93	31.83
22	2.62	71.84	0.16	35.12	30.99
23	2.62	67.58	0.14	31.26	29.65
24	2.61	65.15	0.15	30.82	28.38
25	2.85	99.72	0.31	88.60	37.99
26	2.86	93.20	0.35	106.18	34.43
27	2.89	102.89	0.25	67.40	41.30
28	2.79	87.90	0.33	84.30	33.14
29	2.83	98.25	0.33	98.97	36.81
30	2.8	93.20	0.36	110.76	34.27

4.3.3 Anisotropy of Arbuckle Group samples

Seismic anisotropy in underground sedimentary sequences is important to petroleum exploration and production and will affect the interpretation of seismic data. The Thomsen parameters, ε, γ, δ are widely used to describe the long offset effect and the shear wave effect and the short offset effect in an anisotropy material. Taking advantage of the availability of Arbuckle Group samples from 3 different directions, the velocities required to calculate anisotropy were obtained.

Using the measure compressional and shear wave velocities in the perpendicular, parallel and 45° angle directions, we determined $V_p(0°)$ and $V_{SH}(0°)$(the average compression and shear wave speed of specimens that perpendicular to bedding planes), $V_p(90°)$ and $V_{SH}(90°)$, (the average compression and shear wave speed of specimens that parallel to bedding planes), and $V_p(45°)$, (the average compression wave speed of specimens that have $45°$ angle respect to bedding planes).

Hence, the stiffness matrices of the Arbuckle block at various pressures were calculated and are shown in Table 4.2. And, Table 4.3 summarizes all three Thomsen's anisotropy parameters and the calculated dynamic Young's modulus using velocities from different stages. The calculation of Young's modulus of the block was made using average ultrasonic velocities of all samples in each direction.

Table 0.2 Stiffness matrix at different pressure

Effective stress, MPa (psi)	Elastic Modulus (GPa)					
	c11	c33	c44	c66	c12	c13
0 (0)	91.65	92.87	27.86	25.22	41.21	27.32
7 (1000)	94.02	96.14	29.01	30.14	33.74	40.77
12 (1725)	94.95	96.84	28.58	30.57	33.82	47.59
17 (2500)	94.93	96.88	28.46	30.00	34.92	45.46
22 (3225)	97.52	96.34	29.26	30.48	36.57	44.98
27 (3950)	97.68	98.21	29.18	30.74	36.21	45.97

Table 0.3 Anisotropy parameters and dynamic modulus

Effective stress MPa (psi)	Anisotropy parameters			Dynamic Young's Modulus (GPa)	
	ε	γ	δ	E3 Ver.	E1 Hor.
0 (0)	-0.01	-0.05	-0.10	81.64	70.45
7 (1000)	-0.01	0.02	0.03	70.13	73.21
12 (1725)	-0.01	0.03	0.09	61.66	70.05
17 (2500)	-0.01	0.03	0.06	65.05	71.09
22 (3225)	0.01	0.02	0.08	66.16	73.35
27 (3950)	0.00	0.03	0.07	66.65	73.33

Thomsen has presented measured anisotropy parameters for different types of sedimentary rocks, including sandstone, shale, mudstone, siltstone, and others (Thomsen, 1958). According to our results, all anisotropy parameters tend to be pressure independent and approach a specific value when the pressure increased over 1000 psi: $\varepsilon \approx 0$, $\gamma \approx 0.025$, and $\delta \approx 0.07$. Our measurements fall far below the average of the rocks of Thomsen's research. The obtained parameters represents an extremely small level of anisotropy for the block of the lower Arbuckle Group. Moreover, from the calculated stiffness matrix parameters, the average dynamic Young's modulus were calculated for the entire block of Arbuckle Group as 64.88 and 71.96 GPa, for vertical and horizontal directions, respectively (average at non-zero confining pressures).

4.4 Multistage Triaxial Testing

From multistage triaxial testing, the static elastic properties such as Young's modulus and Poisson's ratio have been obtained at each confining pressure. In addition, the compressive strength and Mohr-Coulomb failure envelope have been estimated. Tables 4.4 - 4.8 in the following pages summarize all of the measured and calculated values for our samples. In those tables, the Mohr-Coulomb failure envelope of each sample is described by the coefficient of internal friction, $\tan\phi$, and cohesion of the rock, c, where ϕ is the internal friction angle, and c is the intercept of the failure envelop with vertical axis. The stress-stain curves and the Mohr-circles for each tested sample is include in the Appendix A and B.

From the results, all rock types tested have high Young's modulus, especially the Roosevelt Gabbro whose Young's modulus can be as high as more than 100 GPa. This value is close to the Titanium. The strongest rock is the Troy granite. For all three intact samples, the UCS values fall over 300 MPa. However, the for the granite samples that had pre-existing weak planes, the strength decreased more than 50% compared with the intact ones.

Although the ductile/ brittle failure behavior of rock has not been quantitatively measured, it can be revealed by the stress-strain plot of each sample. In general, a sudden linear post-peak curve represents a fast stress drop in brittle failure, the curved post-peak curve represents a relatively more ductile failure mode. The brittle/ductile failure behavior from the stress-strain plot for single tested sample is discussed in Appendix A where the plots are presented. According to the plots, both the Arbuckle and Troy granite samples have relatively brittle deformation behaviors in that sudden failure is observed

during the failure stages. On the other hand, the gabbro samples appear to be more ductile. The failures of those samples usually occurred gradually and with a residual strength.

Thus, in order to ensure a clear single fracture (for future joint testing), the axial strain rate were increased to 1.5×10^{-5} strain/s (the regular strain rate for the test is 5×10^{-6} strain/s) at the failure stages for some gabbro samples.

Table 0.4 Multistage triaxial test result - Arbuckle (1-6)

Sample No.	Confining Pressure (MPa)	Compressive Strength (MPa)	Estimated UCS (MPa)	Static Young's Modulus (GPa)	Static Poisson's Ratio	Cohesion (MPa)	Coefficient of internal Friction
1	3	209	188	57.49	0.26	41	0.92
	7	226		58.76	0.24		
	10	234		59.53	0.23		
	14	262		59.10	0.27		
	21	298		60.14	0.27		
2	3	221	206	61.02	0.26	38	1.17
	7	264		62.22	0.27		
	10	288		63.36	0.27		
	14	309		65.75	0.28		
	21	353		63.92	0.27		
3	3	236	214	65.41	0.26	40	1.16
	7	265		68.79	0.26		
	10	289		69.54	0.24		
	14	321		69.38	0.24		
	21	360		69.23	0.24		
4	3	262	237	70.81	0.28	48	1.05
	7	280		70.77	0.28		
	10	296		70.67	0.27		
	14	331		70.15	0.28		
	11	303		68.84	0.30		
5	3	196	176	70.84	0.25	32	1.18
	7	235		71.15	0.25		
	10	258		71.33	0.26		
	14	276		71.21	0.26		
6	3	222	215	71.53	0.24	46	0.95
	7	254		70.94	0.23		
	17	281		70.12	0.24		
	10	297		69.38	0.24		

Table 0.5 Multistage triaxial test result - Arbuckle (7-12)

Sample No.	Confining Pressure (MPa)	Compressive Strength (MPa)	Estimated UCS (MPa)	Static Young's Modulus (GPa)	Static Poisson's Ratio	Cohesion (MPa)	Coefficient of Friction
7	3	211	193	71.99	0.31	45	0.83
	7	228		72.42	0.31		
	10	237		72.92	0.30		
	14	248		71.10	0.32		
	21	292		71.60	0.30		
8	3	101	86	53.41	0.29	17	1.07
	7	134		56.90	0.28		
	10	160		59.84	0.29		
	14	172		62.35	0.27		
	21	215		60.42	0.28		
9	3	223	209	62.34	0.30	51	0.80
	7	242		61.25	0.29		
	10	254		61.28	0.29		
	14	266		62.59	0.28		
	21	299		61.43	0.30		
10	3	158	141	64.32	0.26	31	0.94
	7	184		63.90	0.26		
	10	197		66.15	0.26		
	14	205		72.01	0.24		
	21	256		63.80	0.29		
11	3	158	149	57.50	0.25	29	1.08
	7	200		59.53	0.25		
	10	227		62.00	0.27		
	14	244		63.99	0.29		
	21	275		60.82	0.25		
12	3	202	178	64.04	0.30	35	1.05
	7	220		61.21	0.31		
	10	239		61.19	0.31		
	14	264		61.92	0.30		
	21	309		63.70	0.30		

Table 0.6 Multistage triaxial test result - Arbuckle (13-18)

Sample No.	Confining Pressure (MPa)	Compressive Strength (MPa)	Estimated UCS (MPa)	Static Young's Modulus (GPa)	Static Poisson's Ratio	Cohesion (MPa)	Coefficient of Friction
13	7	220	180	82.67	0.30	37	1.00
	10	239		79.44	0.29		
	14	261		78.94	0.28		
	21	301		78.22	0.28		
14	3	167	150	76.50	0.29	29	1.07
	7	198		74.24	0.30		
	10	221		73.45	0.30		
	14	239		72.46	0.30		
	21	281		70.89	0.31		
15	3	172	160	81.81	0.30	31	1.10
	7	211		81.42	0.31		
	10	238		79.51	0.31		
	14	259		78.23	0.31		
	21	292		74.71	0.31		
16	3	214	198	75.56	0.30	43	0.99
	7	235		75.78	0.27		
	10	252		75.17	0.27		
	5	227		73.49	0.28		
17	3	146	131	73.99	0.32	28	0.98
	7	171		77.97	0.33		
	10	193		80.44	0.34		
	14	214		79.84	0.34		
	21	244		79.35	0.34		
18	3	132	114	82.72	0.25	22	1.11
	7	162		85.50	0.27		
	10	187		82.85	0.25		
	14	210		81.06	0.25		
	21	250		82.21	0.24		

Table 0.7 Multistage triaxial test result – Troy Granite (19-24)

Sample No.	Conf. Pressure (MPa)	Compr. Strength (MPa)	Estimated UCS (MPa)	Static Young's Modulus (GPa)	Static Poisson's Ratio	Cohesion (MPa)	Coefficient of Friction
19	3	350	322	63.29	0.23	57	1.23
	7	379		65.36	0.25		
	10	401		62.54	0.25		
	17	460		64.40	0.24		
	24	514		64.19	0.27		
20	3	391	366	73.08	0.24	62	1.17
	7	429		71.71	0.24		
	10	463		73.77	0.23		
	17	517		73.08	0.23		
	28	608		73.08	0.26		
21	3	407	387	67.64	0.25	66	1.16
	7	446		71.02	0.25		
	10	483		71.71	0.23		
	17	542		73.08	0.23		
	28	616		74.46	0.24		
22*	10	189	145	63.57	0.39	34	1.05
	17	224		64.95	0.38		
	24	258		61.91	0.38		
	31	280		63.02	0.38		
23*	10	161	108	74.46	0.36	24	1.18
	17	201		62.60	0.33		
	24	233		73.08	0.28		
	31	270		71.71	0.26		
24*	31	163	N/A	67.50	0.96	N/A	N/A

* Indicating defective samples

Recalling Figures 3-6 in the Sample Preparation chapter (Chapter 3), Samples 22, 23, 24 had pre-existing weak planes. For Sample 24, the volumetric strain started decreasing right after the test was started, thus the multistage strategy was not applied to the sample. For Sample 22 and Sample 23, their strength properties were impacted by pre-existing weak planes.

From the obtained strength properties in the Table. 4.7, the strength of samples with pre-existing fractures turned out to be much lower than the normal samples - Sample 22 and 23 show about 50% strength reduction, and Sample 24 has a compressive strength of only

163 MPa at 4500 psi confining pressure (compared with more than 500 MPa for the normal samples). Moreover, the Poisson's ratios of the defective samples are larger than the normal samples.

Table 0.8 Multistage triaxial test result – Roosevelt Gabbro (25-30)

Sample No.	Confining Pressure (MPa)	Compressive Strength (MPa)	Estimated UCS (MPa)	Static Young's Modulus (GPa)	Static Poisson's Ratio	Cohesion (MPa)	Coefficient of Friction
25	3	194	179	102.73	0.29	38	0.98
	7	220		106.91	0.30		
	10	243		106.77	0.31		
	17	279		107.64	0.31		
	24	313		106.41	0.31		
26	3	157	145	87.42	0.32	31	0.95
	7	185		100.45	0.30		
	10	207		100.70	0.31		
	17	242		100.01	0.31		
	28	272		96.48	0.32		
27	3	163	145	91.72	0.26	29	1.04
	7	187		99.87	0.31		
	10	212		103.63	0.31		
	17	254		99.03	0.31		
	24	291		101.66	0.31		
28	10	203	119	103.32	0.29	21	1.26
	17	263		103.15	0.29		
	24	312		103.83	0.28		
	24*	321		101.76	0.32		
29	10	197	128	100.05	0.19	25	1.09
	17	241		103.71	0.21		
	24	282		102.19	0.23		
	24*	294		105.47	0.28		
30	10	214	147	106.65	0.24	29	1.07
	17	259		109.64	0.33		
	24	303		115.02	0.34		
	24*	313		109.50	0.35		

* Indicating a different axial strain rate of loading

For Sample 28, 39, and 30, the confining pressure at the failure stage were selected to be the same as the previous non-failure stage, i.e., 24 MPa. However, the strain rate was increased in order to make the samples more brittle in failure to increase the chance of obtaining a clear single fracture. The axial strain rate at failure stage was $1.5 \times 10^{-5}\ strain/s$ for Sample 28 and $2.5 \times 10^{-5}\ strain/s$ for Sample 29 and 30, compared with regular rate of $5 \times 10^{-6}\ strain/s$.

4.5 Discussion

4.5.1 Dynamic-Static Relationship for the Tested Rocks

For most of the samples in the previous sections, both dynamic and static elastic constants were determined. In some situations, dynamically measured elastic properties are used rather than the static ones for the reasons such as lower cost, better test efficiency and non-destructive to the samples. Although it is not likely to obtain a universal relation between dynamic and static measured properties, it is still meaningful to discover the relation for our tested samples. For these purposes, the dynamically and statically measured Young's moduli are summarized in the Table 4.9 below. Note that, the dynamic Young's moduli are calculated using the average ultrasonic velocities at non-zero confining pressures; and the static Young's moduli are listed as the arithmetic mean of the average Young's modulus obtained in each testing stage.

Table 0.9 Dynamic and static modulus

Sample Number	**Density (g/cc)**	E_{static} **(GPa)**	E_{dyn} **(GPa)**	$k = \frac{E_{dyn}}{E_{static}}$
1	2.67	59.38	73.33	1.23
8	2.68	59.88	72.10	1.20
11	2.67	61.59	82.11	1.33
9	2.68	61.64	72.11	1.17
12	2.68	62.01	77.45	1.25
22	2.62	63.36	71.84	1.13
2	2.68	63.81	76.60	1.20
10	2.68	66.46	82.94	1.25
24	2.61	67.50	65.15	0.97
3	2.68	69.23	73.18	1.06
4	2.68	70.11	72.23	1.03
6	2.68	70.14	75.68	1.08
23	2.62	70.46	67.58	0.96
5	2.68	71.23	74.46	1.05
7	2.68	72.01	81.21	1.13
14	2.67	72.76	70.54	0.97
16	2.68	74.81	79.02	1.06
15	2.67	78.47	76.91	0.98
13	2.67	78.87	80.27	1.02
17	2.68	79.40	75.04	0.95
18	2.68	82.91	79.39	0.96
26	2.86	97.01	93.20	0.96
27	2.89	99.18	102.89	1.04
29	2.83	102.86	98.25	0.96
28	2.79	103.02	87.90	0.85
25	2.85	106.09	99.72	0.94
30	2.80	109.95	93.20	0.85

According to previous studies by various authors, the coefficient *k*, the ratio between dynamic and static modulus, tends to be bigger than one for low modulus values. And *k*

decreases when dynamic modulus increases until *k* becomes nearly equal to unity in samples with the large elastic moduli, typically 80 GPa (Brotons, 2016).

In order to present the trend of coefficient *k* of our measurements, the Table 4.9 has been sorted with an ascending $\boldsymbol{E_{static}}$ values. According to the table, a similar trend of *k* can be observed: *k* is larger (usually > 1.20) for Samples 1, 2, 8, 9, 10, 11, 12, which have relatively lower static Young's modulus among all the samples (59.38 GPa – 66.46 GPa). For other samples, the *k* value is closer to 1 as they have higher Young's modulus values (63.36 GPa - 82.91 GPa).

Much less data have been published for rocks with even higher Young's modulus, e.g., more than 100 GPa. Except for Christaras et al., 1994. They have published data for several types of rock with various Young's modulus as shown in Table 4.10. The test results of three basalt samples have the *k* value smaller than 1. Our results just matched this observation: most Roosevelt gabbro samples have *k* values less than 1. This can be explained by that the gabbro and basalt are related and gabbro is equivalent in composition to basalts but with different grain sizes.

Table 0.10 Dynamic and static modulus from Christaras et al., 1994

Rock Type	$\boldsymbol{E_{static}}$ **(GPa)**	$\boldsymbol{E_{dyn}}$ **(GPa)**	k
Limestone Re	19.88	24.7	1.24
Gypsum Rose	36.1	33.08	0.92
Andesite Vovic	28.72	26.58	0.93
Basalt Sauvat	101.83	101.66	1.00
Basalt Pradel 1	110.63	103.34	0.93
Basalt Pradel 2	114.37	110.21	0.96
Granite Gueret	63.98	65.11	1.02
Phonolite	56.5	63.39	1.12

For the discrepancy between the static and dynamic moduli, Schön (2011) has suggested that the reasons could be the different mechanisms of dynamic and static measurements: During the static deformation, nonelastic components (due to mobilization of microcracks and grain boundaries) will occur; the ultrasonic measurements are mainly affected by the elastic response. Both static and dynamic moduli decrease with increasing crack porosity, but the static modulus will show a stronger decrease than the dynamic modulus. Therefore, for the rock with less crack porosity, its density tends to be high. Meanwhile, the k coefficient of it will become closer to the unity than the rocks with more crack porosity.

4.5.2 Overall Failure Envelope

From the multistage triaxial testing results, the shear strength can be represented in terms of normal stresses for each tested sample. If we plot all the shear strength points, a lower bound and upper bound envelops can be established. Fig. 4-8 and 4-9 are the constructed overall failure envelopes for the Arbuckle Group samples and the basement rocks, respectively. In each plot, all of the points are bonded by two straight lines. The two lines are constructed using the maximum and minimum coefficient of internal friction and cohesion for each rock type, respectively. No failure tends to occur below the lower bonded line. And from the average values of coefficient of internal friction and cohesion, the overall trend of failure is described as the middle dashed line. In Fig. 4-9, the strength reduction caused by pre-existing weak planes can be clearly observed. It can be seen that the distribution of the red square marks (representing Troy granite samples) are separated into two parts. Results of normal Troy granite samples are distributed close to the upper bond envelope. The others, which are close to the lower bond envelope, indicating high risk of failure, are exactly the results of the defective (with pre-existing cracks) Tory granite samples (Sample 22 and 23). However, in reality, the failure is more complex and depends on the temperature, pore pressure, and pre-existed fracture conditions. Our plot only represented results in laboratory conditions and scale.

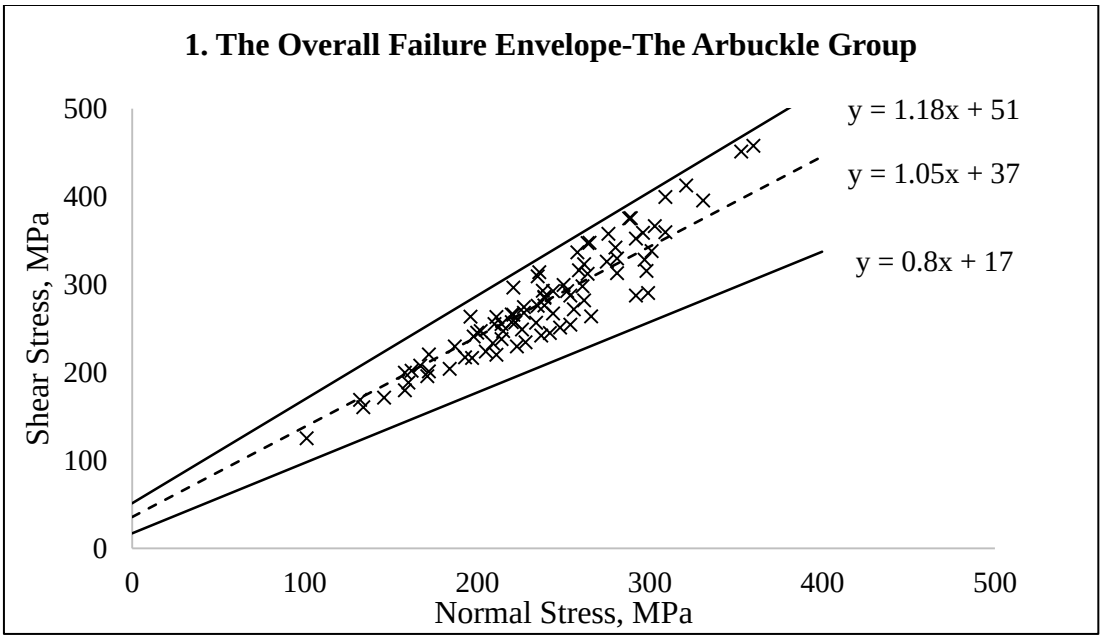

Fig. 0-8 The overall failure envelope - The Arbuckle Group

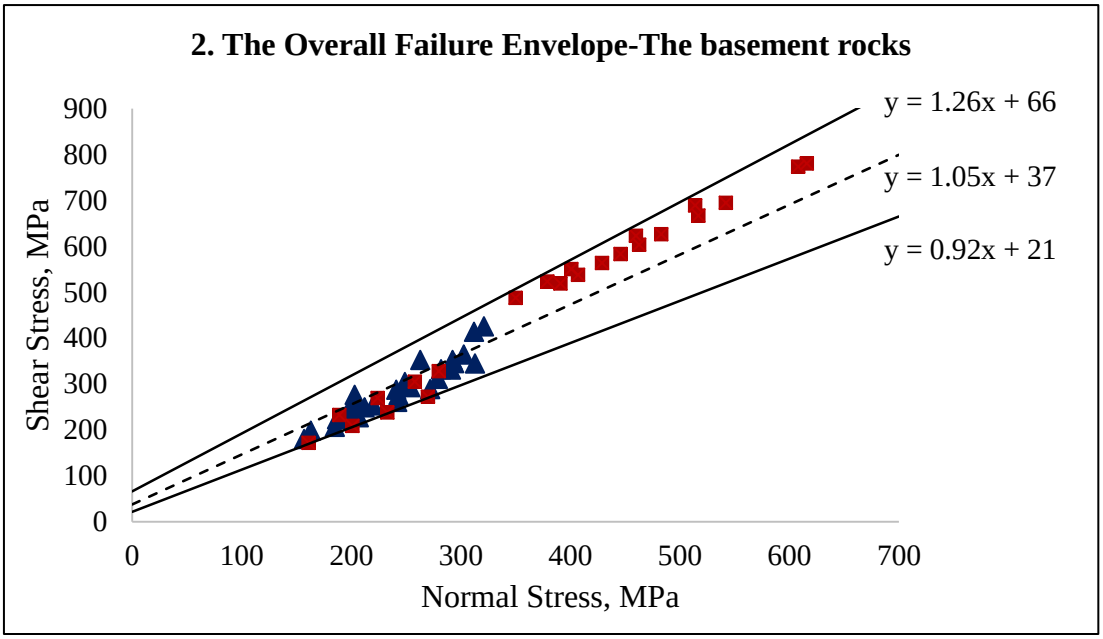

Fig. 0-9 The overall failure envelope - The basement rocks

*the black crosses represent the Arbuckle samples, the **blue triangles** represent the Roosevelt gabbro samples, and the **red squares** represent the Troy granite

Chapter 5 Rock Joint Characterization

Four specimens from previous multistage triaxial tests are selected for experimental characterization of rock joint properties: Sample 7, 8, 23, and 30. Among them, sample 7 and 8 are the Arbuckle Group samples; Sample 23 is the Troy granite and Sample 30 is the Roosevelt gabbro. As shown in the Fig. 5-1, all specimens have induced good single fracture caused by compressional forces in their failure stages. As we mentioned in the previous chapter, the sample 23 has pre-existed weak plane. For the induced joint plane on sample 23, it basically followed the pre-existed weak plane. For other three specimens, Sample 7, 8 and 30, no obvious pre-existed weak plane or discontinuity was observed before the triaxial testing. So the fracture on those samples are formed during the triaxial compression testing.

Fig. 5-2 presents the joint profiles along the major axis of the fracture surfaces measured by an *Empire 6 in. Contour Gauge*. Note that, the contours are obtained after the triaxial shear test of each specimen because the measurements could possibly damage the fracture surfaces.

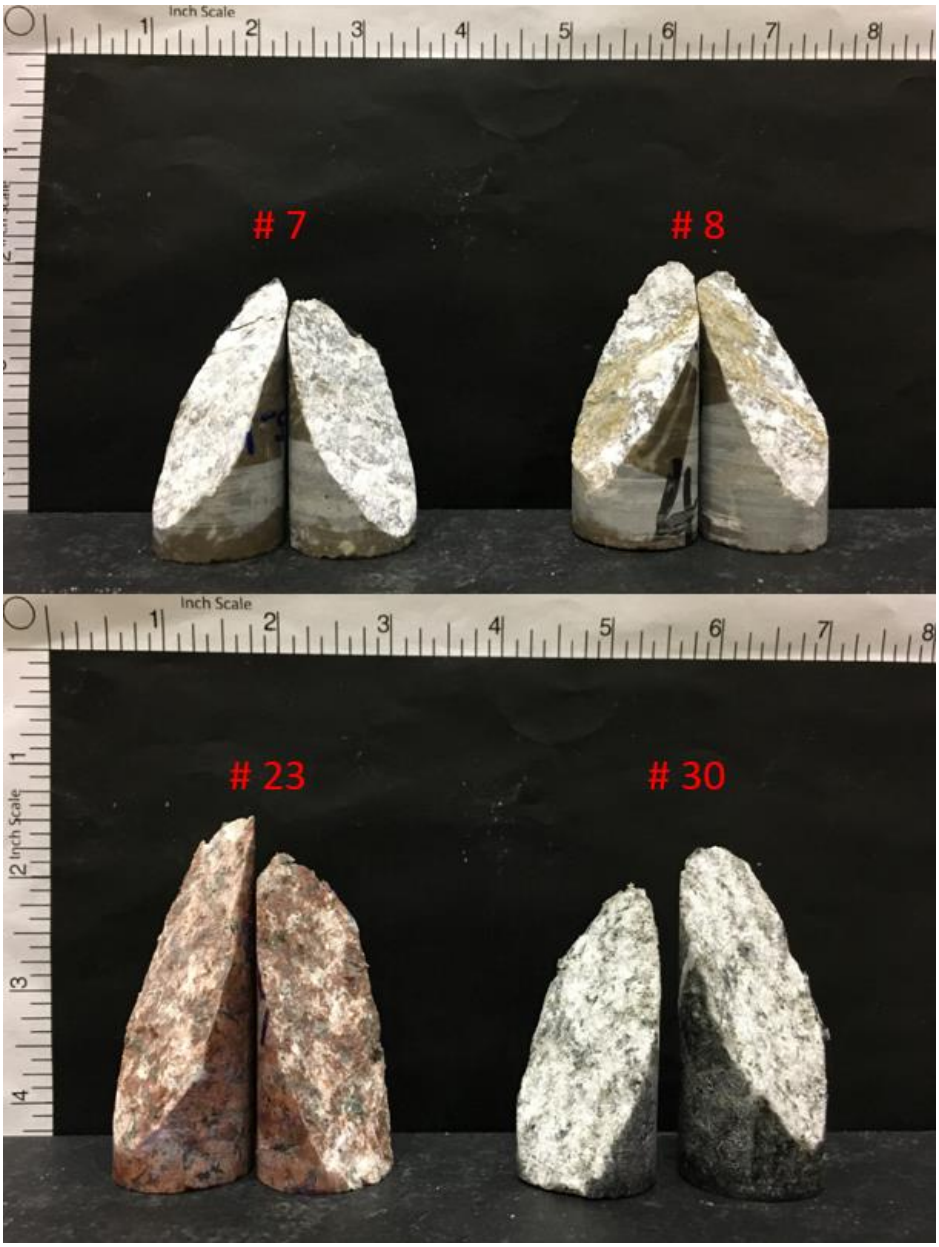

Fig. 0-1 Jointed Rock Samples

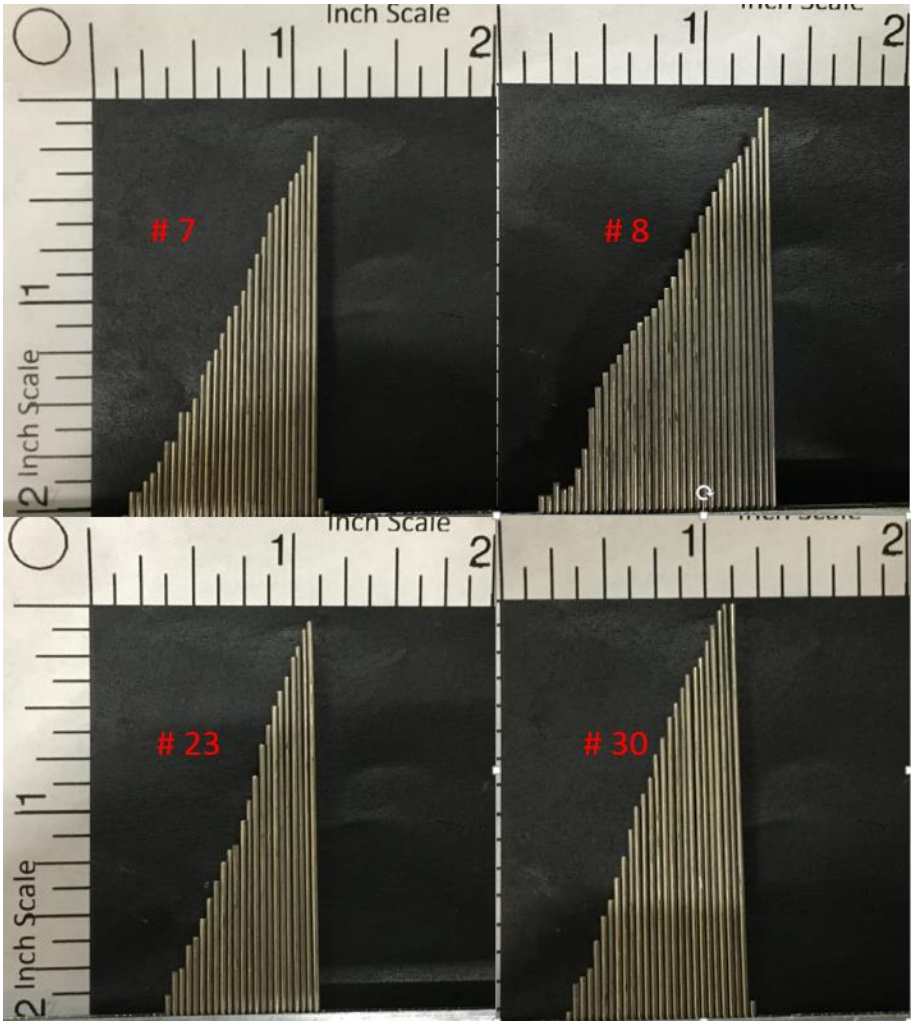

Fig. 0-2 Joint Profiles along major axis

5.1 Experimental Setup

The rock joint property characterization requires experimental setup similar to the multistage triaxial test. The test system (Fig. 5-3) set up consist of:

- An MTS Model 816 test system with a force capacity of 1048 kN force with an MTS 20.000 psi pressure vessel
- A computer with MTS series 793™ controller software for test control and data acquisition

Additionally, as shown in Fig. 5-3 and 5-4, the sample setup consists of:

- A pair of stainless steel platens;
- Two Linear Variable Differential Transformer (LVDT) extensometers for axial displacement measurement
- A TerraTek ring with four strain-gaged cantilevel beams measuring two transverse displacements

To setup the sample, a pair of stainless platens are placed on top and bottom of the jointed sample. The polyeofin tubing jacket is completely heat shrunk over it to provide isolation of confining fluid. The ends of the jacked shall be clamped on the silicone tape strips with stainless steel wires. Two LVDTs measuring axial displacements are fixed in a pair of 3D-printed PLA material rings (same as for triaxial test) which are mounted in perpendicular to longitudinal axis of the sample. Then, the TerraTek ring with four strain-gaged steel cantilevel beams are fixed over the sample. The free ends of two pairs of transverse cantilevel beams have screws mounted on them to contact the side of the specimen. Fig. 5-4 presents a jointed sample after the setup. To measure the fracture sliding, one pair of the beam should cross the joint surface, another pair should on the same side of the joint surface with about 2 mm above/below the joint. When the sample is ready to be tested, it will be placed into the MTS triaxial vessel on the internal load cell and then starting the testing procedures.

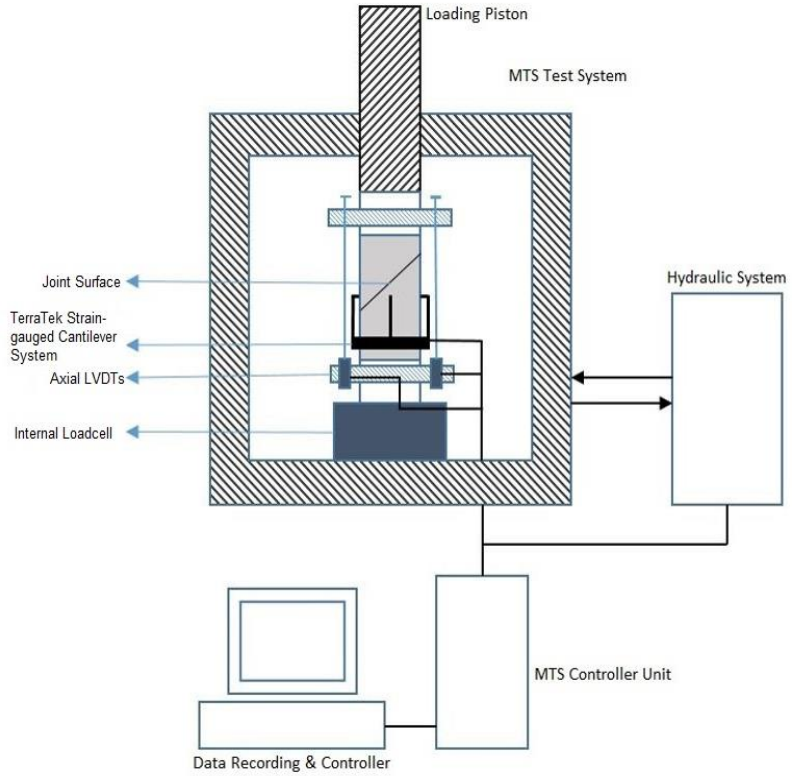

Fig. 0-3 Schematic diagram of test setup

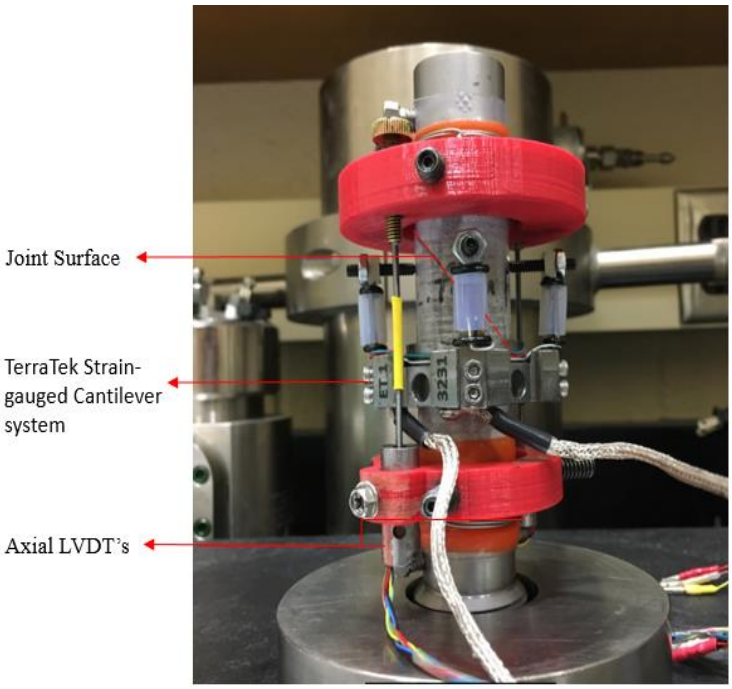

Fig. 0-4 Triaxial Shear Test Sample Setup

5.2 Procedures

After the sample was properly put inside the cell, the connections for axial LVDTs, cantilevel beams, and load cell shall be completed and adjusted to within the desired range. Once the signals of each connection has been checked, the MTS series 793™ controller software will be used to control the test step by step with the following process. The multistage strategy has also been used to obtain shear strength envelope from a single jointed sample.

1) The pressure vessel is closed and the bolts on the cell are tightened to ensure good sealing. Then the vessel is filled with hydraulic oil
2) Confining pressure is increased to the first-stage hydrostatic testing pressure
3) The axial load is increased at a constant axial strain rate to the point at which the rock joint is about to slide (Diagnosed by: In the real-time transvers displacement vs. axial stress plot, one of the transverse displacement start to go straight upward, at same time, another transverse displacement does not change much)
4) Lower the axial stress until a hydrostatic state is reached again. Then, increase the confining pressure to the next-stage hydrostatic testing pressure. Repeat step 3 and 4 for several times (at least 3 times)
5) Reduce axial stress to the initial hydrostatic condition, then reduce the confining pressure to zero and disassemble sample.

Unless noted otherwise, the axial strain rate is $5 \times 10^{-6}\ strain/s$ and is kept same in every stage of each test.

5.3 Triaxial Shear Testing

5.3.1 Barton's Shear Strength Envelope

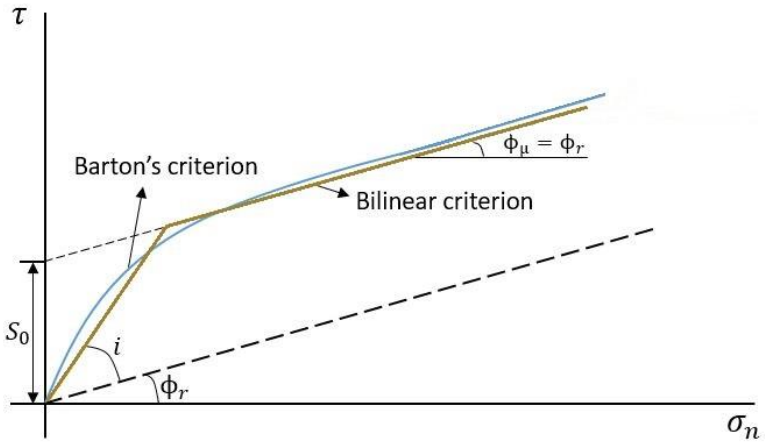

Fig. 0-5 Shear Strength criteria of rock joints

Similar to the multistage triaxial compression test, in multistage shear testing, the jointed rock specimen is subjected to an increasing axial load at different confining pressures until the rock joint just start to slip. At each confining pressure, the shear (τ) and normal stress (σ_n) of joint surface can be calculated by equation (2.9) and (2.10) from the axial stress (σ_1), confining pressure (σ_3), and the angle of the joint plane (θ). The obtained normal and shear stresses at different confining pressures are presented in the Table 5.1 below.

Barton (1973, 1976) studied the behavior of natural rock joints and proposed a shear strength criterion that can described as:

$$\tau = \sigma_n \tan\left(JRC\ log_{10}(\frac{JCS}{\sigma_n}) + \phi\right) \tag{5.1}$$

where, JRC is the joint roughness coefficient and JCS is the joint wall compressive strength, ϕ is the basic friction angle (ϕ_b), or residual friction angle (ϕ_r) of the joint. A least-square curve fitting method (Li, Wang et al. 2012) is used to determine those three

parameters of a shear strength envelope. The curve fitting results are shown in the Fig. 5-5 to 5-8. And the shear and normal stresses, JRC, JCS and ϕ for four tested specimens are summarized in the following Table 5.1.

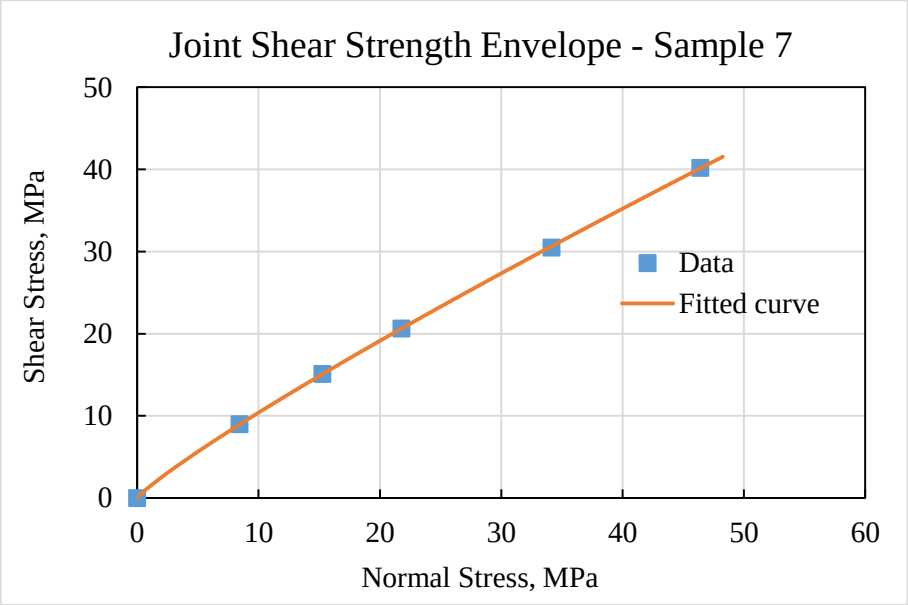

Fig. 0-6 Shear Strength Envelope-sample 7

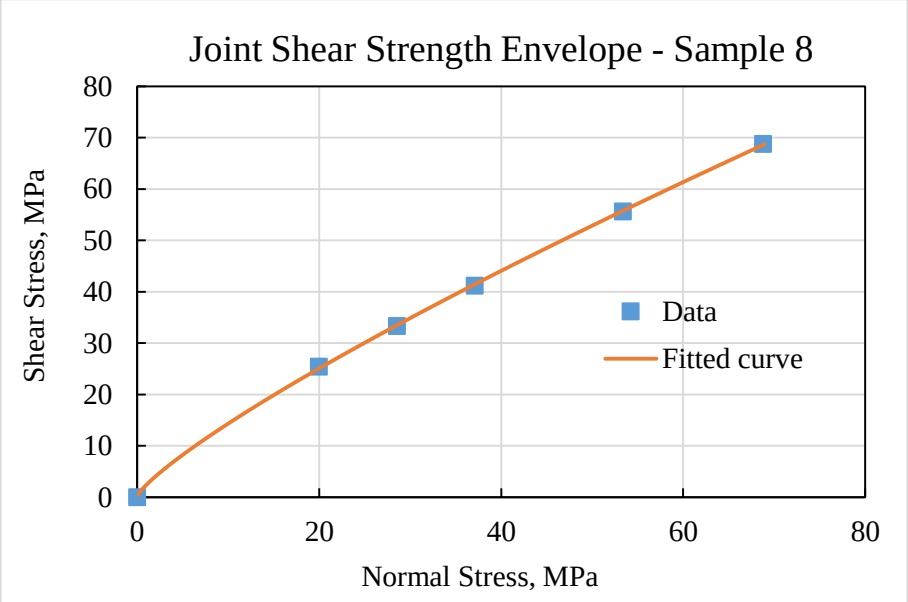

Fig. 0-7 Shear Strength Envelope-sample 8

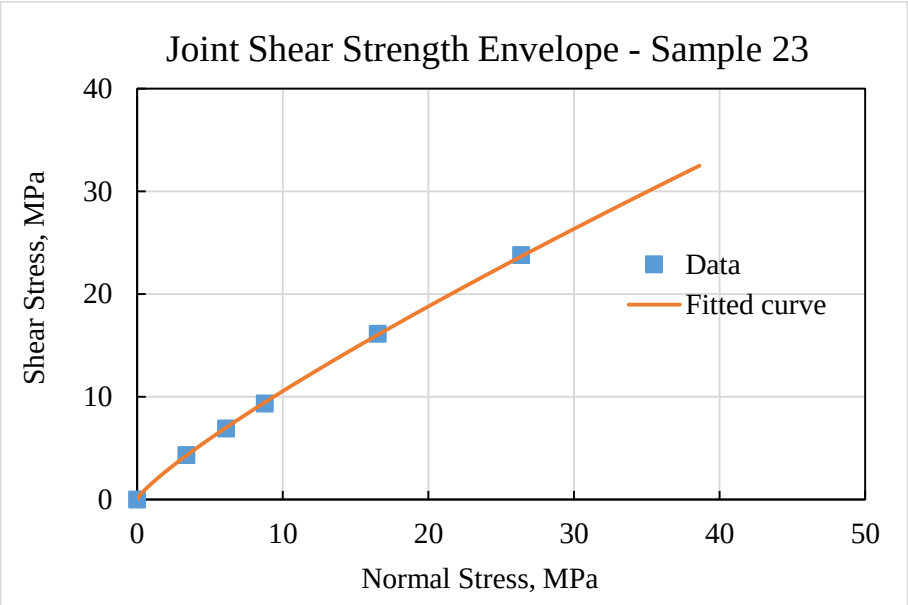

Fig. 0-8 Shear Strength Envelope-sample 23

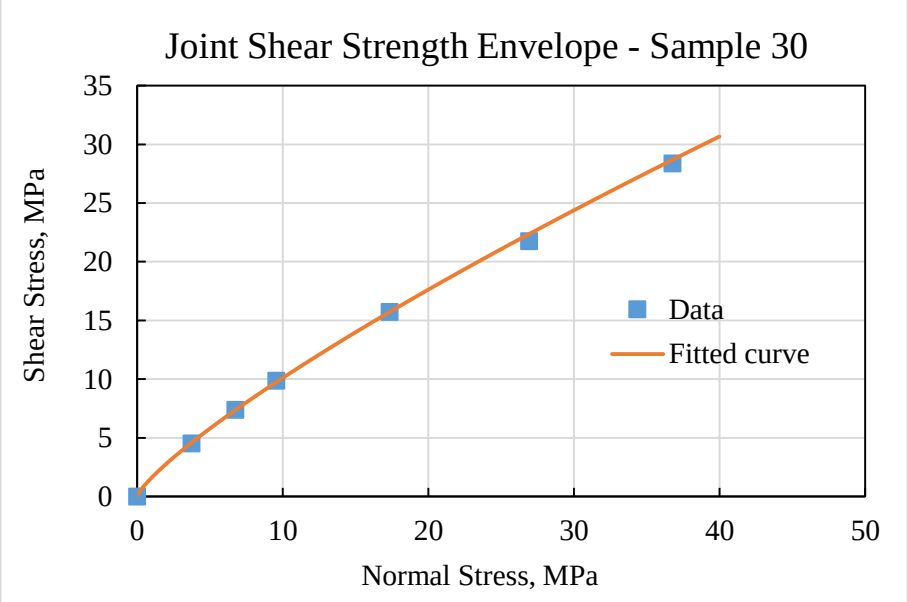

Fig. 0-9 Shear Strength Envelope-Sample 30

Table 0.1 Triaxial Shear test results

Sample # (Joint angle)	Conf. Pressure (psi)	Compressive Strength (psi)	Normal Stress (psi)	Shear Stress (psi)	JRC	JCS (psi)	ϕ_r
# 7 (29°)	3	24.67	8.44	9.00	0.14	179	36.2°
	7	42.51	15.27	15.10			
	10	59.03	21.78	20.64			
	17	89.18	34.15	30.51			
	24	118.99	46.43	40.22			
# 8 (33°)	3	59.08	19.95	25.41	0.21	106	42.6°
	7	79.86	28.54	33.33			
	10	100.51	37.09	41.19			
	17	139.06	53.37	55.65			
	24	174.61	68.77	68.74			
# 23 (21°)	2	14.65	3.38	4.32	0.19	120	34.7°
	3	24.07	6.10	6.90			
	5	33.10	8.76	9.34			
	10	58.53	16.53	16.12			
	17	88.38	26.37	23.80			
	24	115.05	35.81	30.42			
# 30 (24°)	2	13.90	3.74	4.52	0.23	134	30.7°
	3	23.36	6.74	7.40			
	5	31.70	9.56	9.86			
	10	52.67	17.34	15.73			
	17	75.79	26.92	21.76			
	24	100.52	36.77	28.39			

From the previous chapters of intact sample geomechanical properties characterization, the UCS obtained for Sample 7, 8, 23 and 30 are 179, 106, 120 and 134 MPa, respectively. The JCS we obtained from triaxial shear testing vary by -7.4% to 23.5% compared to the UCS values characterized in triaxial compression testing. This indicates the weathering of intact rock material and joint walls was small. All the JRC values obtained in back-analysis for our tests are small. It is similar to (Li, Wang et al. 2012). The possibly reason can be the scale of the specimens are relatively small, so that the large waviness of fracture is more difficult to be captured within the fracture surfaces.

5.3.1 Fracture Stiffness

The joint normal and shear stiffnesses are determined from the stresses and displacements in normal and shear directions of the joint surface. In general, at different confining pressures, different normal stress-displacement behavior shall be expected from triaxial shear testing with constant axial strain rate control (Brechtel 1978). They can be summarized as four plots as shown in the Fig. 5-10 below. Note that in each plot, the curve of normal stress-displacement always starts at the stress equal to the confining pressure. This is because the loading and recording of our test was not started until the hydrostatic state was reached. At this initial stress state, the normal stress on the joint surface equals to the confining pressure, and the shear stress is zero. And since the rock joint already partially closed due to the applied confining pressure, this part of joint closing was not reflected through our measured normal stiffnesses.

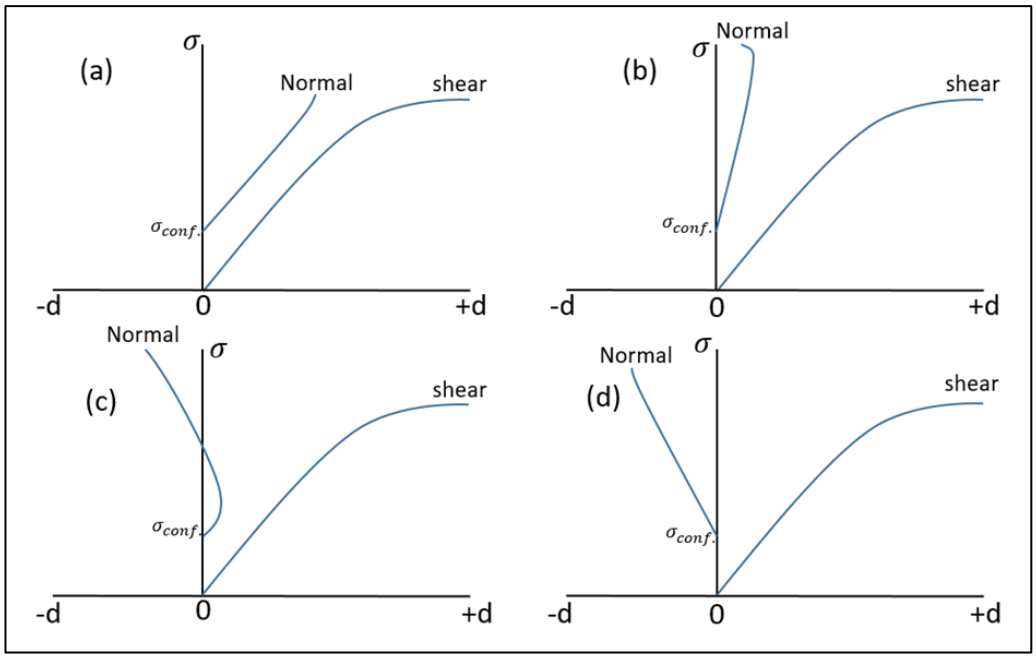

Fig. 0-10 Different stress-displacement plots of triaxial shear testing

From the Fig. 5-10 above, (a) presents the joint deformation behavior of a smooth joint surface (e.g. saw-cut); (b) presents the joint deformation behavior at high confining pressure when the asperities are sheared off. Both cases indicate the behavior of joint closing with an increased axial stress applied on the joint surface. But the normal stiffness of case (b) is usually higher than the case (a). Plots (c) and (d) present joint deformation behaviors at low confining pressure, or when the asperities are strong. For case (c), the joint undergo a small amount of closure and then begin to open. In the case (d) the joint could open immediately when the axial loading start to increase. Joint opening in these cases are caused by riding over the asperities. And the normal stiffness value cannot be obtained for these cases.

For the shear deformation of the joint, the deformation is always in the same direction as the shear stress. Usually, the shear stress increases linearly as the shear displacement increases until a peak stress has been reached. Usually, this transaction is close but before the joint slip which we used as unloading criterion of the test.

Fig. 5-9 to 5-12 show the stress-displacement curves for four jointed specimen at different confining pressures, respectively. The values of joint stiffness are summarized in the Table 5.2. The shear stiffness are obtained from the slope of the linear part of the shear stress-displacement curve; and the normal stiffness are obtained from the average slope of the normal stress-displacement curve if it represents the closure of the joint.

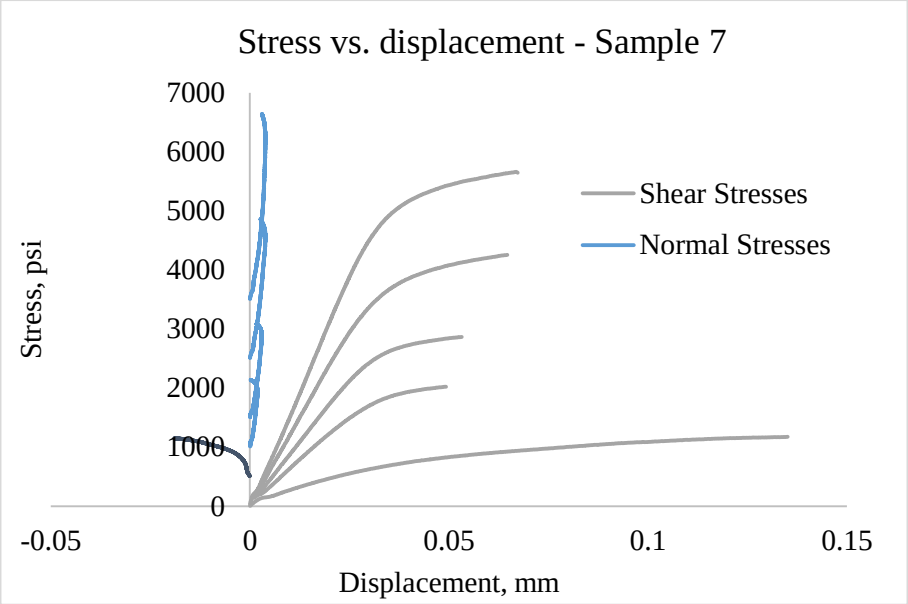

Fig. 0-11 Stress-displacement curve of rock joint-sample 7

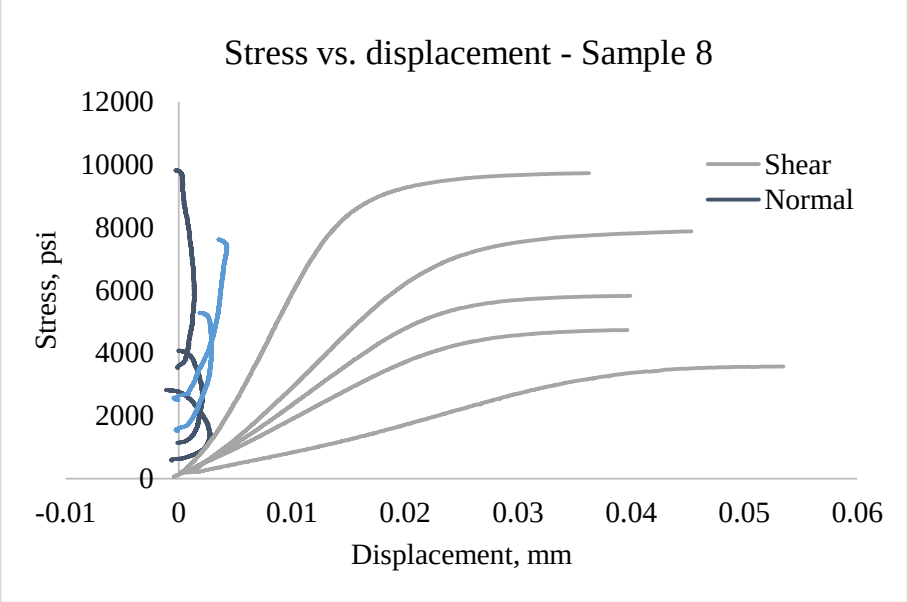

Fig. 0-12 Stress-displacement curve of rock joint-sample 8

*Normal stiffness values are obtained from lighter colored normal stress-displacement curves

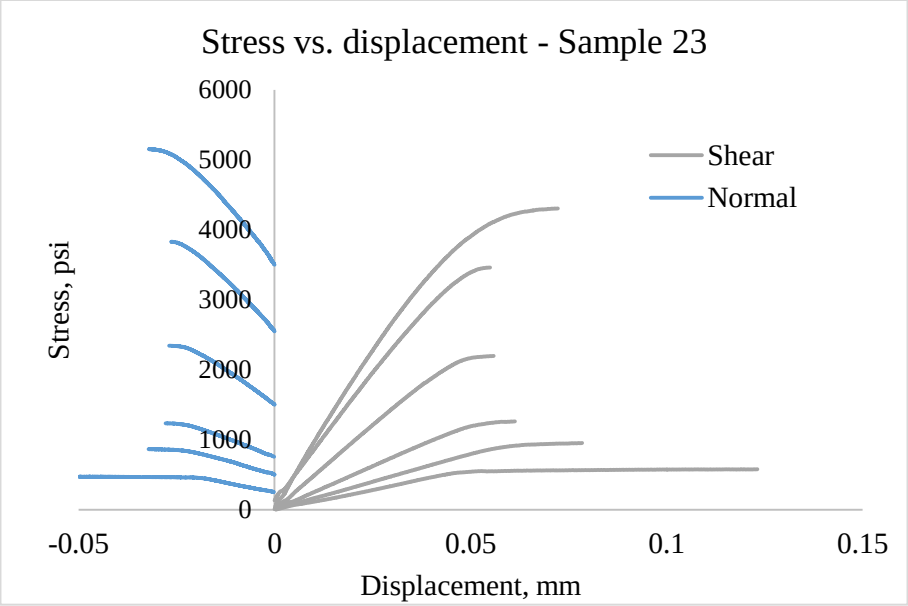

Fig. 0-13 Stress-displacement curve of rock joint-sample 23

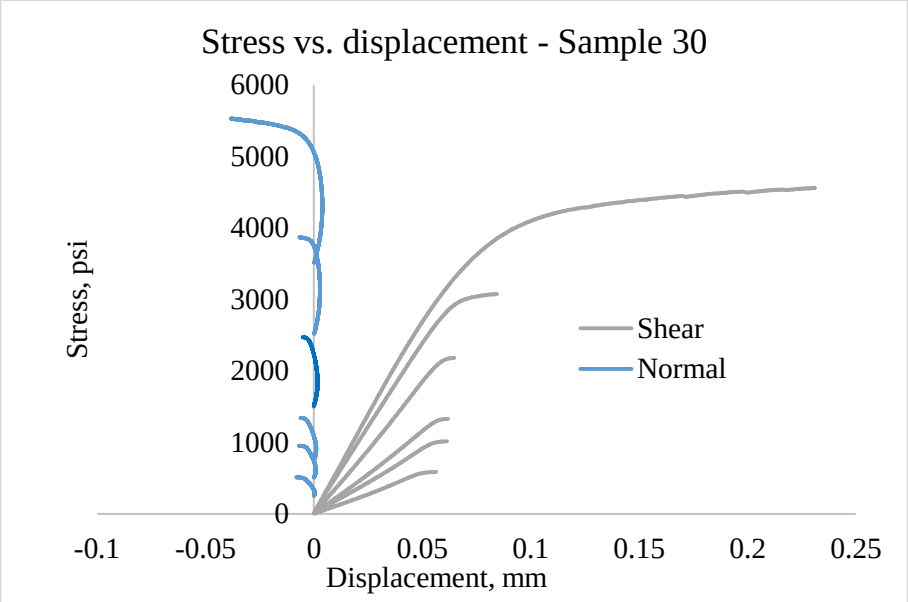

Fig. 0-14 Stress-displacement curve of rock joint-sample 30

*No normal stiffness values are obtained from Fig. 5-13 and 5-14.

Table 0.2 Joint stiffness at different confining pressures

Sample # (Joint angle)	Conf. Pressure (MPa)	Normal stiffness (MPa/mm)	Shear Stiffness (MPa/mm)
# 7 (29°)	3	\	110.53
	7	3856.95	405.89
	10	3620.48	583.42
	17	3981.52	809.99
	24	4785.22	1103.84
# 8 (33°)	3	\	629.68
	7	\	1286.39
	10	7824.26	1762.32
	17	7607.30	2339.94
	24	\	4628.11
# 23 (21°)	2	\	80.28
	3	\	110.02
	5	\	169.80
	10	\	326.53
	17	\	487.23
	24	\	570.84
# 30 (24°)	2	\	79.39
	3	\	125.41
	5	\	162.17
	10	\	257.87
	17	\	322.40
	24	\	357.20

As shown in the Table 5.2 and the relevant figures above, the samples from the Arbuckle Group show higher shear stiffness than the sample from the crystalline basement, especially Sample 8 which has the largest shear stiffness (by one order). Although the rock types are different, Sample 23 and 30 have close shear stiffness values. In general, the shear stiffness is sensitive to the confining pressure and increases as the confining pressure increases.

The rock samples from basement tend to have stronger asperities. The Arbuckle samples, however, have a finite normal stiffness at relatively higher confining pressures, which may indicate joint sliding tends to shear-off the asperities rather than ride over them. The

measured normal stiffness of Arbuckle samples are not sensitive to the different confining pressures.

Chapter 6 Conclusions and Recommendations

In the laboratory characterization program, three types of rock, Arbuckle limestone, Troy granite and Roosevelt gabbro, from the lower Arbuckle Group and the crystalline basement of Oklahoma were characterized for different geomechanical properties, on both intact and jointed rock specimens.

Before testing, the density and hardness index measured by a *Procerq Portable Material Hardness Tester* are recorded for each specimen, by which the rock types can be distinguished. The Arbuckle limestone have densities of 2.67-2.68 g/cc and 618-677 hardness index; the Troy granite have densities of 2.61-2.62 g/cc and 798 to 869 harness index; and the Roosevelt gabbro have densities od 2.79 to 2.89 g/cc and 725 to 776 hardness index. The gabbro represent higher level of heterogeneity from the density measurements.

For intact rock samples, both dynamic and static properties were characterized. Through the ultrasonic measurement, we found the compressive wave velocities varied for different types of rock. The Roosevelt gabbro have a much higher P-wave velocities, about 7000 m/s, followed by the Arbuckle limestone, about 6000 m/s, then the Troy granite, about 5300 m/s. It follows the same orders as the decent densities among three rock types. The S-wave, however, do not various as much, especially for Arbuckle and Troy granite which have very similar S-wave velocities, about 3300 m/s. The average S-wave velocities of Roosevelt gabbro are just about 300 m/s bigger, equal to 3583 m/s. In general, very small or no pressure dependence was observed for the ultrasonic velocities measurement. However, for all the measurements when the confining is zero or small, the results are tend to be much smaller.

Furthermore, we have calculated dynamic parameters using the measured wave velocities. For the Arbuckle limestone, Thomsen parameters were obtained taken advantages of availability of specimens in three different directions: $\varepsilon \approx 0$, $\gamma \approx 0.025$, and $\delta \approx 0.07$, which indicate the small anisotropy of the rock. Meanwhile, the dynamic elastic modulus are obtained. Those elastic constants were compared with the ones obtained in multistage triaxial tests. Using *k* (the ratio between dynamic and static modulus) to represent, our results match the trends from massive previous researches: *k* is always bigger than 1 for samples with lower Young's modulus (less than 60 GPa), and it is close to 1 for samples with higher Young's modulus (about 80 GPa). For the Roosevelt gabbro whose Young's modulus is extremely high (more than 100 GPa), the *k* can be smaller than 1.

The multistage triaxial test on intact rock samples gave important strength properties of the rock. The strongest rock is the Troy granite. For all three intact samples, the UCS of them are all over 300 MPa. However, the for the granite samples with pre-existed weak planes, the strength decreased more than 50% compared with the intact ones. Both Arbuckle and Troy granite samples have relative brittle deformation behaviors, the sudden breakages were observed at the failure stages. On the other hand, the gabbro samples are more ductile. The failures of those samples usually occurred gradually and with a residual strength at last. The observation in rock strength imply that although in crystalline basement where the rock strength could be very high, the existing of pre-existed fractures may increase the risk of earthquakes because it dramatically affected the rock strength. Moreover, the Troy granite is with more risks rather than the Roosevelt gabbro because the brittle/ductile behavior of the failures. For the Troy granite, the high

strength allows it to preserve more energy. But when the failure occurs, the brittle failure also let the energy being released drastically.

At last, the triaxial shear testing characterized rock joint properties of selected samples with joints induced by compression in the previous tests. Empirical parameters such as JRC and JCS are obtained from back-analysis using Barton's shear strength criterion which can be used in numerical modeling and analysis of MEQ in the Oklahoma. In addition, the joint shear stiffness are obtained from the stress-displacement curves from triaxial shear testing. The two tested jointed rock samples from basement have similar shear stiffness values, about 120 MPa/mm at 3 MPa confining pressure and increased to 350 MPa/mm or 570 MPa/mm as confining pressures reached 24 MPa. The two Arbuckle samples have much different shear stiffness: one from 110 MPa/mm at 3 MPa to 1103 MPa/mm at 24 MPa; and another from 630 MPa/mm at 3 MPa to 4628 MPa/mm at 24 MPa. According to the results on the four jointed specimens, the shear stiffness of Arbuckle limestone is larger and more sensitive to confining pressure than it of the Troy granite and Roosevelt gabbro. At the same shear stress condition, the joint in basement rock tend to slip easier.

References

ASTM (2014). Standard Test Methods for Compressive Strength and Elastic Moduli of Intact Rock Core Specimens under Varying States of Stress and Temperatures, ASTM International.

Al-Shayea, N. A. (2004). "Effects of testing methods and conditions on the elastic properties of limestone rock." Engineering geology **74**(1): 139-156.

Assefa, S., et al. (2003). "Velocities of compressional and shear waves in limestones." Geophysical prospecting **51**(1): 1-13.

ASTM (2008). D2845-08 (2008) Standard test method for laboratory determination of pulse velocities and ultrasonic elastic constants of rock. ASTM International, West Conshohocken.

ASTM, D. (1994). "3080-90: Standard test method for direct shear test of soils under consolidated drained conditions." Annual Book of ASTM Standards **4**: 290-295.

Barton, N. (1976). The shear strength of rock and rock joints. International Journal of rock mechanics and mining sciences & Geomechanics abstracts, Elsevier.

Barton, N. and V. Choubey (1977). "The shear strength of rock joints in theory and practice." Rock Mechanics and Rock Engineering **10**(1): 1-54.

Bickford, M. and R. D. Lewis (1979). "U-Pb geochronology of exposed basement rocks in Oklahoma." Geological Society of America Bulletin **90**(6): 540-544.

Bieniawski, Z. T. (1967). Mechanism of brittle fracture of rock: part I—theory of the fracture process. International Journal of Rock Mechanics and Mining Sciences & Geomechanics Abstracts, Elsevier.

Brace, W., et al. (1966). "Dilatancy in the fracture of crystalline rocks." Journal of Geophysical Research **71**(16): 3939-3953.

Brechtel, C. E. (1978). The strength and deformation of singly and multiply jointed sandstone specimens, Brechtel.

Brotóns, V., et al. (2013). "Study of creep behavior of a calcarenite: San Julián´ s stone (Alicante)." Materiales de Construcción **63**(312): 581-595.

Crawford, A. M. and D. A. Wylie (1987). A modified multiple failure state triaxial testing method. The 28th US Symposium on Rock Mechanics (USRMS), American Rock Mechanics Association.

Eissa, E. and A. Kazi (1988). Relation between static and dynamic Young's moduli of rocks. International Journal of Rock Mechanics and Mining Sciences & Geomechanics Abstracts, Elsevier.

Ellsworth, W. L. (2013). "Injection-induced earthquakes." Science **341**(6142): 1225942.

Gardner, G., et al. (1964). "Effects of pressure and fluid saturation on the attenuation of elastic waves in sands." Journal of Petroleum Technology **16**(02): 189-198.

Ghassemi, A., et al. (2007). "A 3-D study of the effects of thermomechanical loads on fracture slip in enhanced geothermal reservoirs." International Journal of Rock Mechanics and Mining Sciences **44**(8): 1132-1148.

Haimson, B. and C. Chang (2000). "A new true triaxial cell for testing mechanical properties of rock, and its use to determine rock strength and deformability of Westerly granite." International Journal of Rock Mechanics and Mining Sciences **37**(1): 285-296.

Handin, J. and R. V. Hager Jr (1957). "Experimental deformation of sedimentary rocks under confining pressure: Tests at room temperature on dry samples." AAPG Bulletin **41**(1): 1-50.

Healy, J., et al. (1968). "The denver earthquakes."

Hughes, D. S. and J. H. Cross (1951). "Elastic wave velocities in rocks at high pressures and temperatures." Geophysics **16**(4): 577-593.

Jaeger, J. (1971). "Friction of rocks and stability of rock slopes." Geotechnique **21**(2): 97-134.

Keranen, K. M., et al. (2013). "Potentially induced earthquakes in Oklahoma, USA: Links between wastewater injection and the 2011 Mw 5.7 earthquake sequence." Geology **41**(6): 699-702.

Kim, M. M. and H.-Y. Ko (1979). "Multistage triaxial testing of rocks."

King, M. and I. Fatt (1962). "Ultrasonic shear-wave velocities in rocks subjected to simulated overburden pressure." Geophysics **27**(5): 590-598.

Kovari, K. and A. Tisa (1975). "Multiple failure state and strain controlled triaxial tests." Rock mechanics **7**(1): 17-33.

Li, Y., et al. (2012). Mechanical properties of intact rock and fractures in welded tuff from Newberry Volcano. Proceedings of 37th Workshop on Geothermal Reservoir Engineering, Stanford, CA.

Maurer, W. C. (1965). "Shear failure of rock under compression." Society of Petroleum Engineers Journal **5**(02): 167-176.

Mavko, G., et al. (2009). The rock physics handbook: Tools for seismic analysis of porous media, Cambridge university press.

McNamara, D., et al. (2015). "Efforts to monitor and characterize the recent increasing seismicity in central Oklahoma." The Leading Edge **34**(6): 628-639.

Morgan, B. C. and K. E. Murray (2015). "Characterizing small-scale permeability of the Arbuckle Group, Oklahoma."

Murray, K. E. (2014). "Class II underground injection control well data for 2010–2013 by geologic zones of completion, Oklahoma."

Paterson, M. (1958). "Experimental deformation and faulting in Wombeyan marble." Geological Society of America Bulletin **69**(4): 465-476.

Patton, F. D. (1966). Multiple modes of shear failure in rock. 1st ISRM Congress, International Society for Rock Mechanics.

Peselnick, L. and I. Zietz (1959). "Internal friction of fine-grained limestones at ultrasonic frequencies." Geophysics **24**(2): 285-296.

Rosso, R. (1976). A comparison of joint stiffness measurements in direct shear, triaxial compression, and in situ. International Journal of Rock Mechanics and Mining Sciences & Geomechanics Abstracts, Elsevier.

Safari, R. and A. Ghassemi (2015). "3D thermo-poroelastic analysis of fracture network deformation and induced micro-seismicity in enhanced geothermal systems." Geothermics **58**: 1-14.

Safari, R. and A. Ghassemi (2016). "Three-dimensional poroelastic modeling of injection induced permeability enhancement and microseismicity." International Journal of Rock Mechanics and Mining Sciences **84**: 47-58.

Swanson, S. R. and W. S. Brown (1972). "The influence of state of stress on the stress-strain behavior of rocks." Journal of Basic Engineering **94**(1): 238-242.

Vachaparampil, A., & Ghassemi, A. (2017, June). Strength Criteria for Shale under True Triaxial Stresses. In *51st US Rock Mechanics/Geomechanics Symposium*. American Rock Mechanics Association.

Thomsen, L. (1986). "Weak elastic anisotropy." Geophysics **51**(10): 1954-1966.

Walsh, F. R. and M. D. Zoback (2015). "Oklahoma's recent earthquakes and saltwater disposal." Science advances **1**(5): e1500195.

Wang, J., et al. (2016). "Geomechanical characterization of Newberry Tuff." Geothermics **63**: 74-96.

Watson, E. B. and T. M. Harrison (1983). "Zircon saturation revisited: temperature and composition effects in a variety of crustal magma types." Earth and Planetary Science Letters **64**(2): 295-304.

Wawersik, W. (1974). Time-dependent behaviour of rock in compression. Advances in rock mechanics: proceedings of the third Congress of the International society for rock mechanics, Denver, Colorado.

Weatherby, B. B. and L. Y. Faust (1935). "Influence of geological factors on longitudinal seismic velocities." AAPG Bulletin **19**(1): 1-8.

Ye, Z., et al. (2016). Fracture Properties Characterization of Shale Rocks. Unconventional Resources Technology Conference, San Antonio, Texas, 1-3 August 2016, Society of Exploration Geophysicists, American Association of Petroleum Geologists, Society of Petroleum Engineers.

Appendix. A. Stress-Strain Curves in Multistage Triaxial Testing

In Appendix. A, stress-strain curves of 30 multistage triaxial compression tests are represented. From the figures, we can conclude the Young's modulus for the most tested samples are not obviously affected by the different confining pressures and repeat loading processes as the stress-strain curves from of different stages are mostly overlapped each other. Moreover, the figure of stress-strain curves can represent the brittle/ductile failure behavior of tested tock samples. For example, the very staring line of Fig. A. 2 of post-failure part represent brittle failure mode that happened in a very short of time. The rocks with such failure mode tend to have none or very small residual strength. As a comparison, for all the Roosevelt gabbro samples, the stress tend to become stable after ultimate strength point and with a residual value. From the figures, the samples yield brittle failures are 2, 3, 4, 5, 6, 8, 9, 15, 16, and 18 of Arbuckle Group; 19 – 23 of Troy granite; and none of Roosevelt gabbro. It indicates that the Troy granite is also the most brittle rock (5 out of 6 behaved brittle failure); followed by the Arbuckle limestone (about half tested samples behaved brittle failure); and the Roosevelt granite is the most ductile one among them.

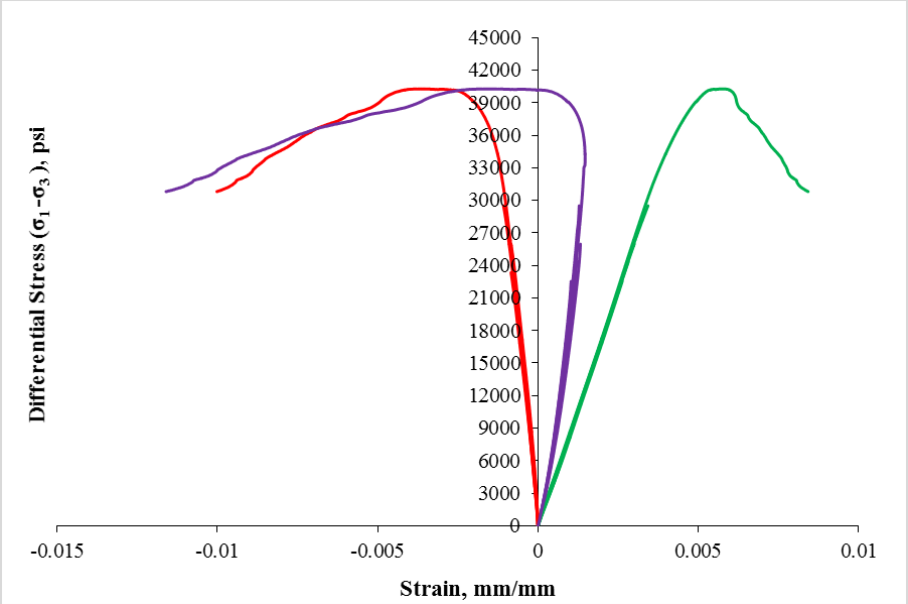

Fig. A.1 Stress-Strain Curves – Sample # 1

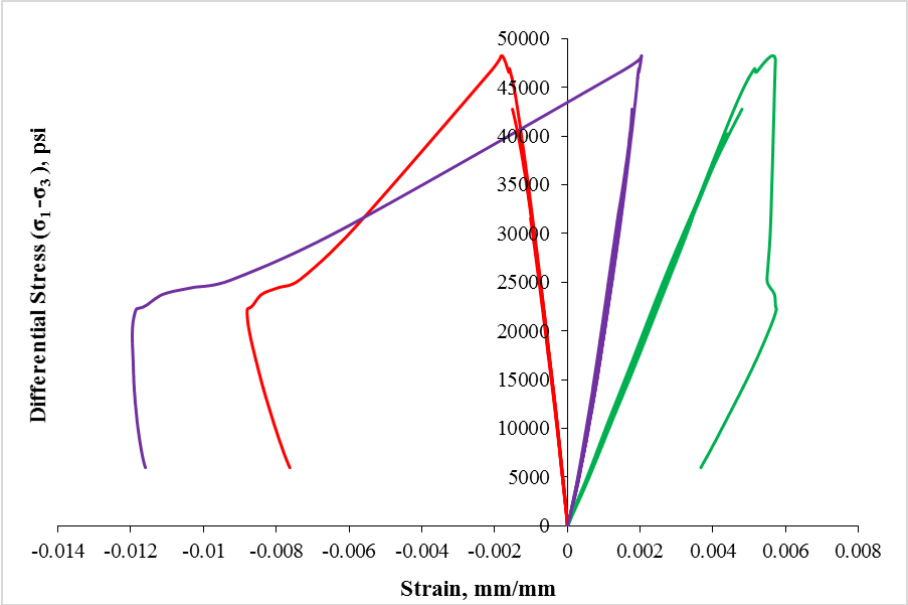

Fig. A.2 Stress-Strain Curves – Sample # 2

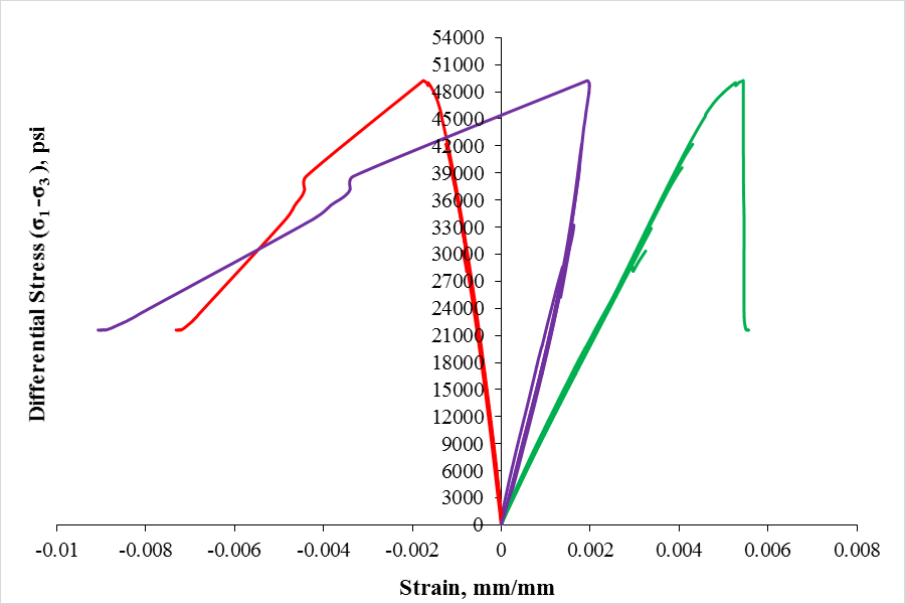

Fig. A.3 Stress-Strain Curves – Sample # 3

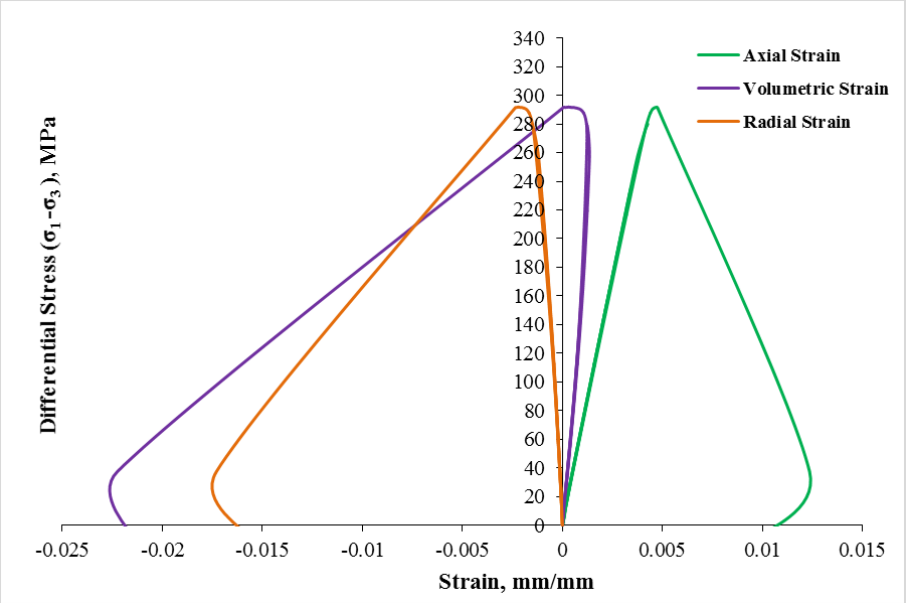

Fig. A.4 Stress-Strain Curves – Sample # 4

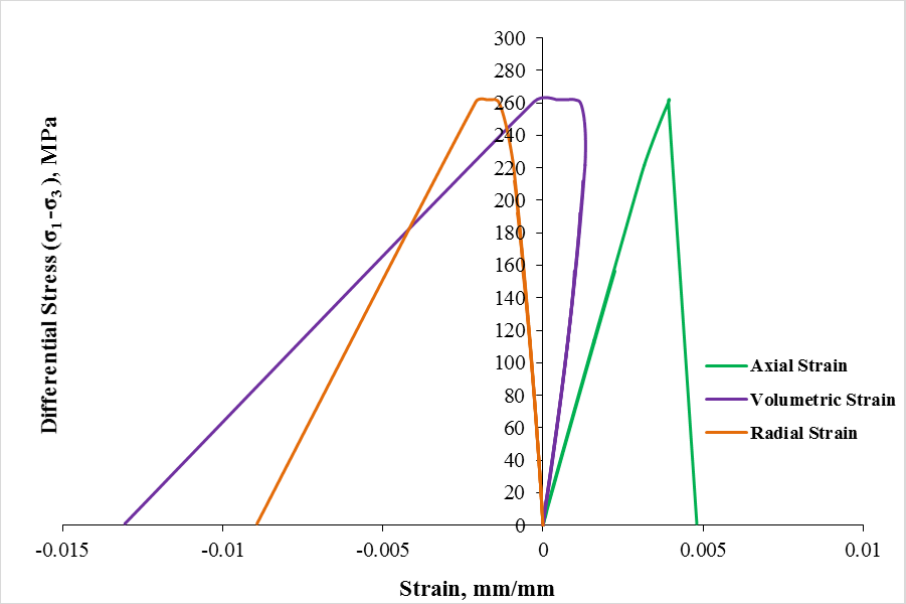

Fig. A.5 Stress-Strain Curves – Sample # 5

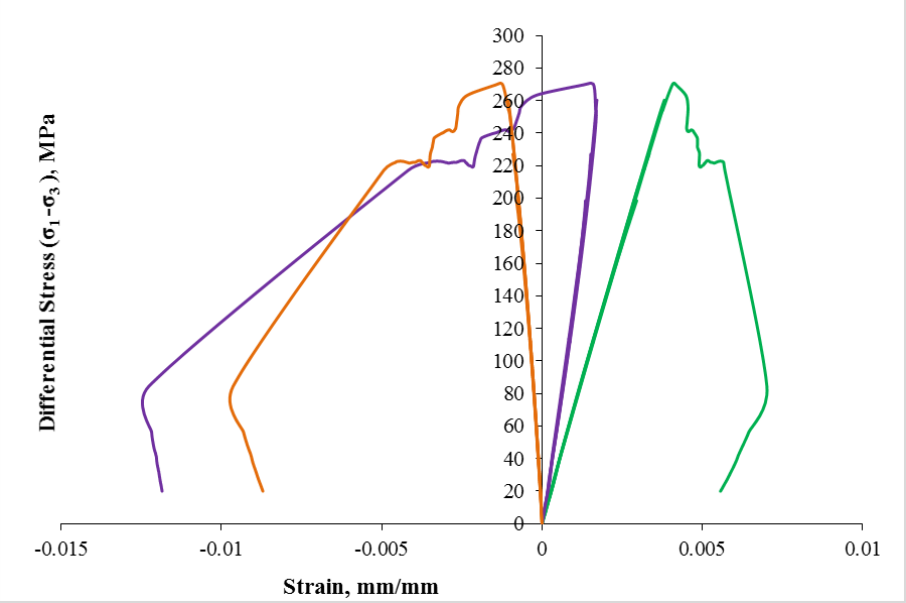

Fig. A.6 Stress-Strain Curves – Sample # 6

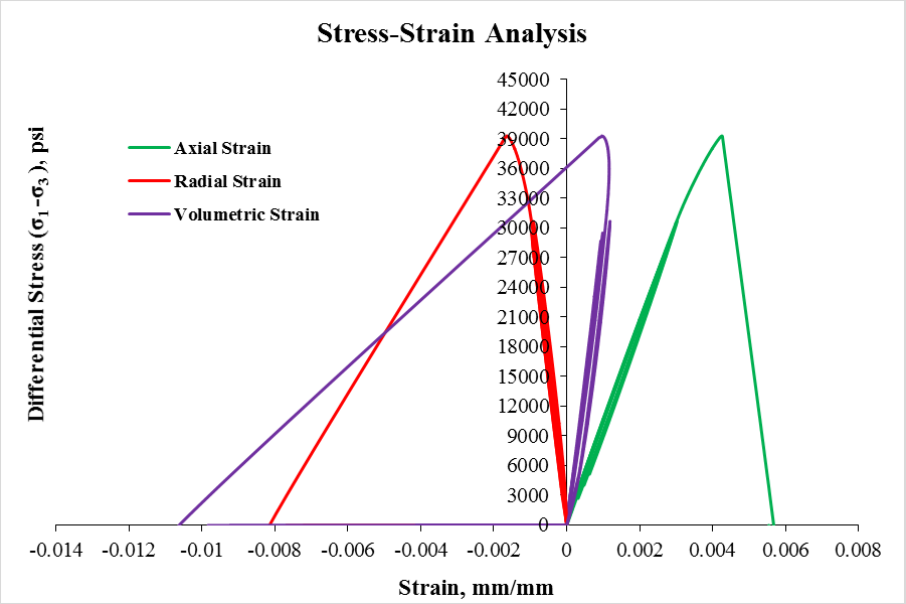

Fig. A.7 Stress-Strain Curves – Sample # 7

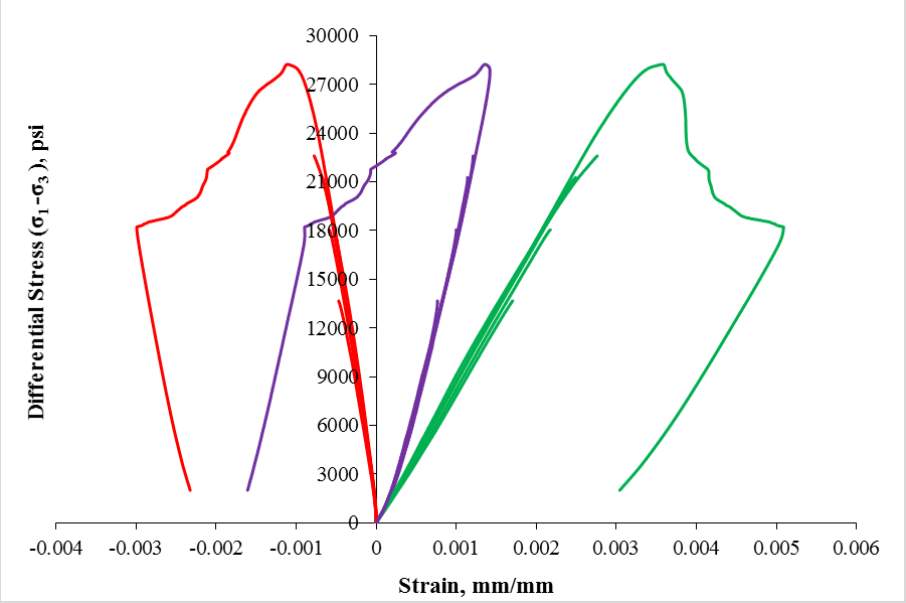

Fig. A.8 Stress-Strain Curves – Sample # 8

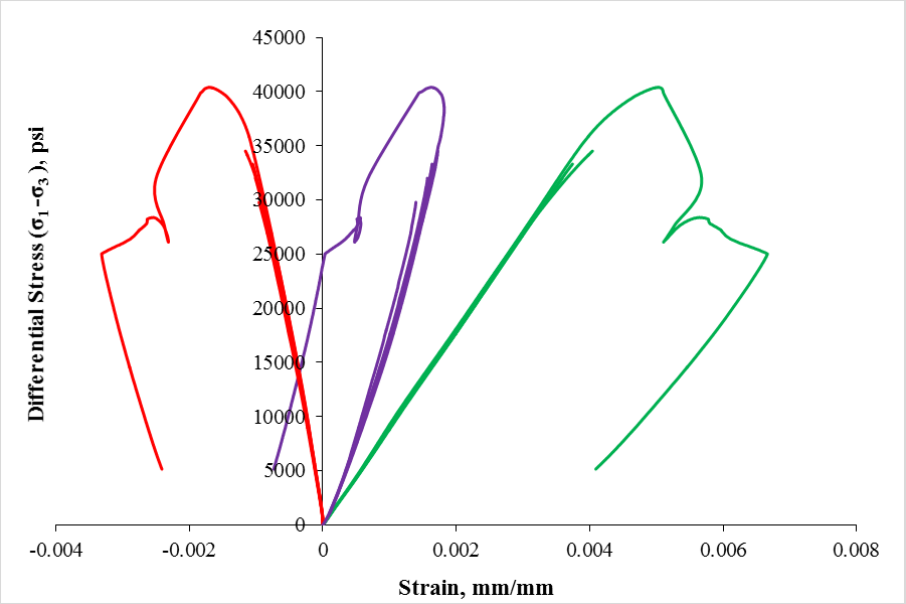

Fig. A.9 Stress-Strain Curves – Sample # 9

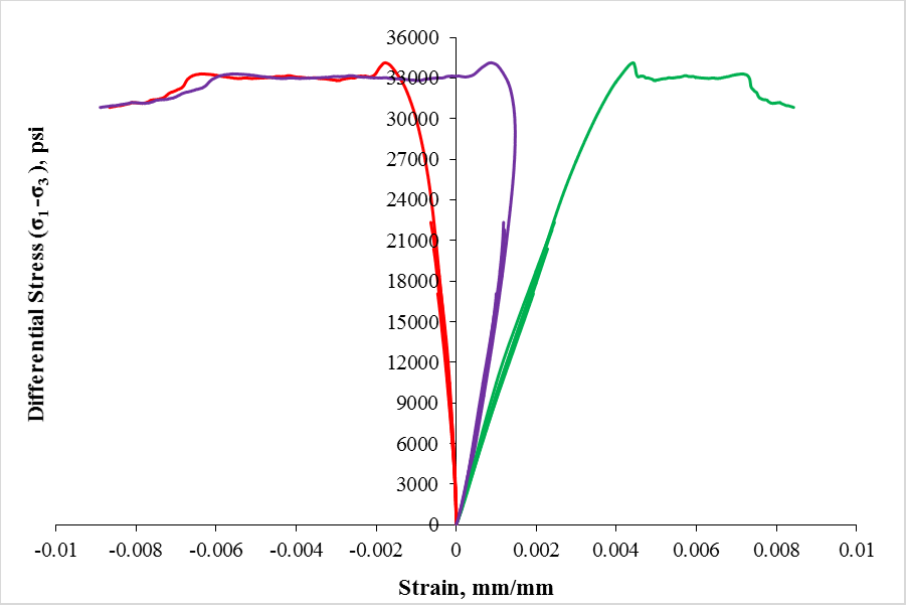

Fig. A.10 Stress-Strain Curves – Sample # 10

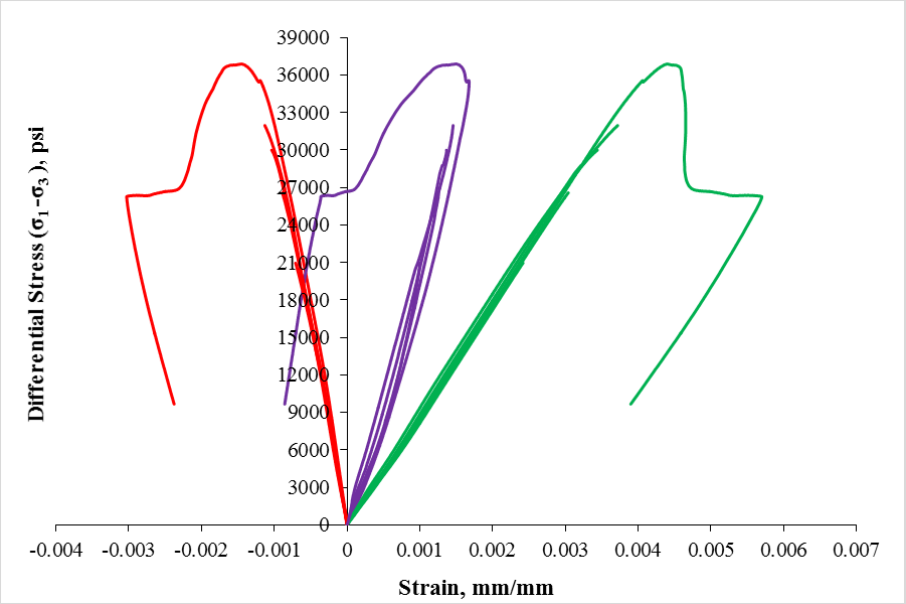

Fig. A.11 Stress-Strain Curves – Sample # 11

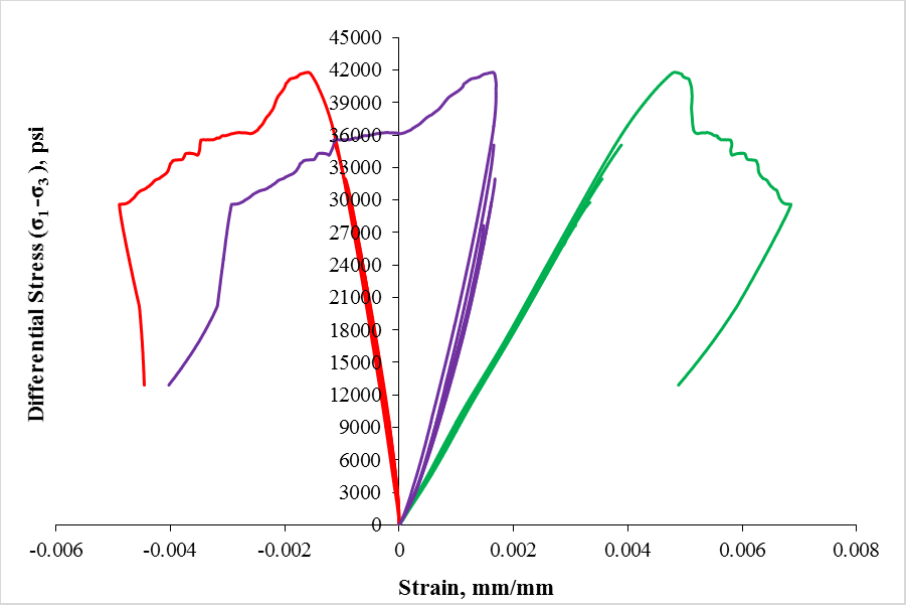

Fig. A.12 Stress-Strain Curves – Sample # 12

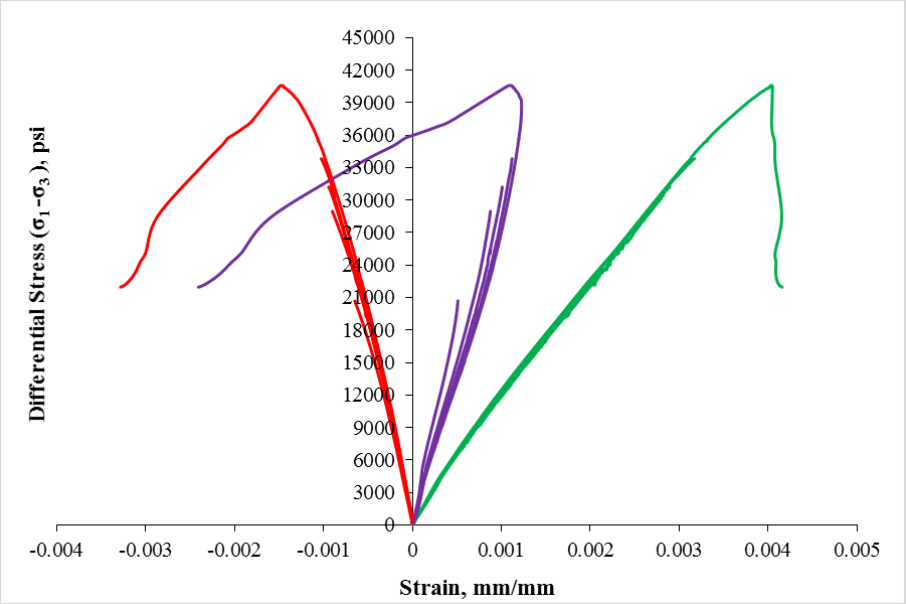

Fig. A.13 Stress-Strain Curves – Sample # 13

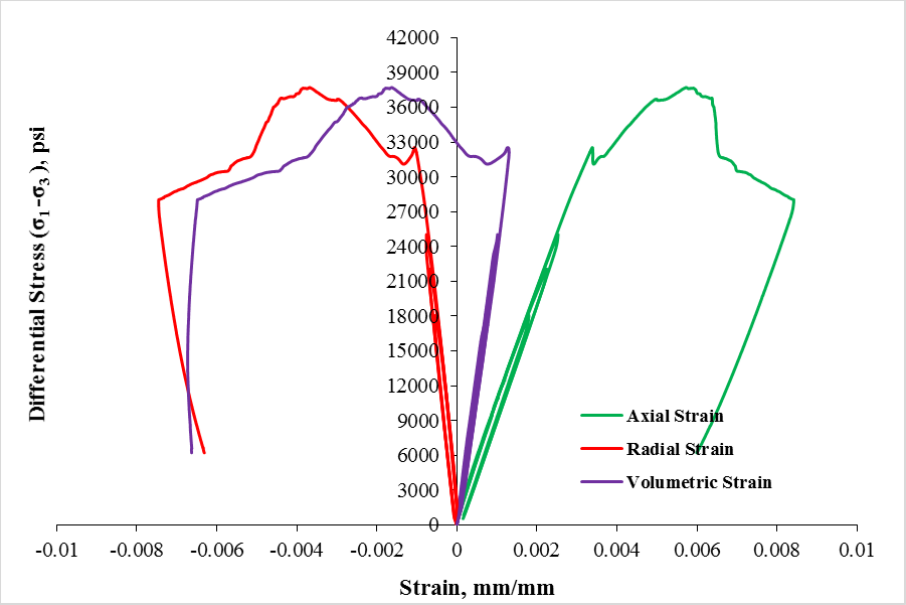

Fig. A.14 Stress-Strain Curves – Sample # 14

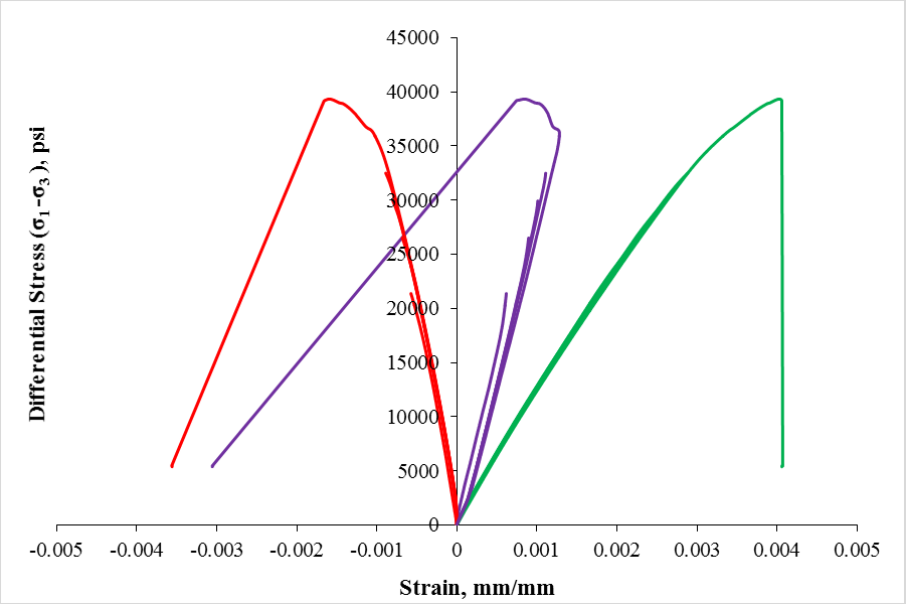

Fig. A.15 Stress-Strain Curves – Sample # 15

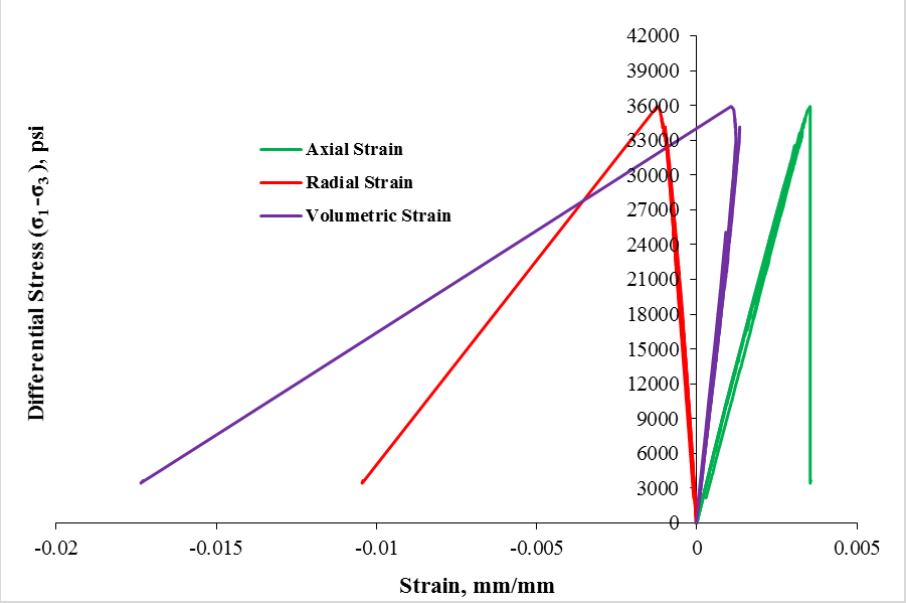

Fig. A.16 Stress-Strain Curves – Sample # 16

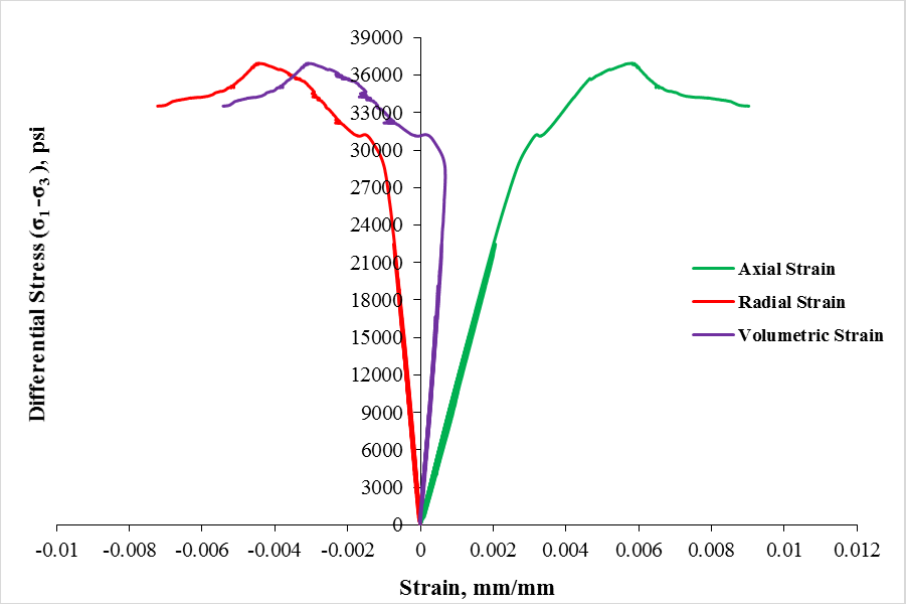

Fig. A.17 Stress-Strain Curves – Sample # 17

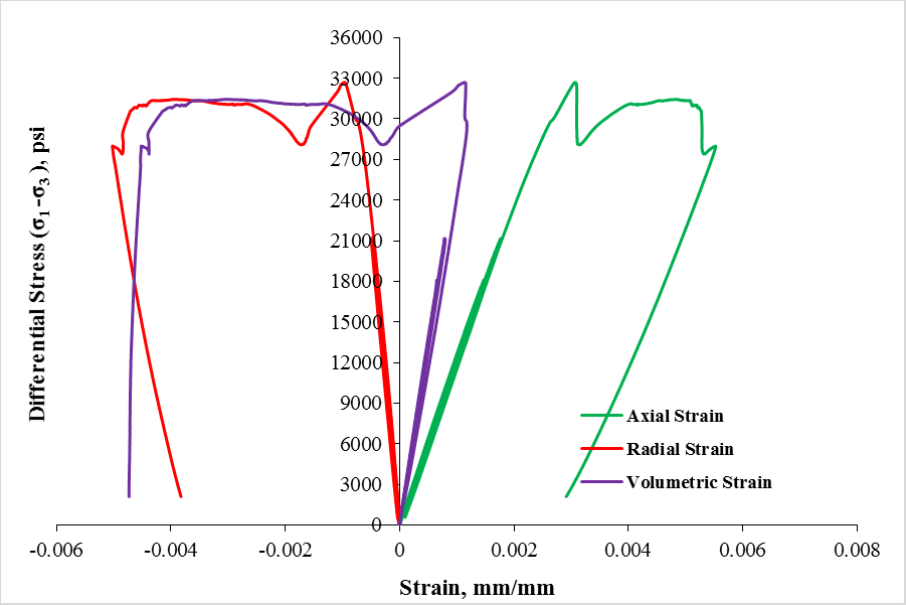

Fig. A.18 Stress-Strain Curves – Sample # 18

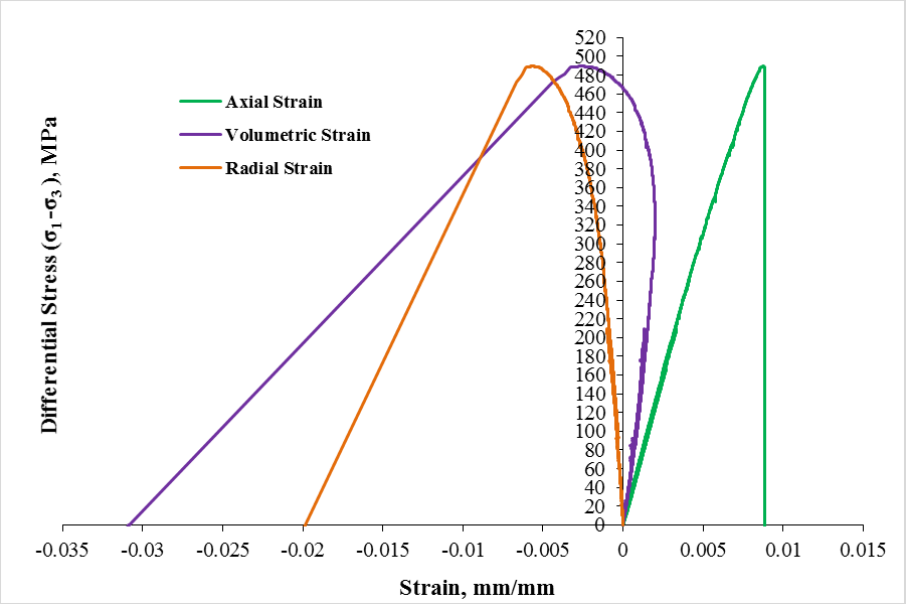

Fig. A.19 Stress-Strain Curves – Sample # 19

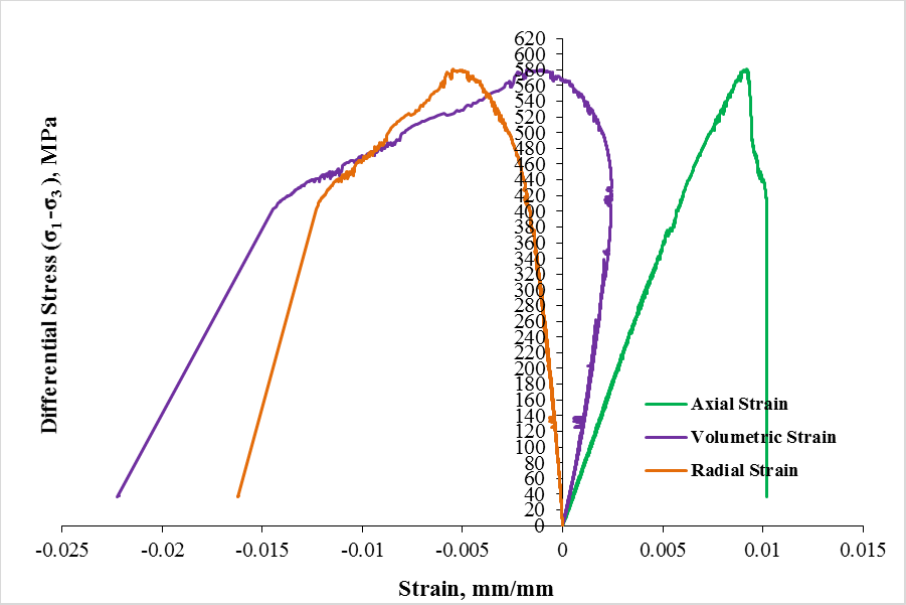

Fig. A.20 Stress-Strain Curves – Sample # 20

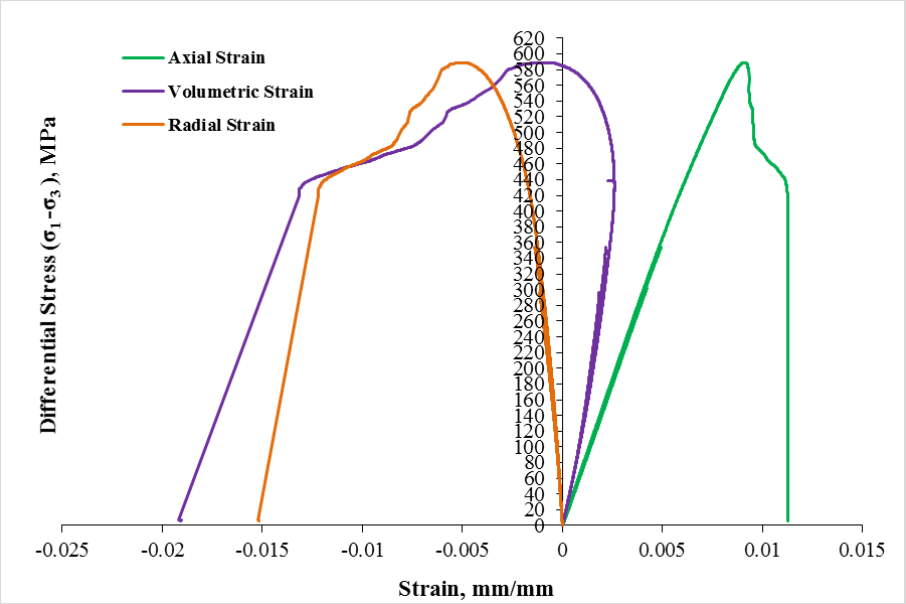

Fig. A.21 Stress-Strain Curves – Sample # 21

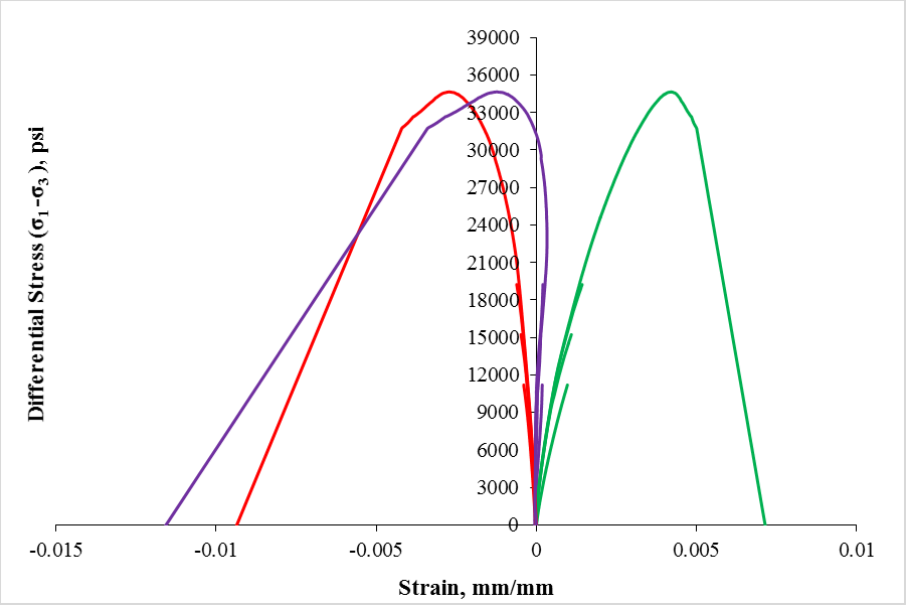

Fig. A.22 Stress-Strain Curves – Sample # 22* (with pre-existed fracture)

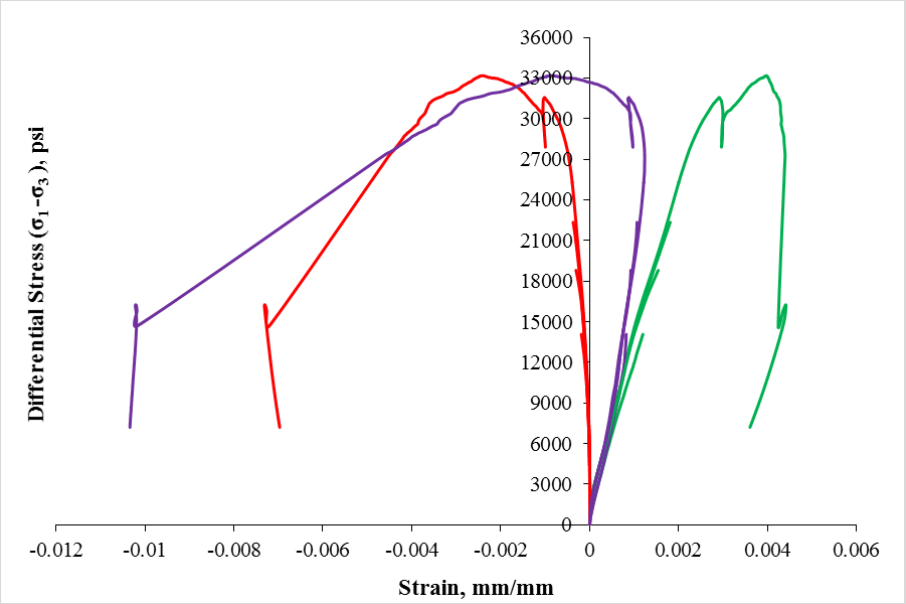

Fig. A.23 Stress-Strain Curves – Sample # 23* (with pre-existed fracture)

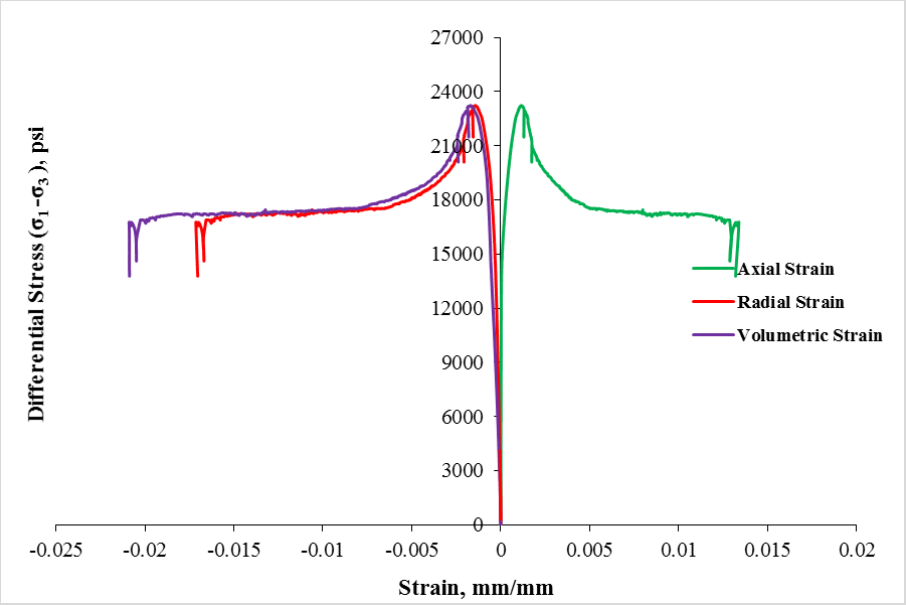

Fig. A.24 Stress-Strain Curves – Sample # 24* (with pre-existed fracture, single stage)

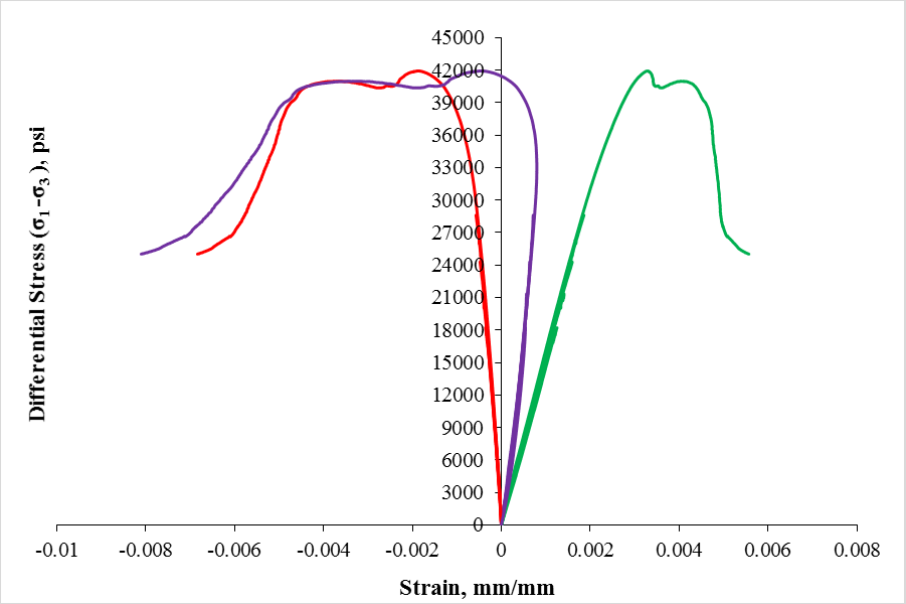

Fig. A.25 Stress-Strain Curves – Sample # 25

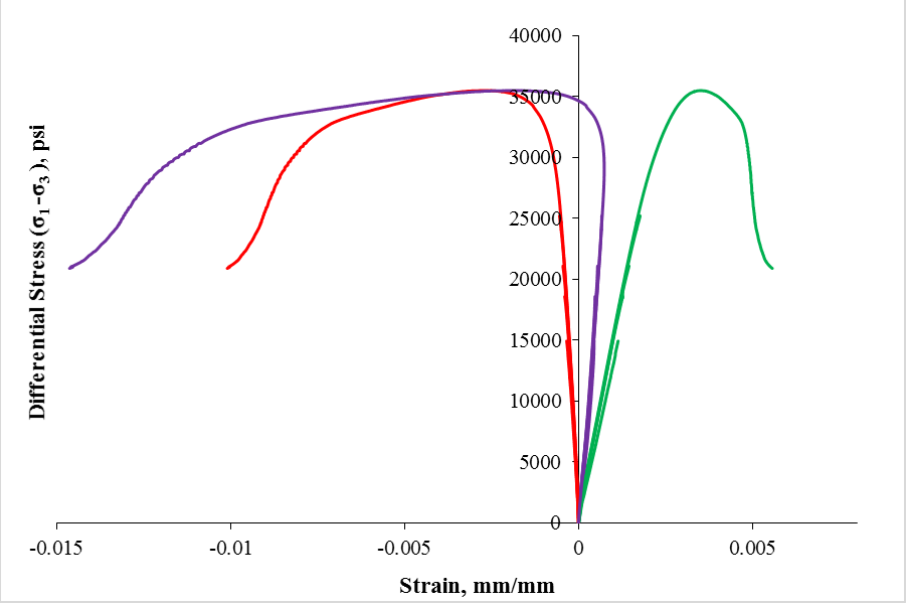

Fig. A.26 Stress-Strain Curves – Sample # 26

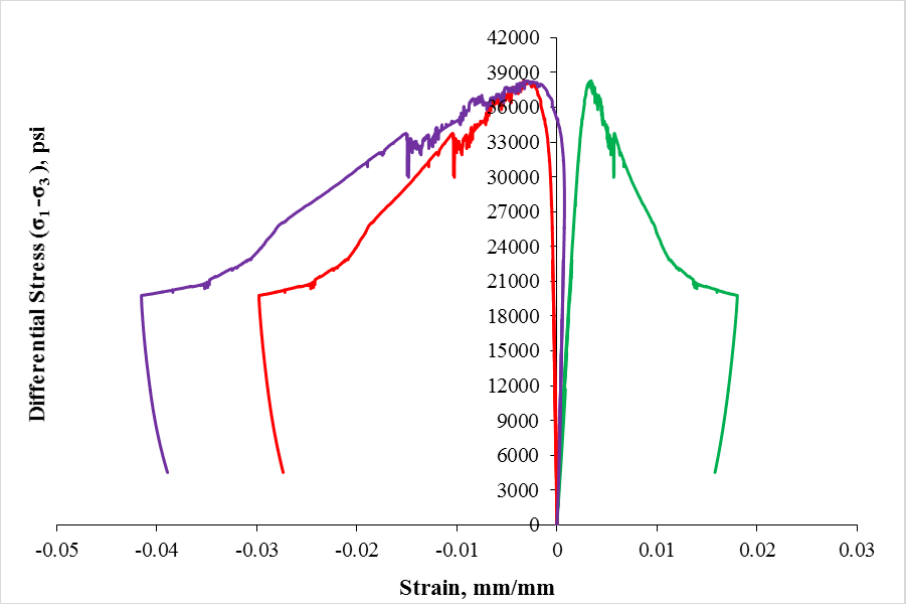

Fig. A.27 Stress-Strain Curves – Sample # 27

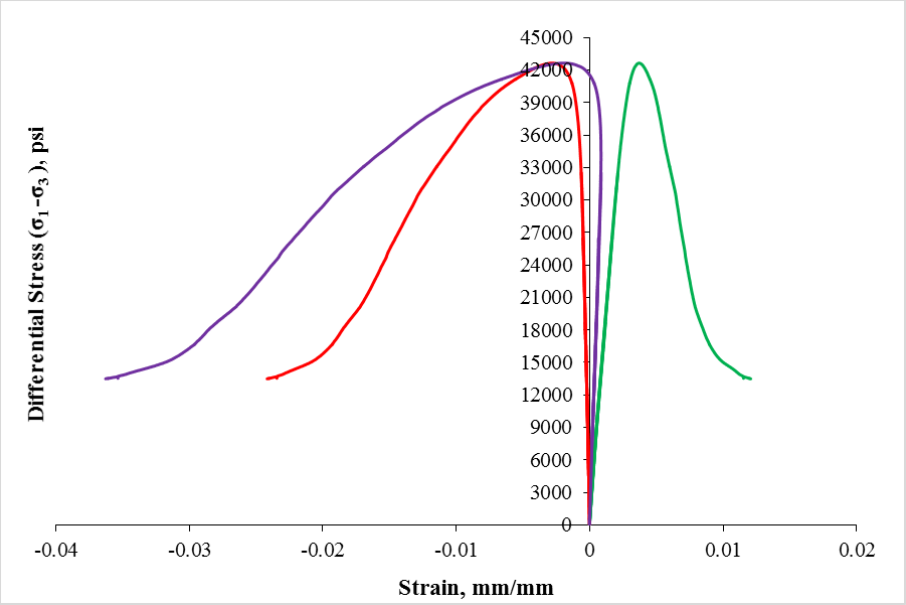

Fig. A.28 Stress-Strain Curves – Sample # 28

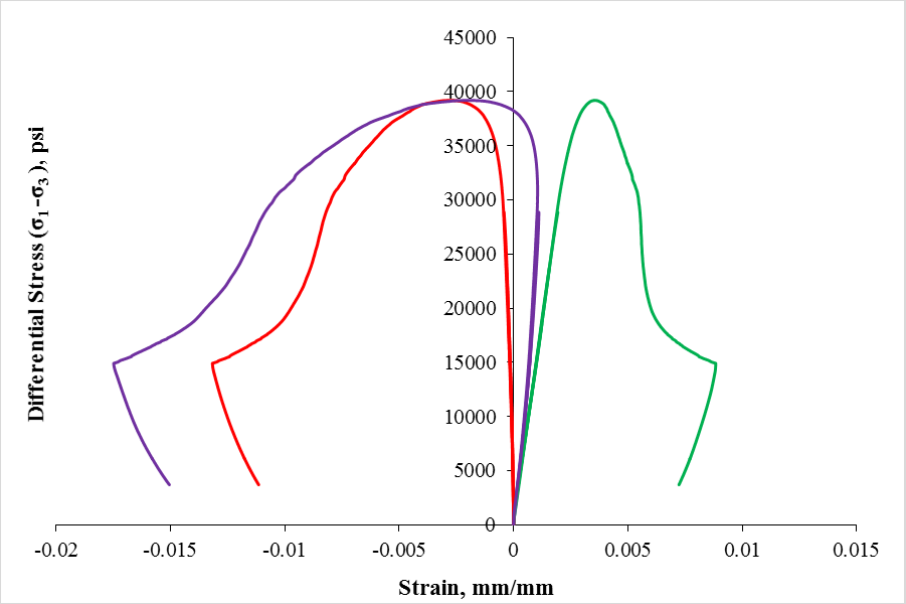

Fig. A.29 Stress-Strain Curves – Sample # 29

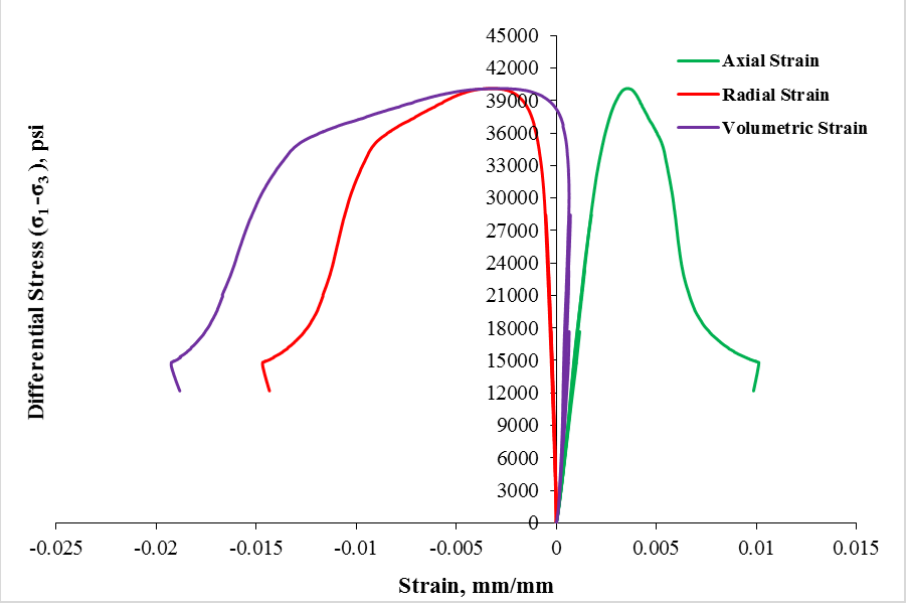

Fig. A.30 Stress-Strain Curves – Sample # 30

Appendix. B. Mohr-Coulomb Failure Envelopes

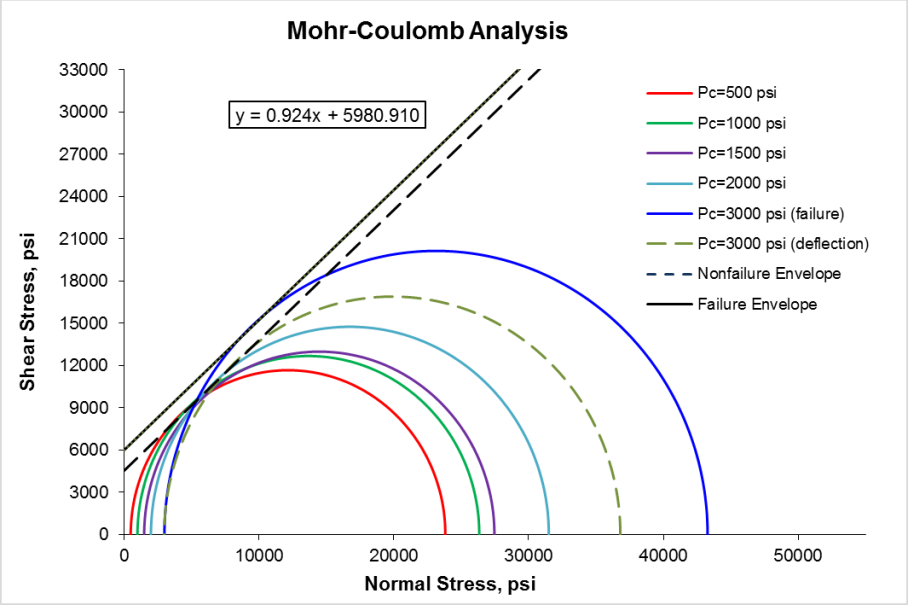

Fig. B.1 Mohr-Coulomb Failure Envelope – Sample # 1

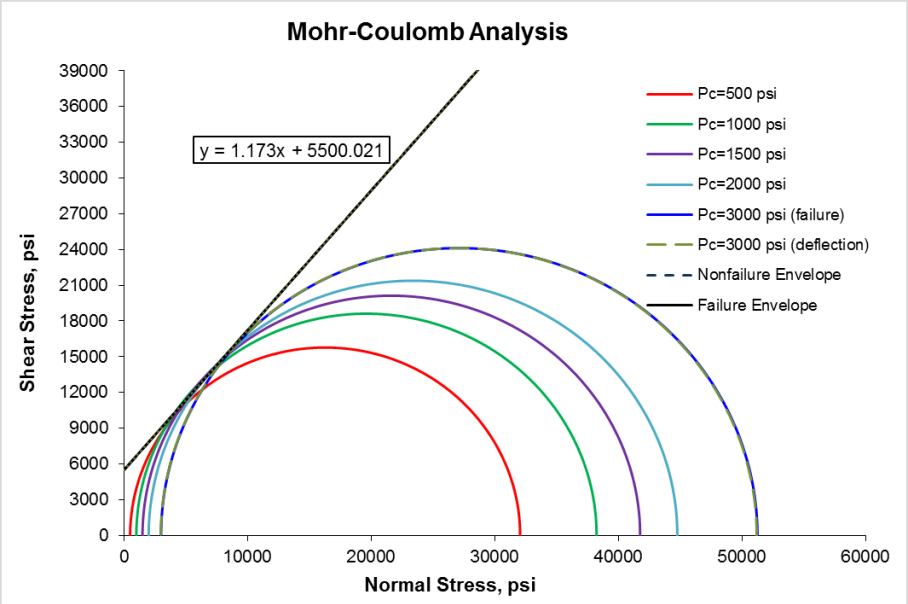

Fig. B.2 Mohr-Coulomb Failure Envelope – Sample # 2

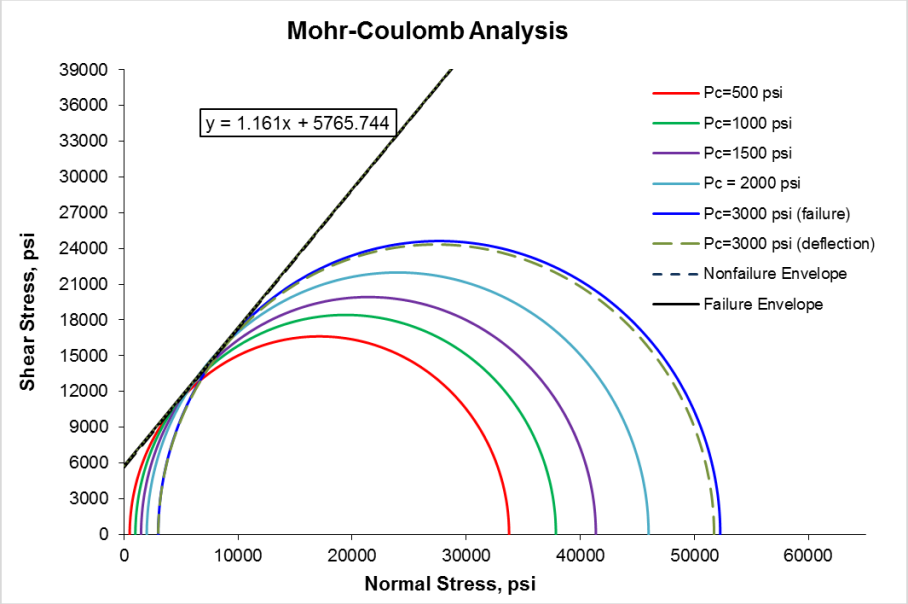

Fig. B.3 Mohr-Coulomb Failure Envelope – Sample # 3

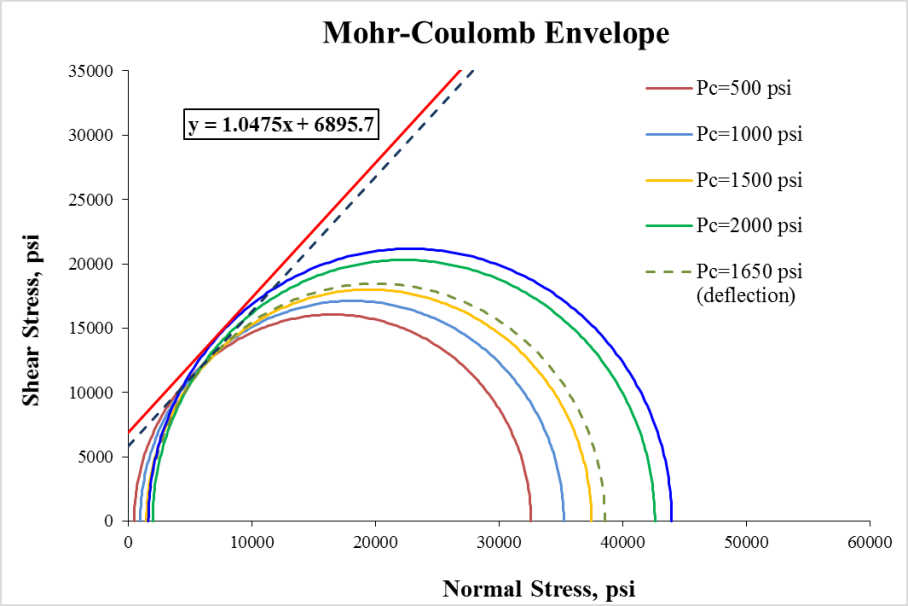

Fig. B.4 Mohr-Coulomb Failure Envelope – Sample # 4

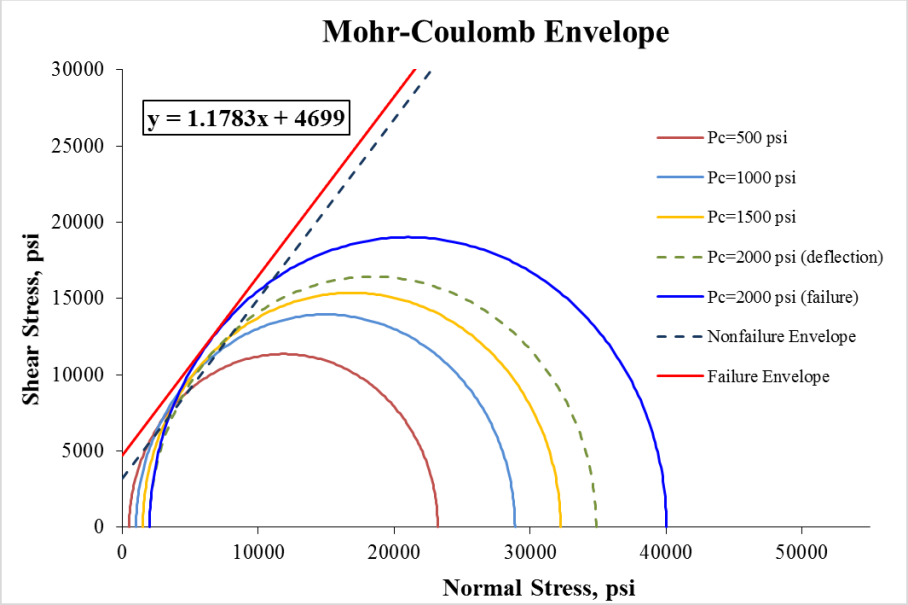

Fig. B.5 Mohr-Coulomb Failure Envelope – Sample # 5

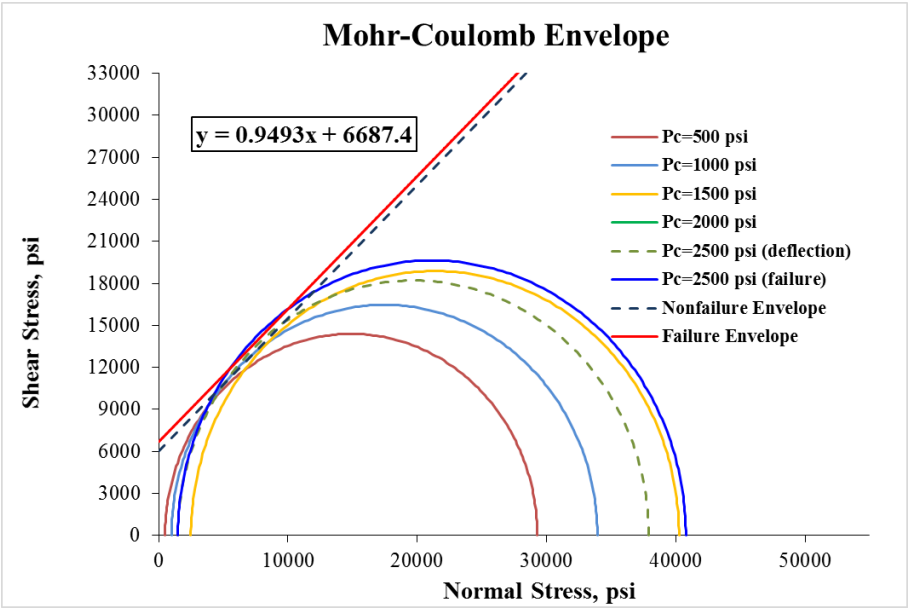

Fig. B.6 Mohr-Coulomb Failure Envelope – Sample # 6*

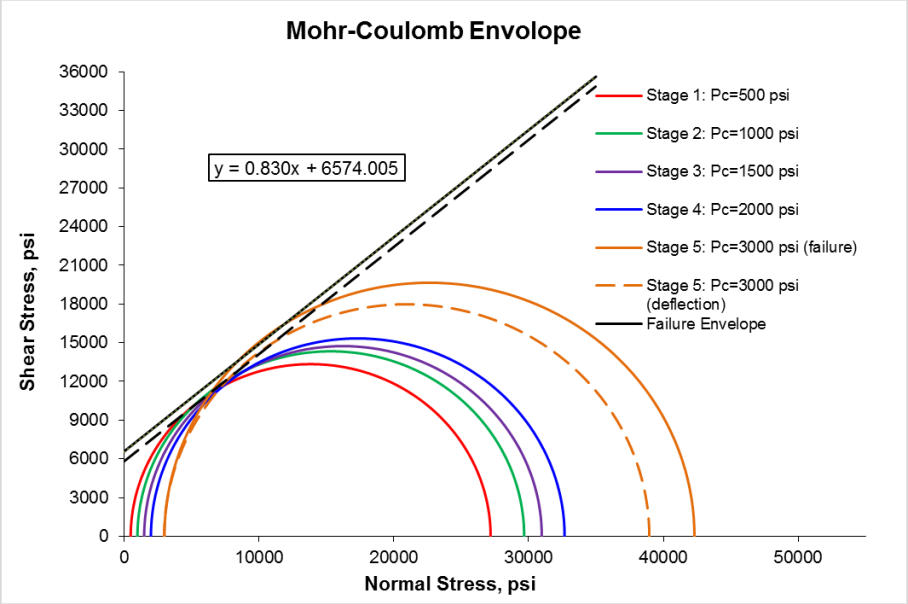

Fig. B.7 Mohr-Coulomb Failure Envelope – Sample # 7*

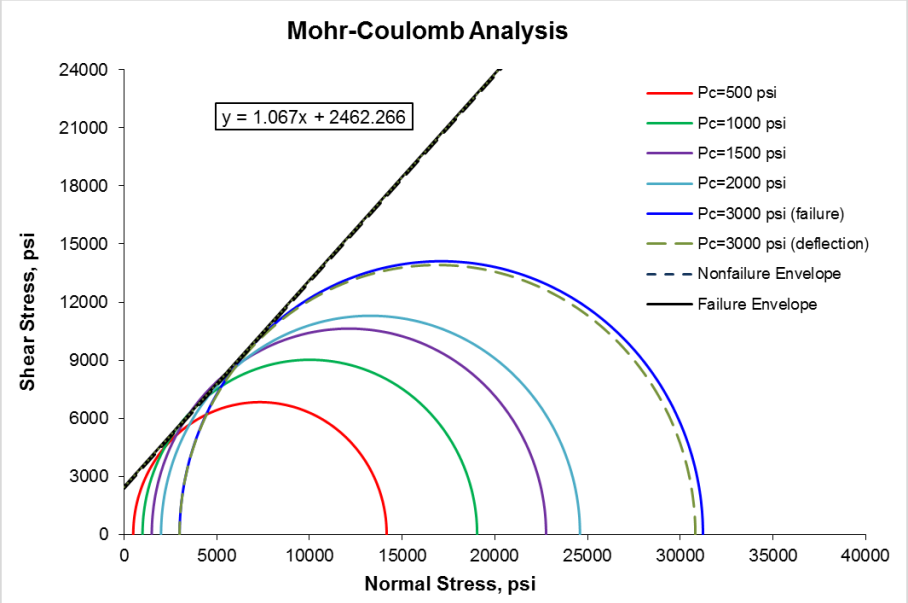

Fig. B.8 Mohr-Coulomb Failure Envelope – Sample # 8*

*Sample # 7 and # 8 have induced good single joint and been used for the triaxial shear testing.

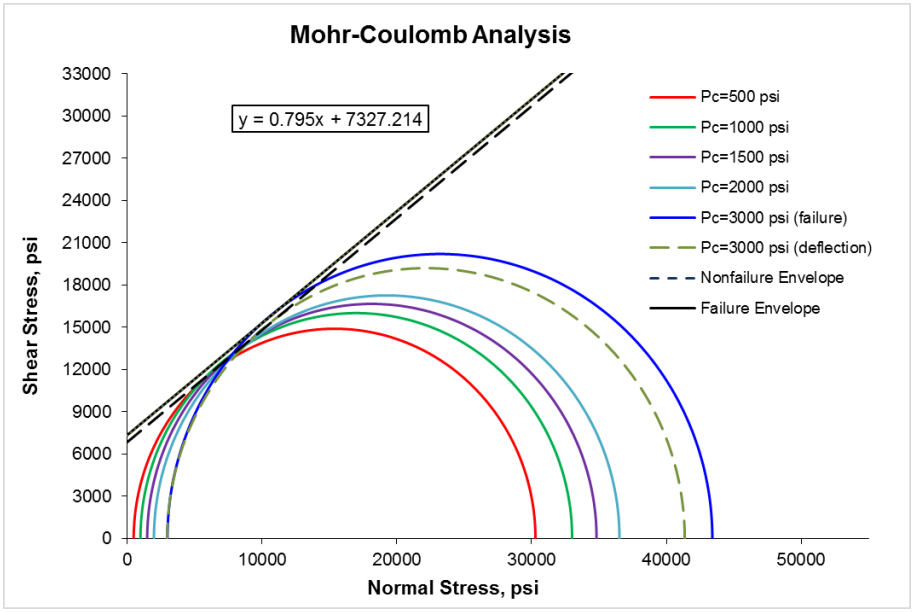

Fig. B.9 Mohr-Coulomb Failure Envelope – Sample # 9

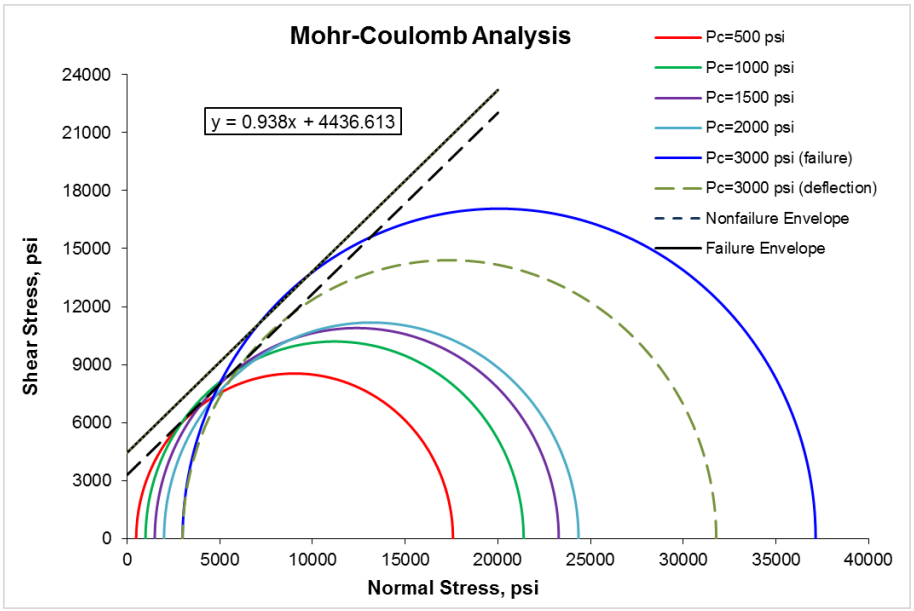

Fig. B.10 Mohr-Coulomb Failure Envelope – Sample # 10

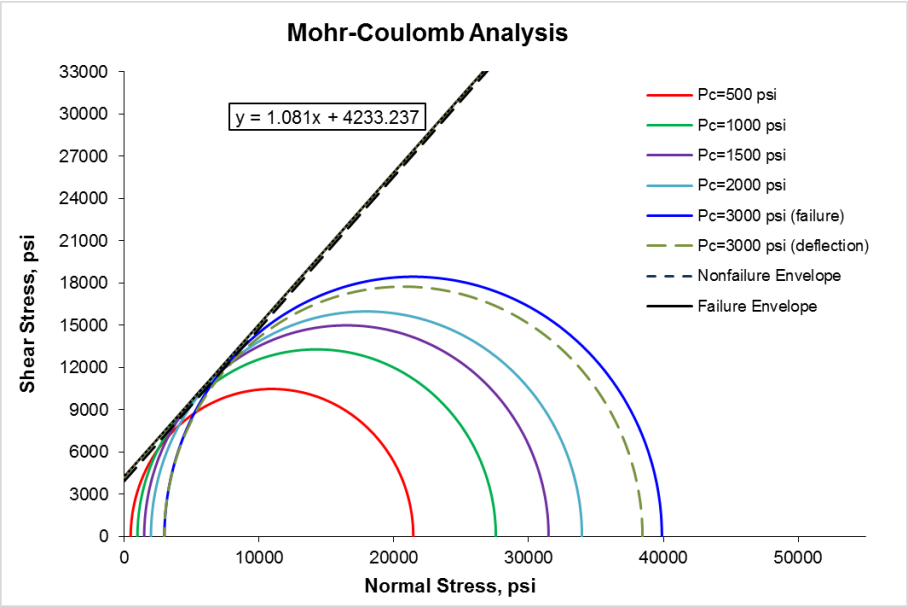

Fig. B.11 Mohr-Coulomb Failure Envelope – Sample # 11

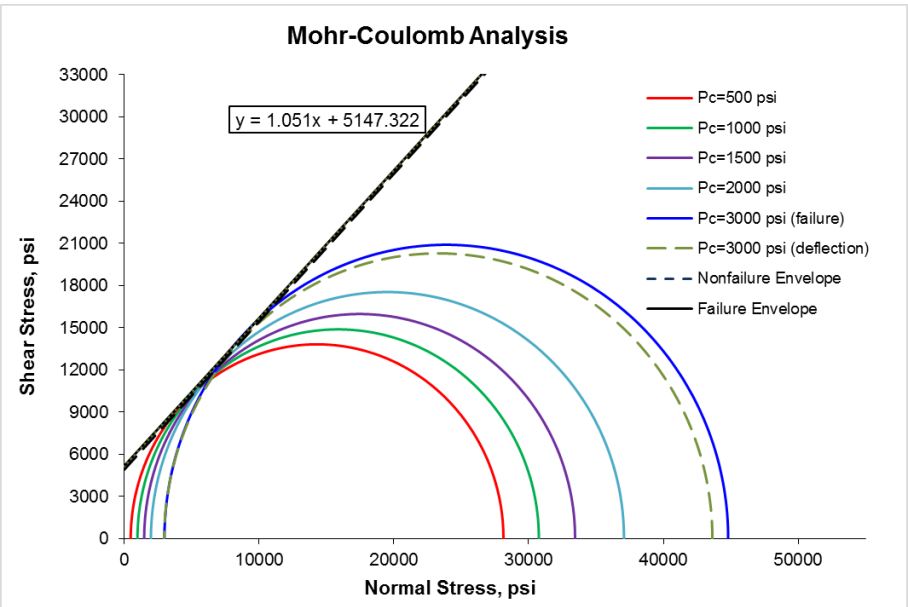

Fig. B.12 Mohr-Coulomb Failure Envelope – Sample # 12

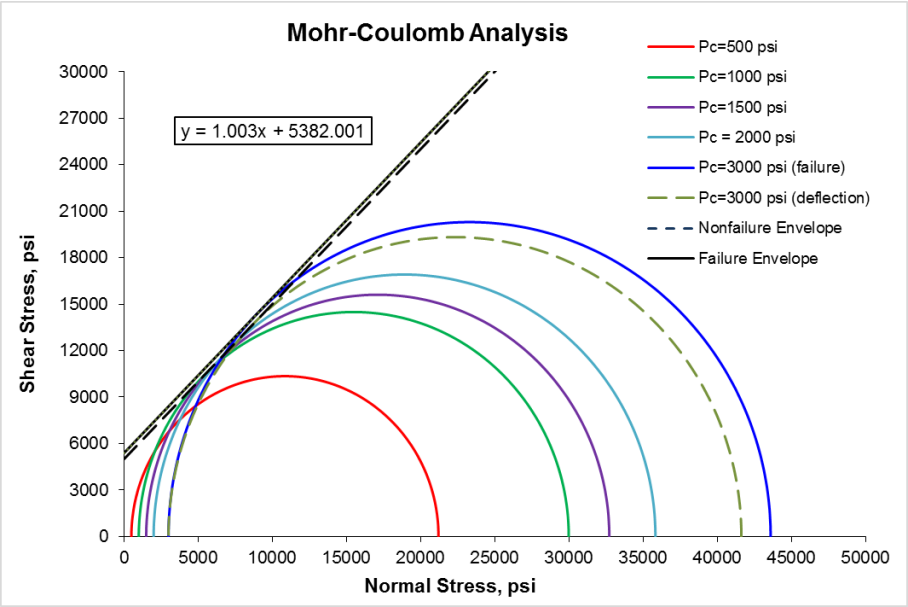

Fig. B.13 Mohr-Coulomb Failure Envelope – Sample # 13

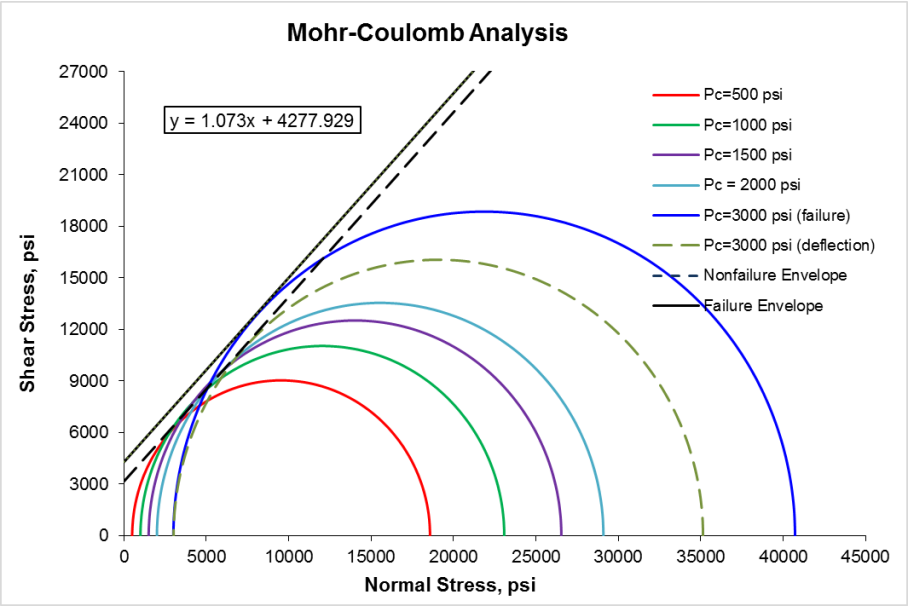

Fig. B.14 Mohr-Coulomb Failure Envelope – Sample # 14

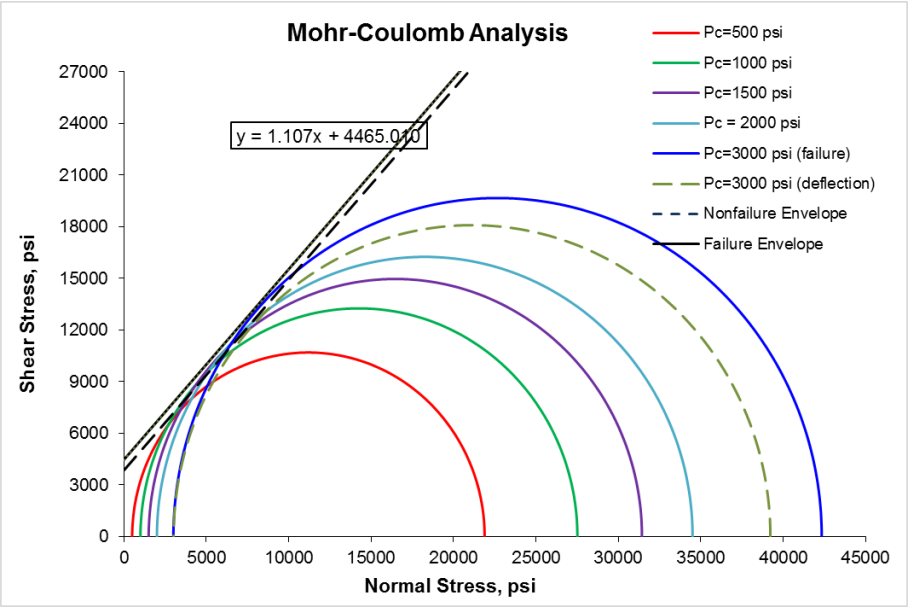

Fig. B.15 Mohr-Coulomb Failure Envelope – Sample # 15

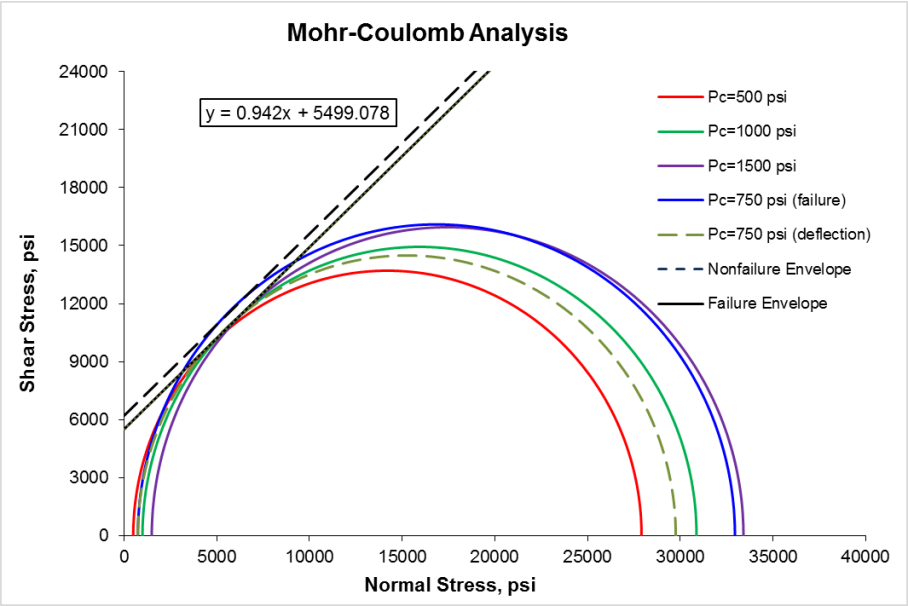

Fig. B.16 Mohr-Coulomb Failure Envelope – Sample # 16

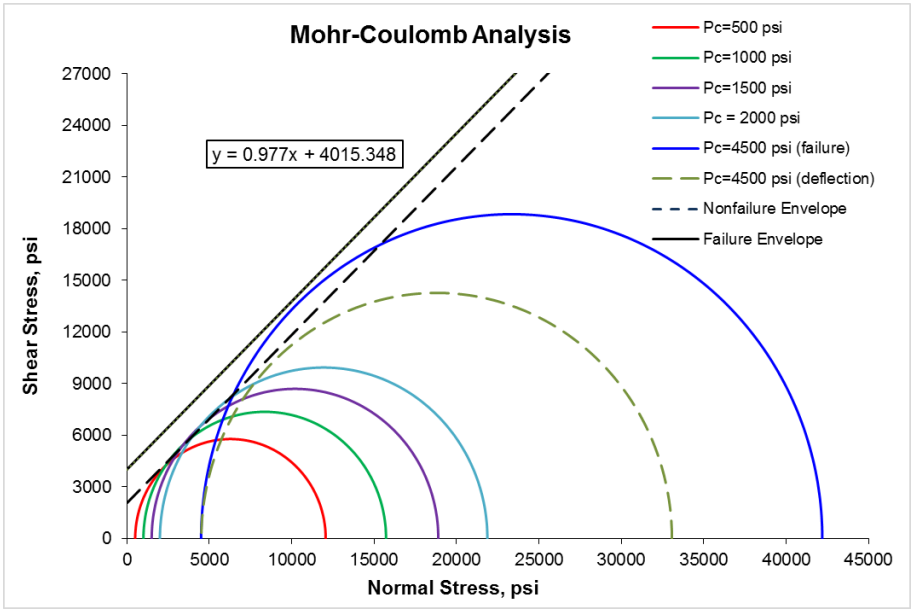

Fig. B.17 Mohr-Coulomb Failure Envelope – Sample # 17

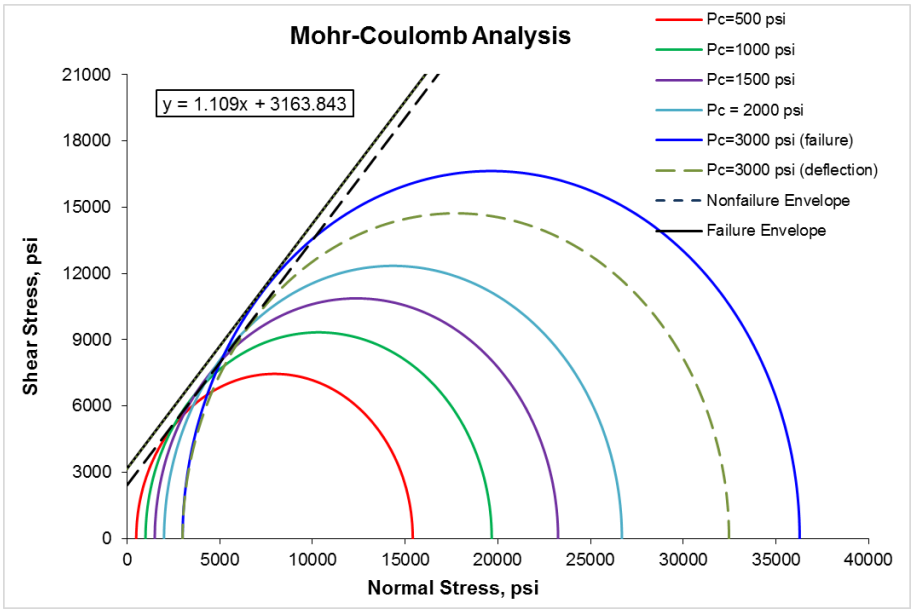

Fig. B.18 Mohr-Coulomb Failure Envelope – Sample # 18

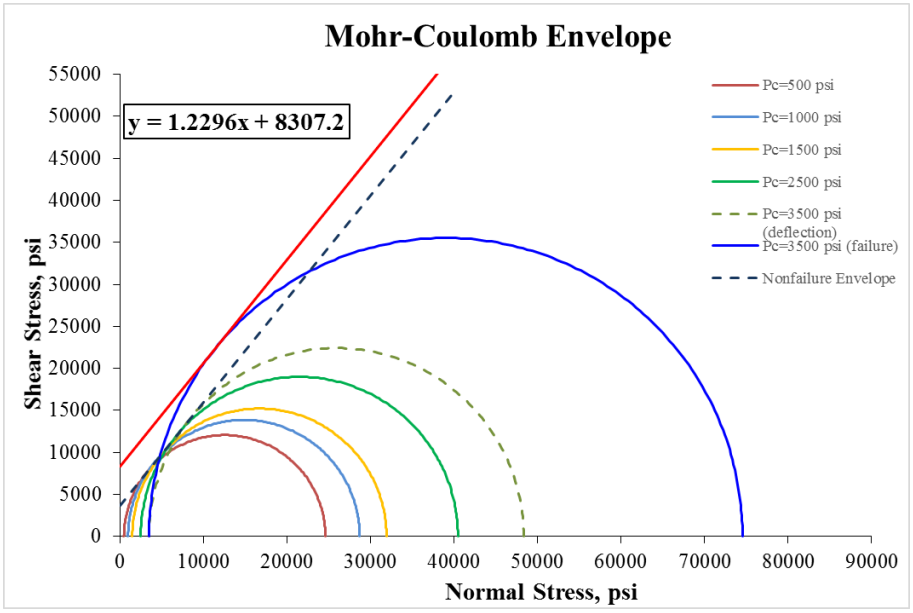

Fig. B.19 Mohr-Coulomb Failure Envelope – Sample # 19

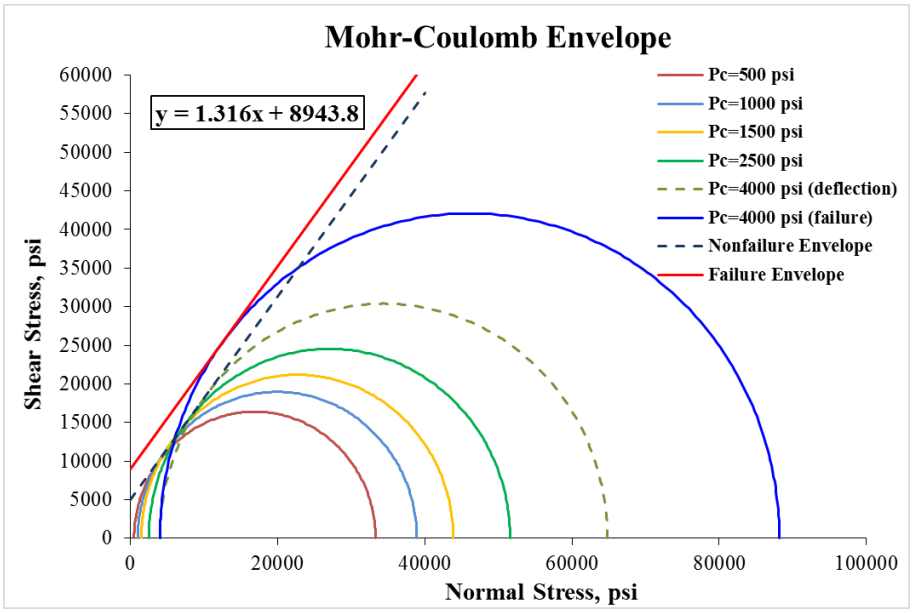

Fig. B.20 Mohr-Coulomb Failure Envelope – Sample # 20

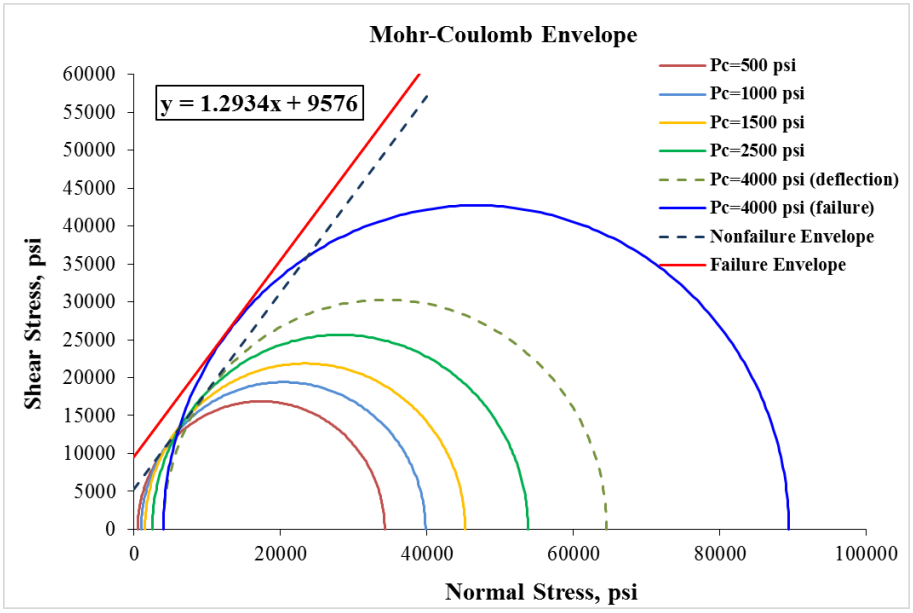

Fig. B.21 Mohr-Coulomb Failure Envelope – Sample # 21

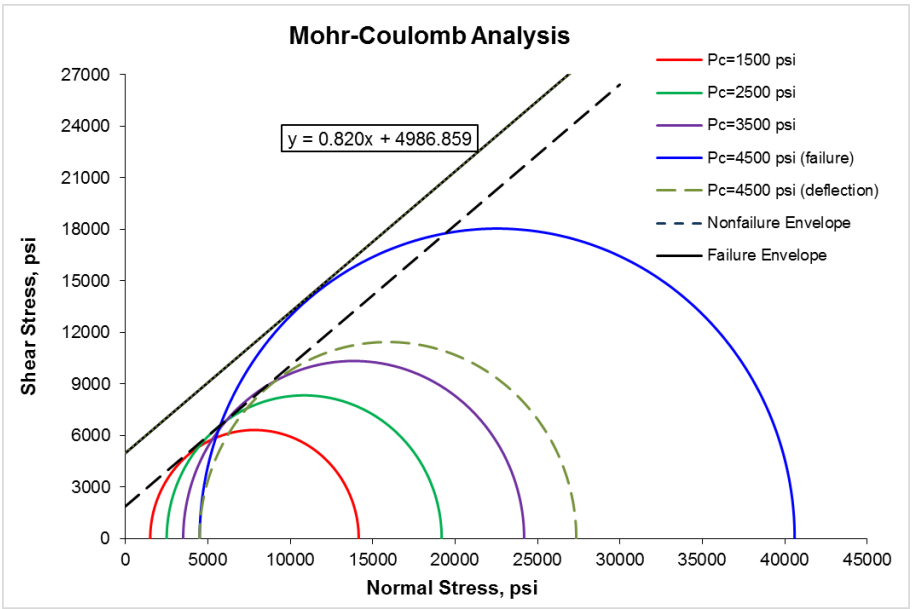

Fig. B.22 Mohr-Coulomb Failure Envelope – Sample # 22*(with pre-existed fracture)

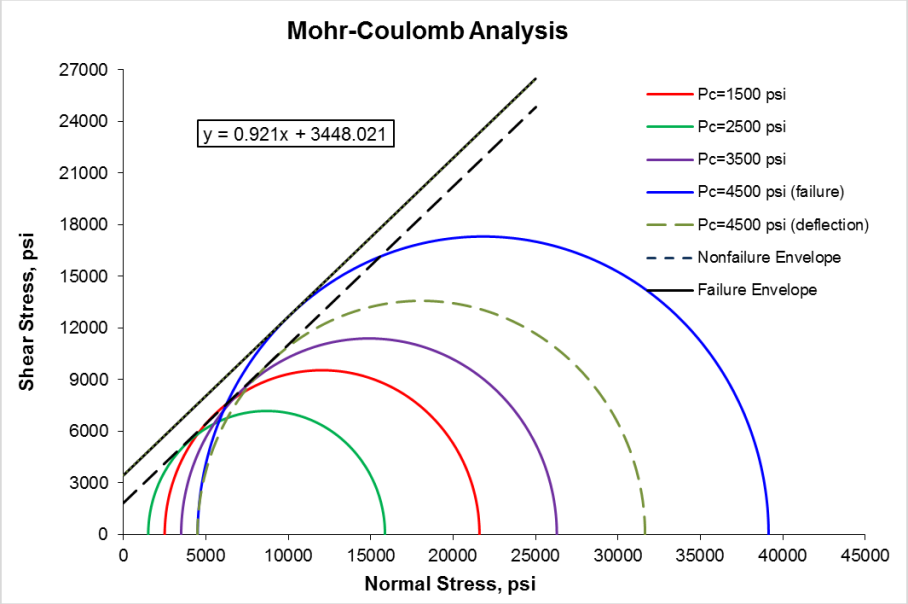

Fig. B.23 Mohr-Coulomb Failure Envelope – Sample # 23*(with pre-existed fracture)

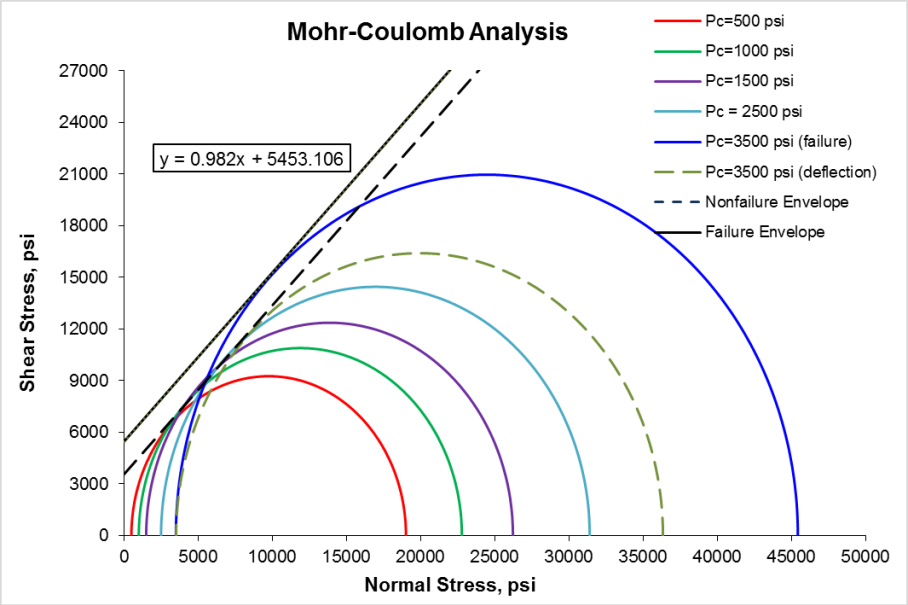

Fig. B.25 Mohr-Coulomb Failure Envelope – Sample # 25

*Sample # 23 has induced good single joint and been used for the triaxial shear test.

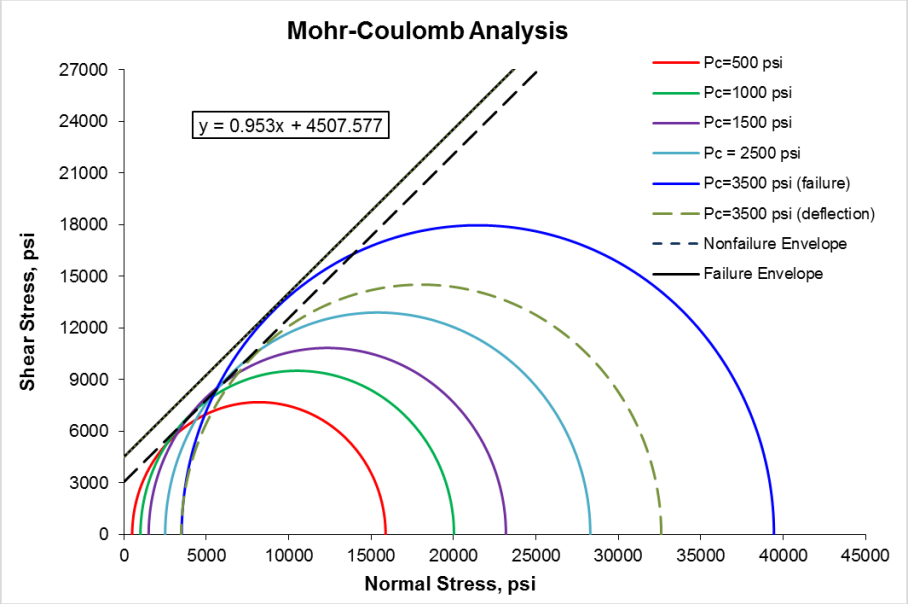

Fig. B.26 Mohr-Coulomb Failure Envelope – Sample # 26

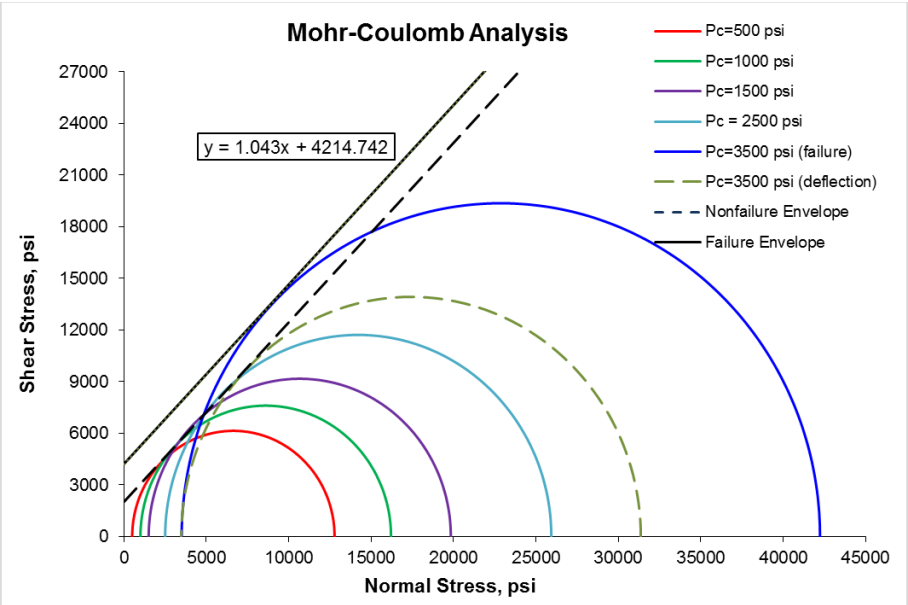

Fig. B.27 Mohr-Coulomb Failure Envelope – Sample # 27

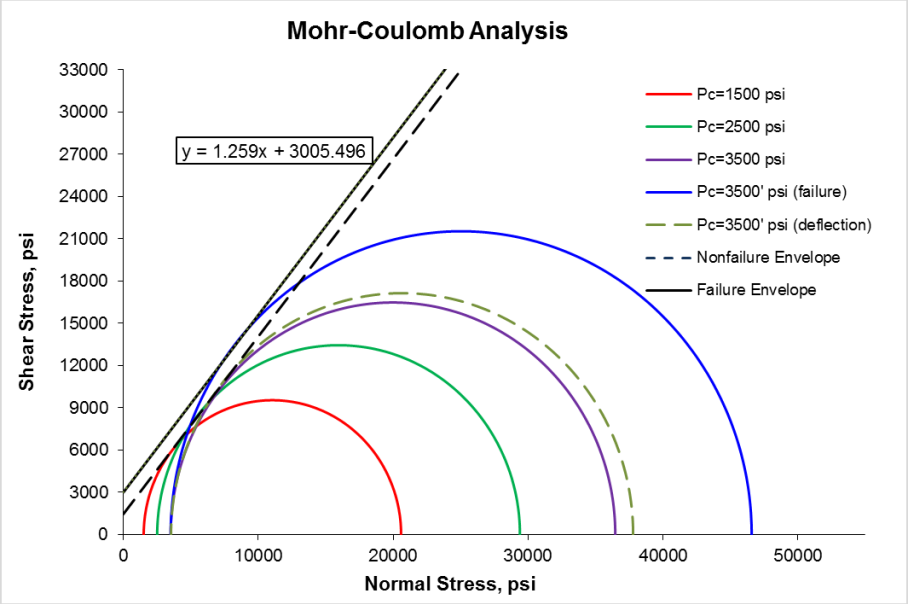

Fig. B.28 Mohr-Coulomb Failure Envelope – Sample # 28*(increased strain rate in failure stage)

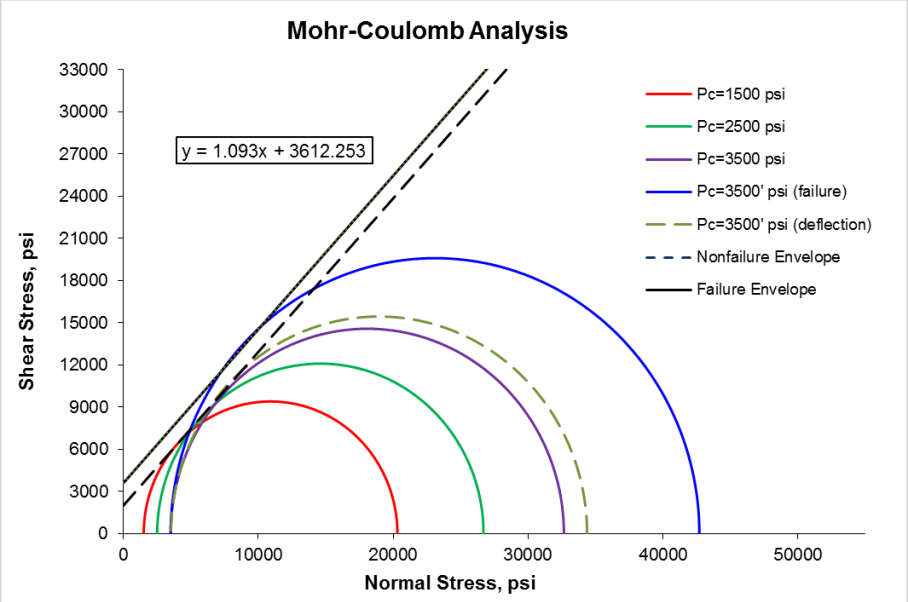

Fig. B.29 Mohr-Coulomb Failure Envelope – Sample # 29*(increased strain rate in failure stage)

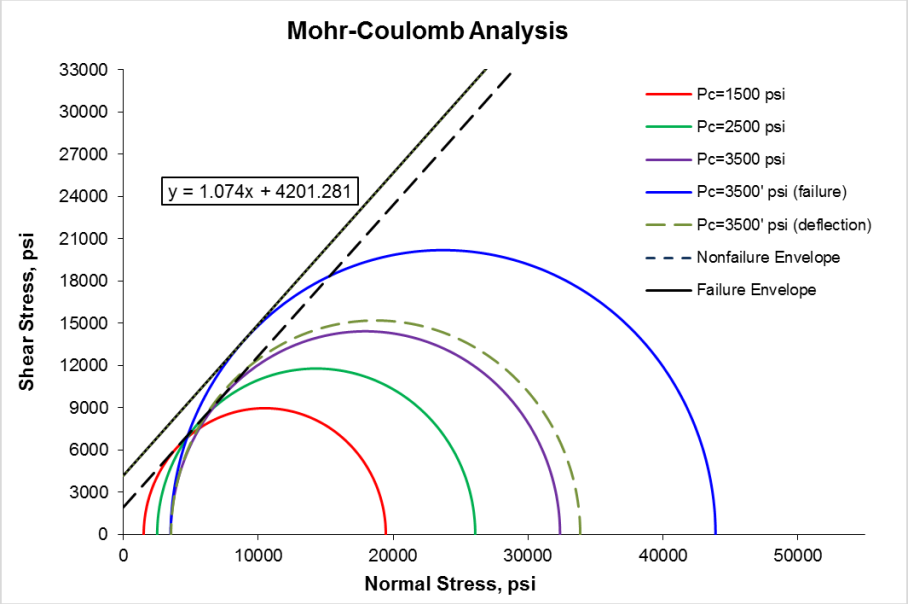

Fig. B.30 Mohr-Coulomb Failure Envelope – Sample # 30*(increased strain rate in failure stage)

As described in the previous chapters, the Roosevelt gabbro behaves more ductile than the other types of rock. Hence, for sample 28, 29, 30, the failure stage have used an increased strain rate to bring the rock to failure in order to get desired rock joints. For those samples, the slope of Mohr-Coulomb envelope was decided by only non-failure stages since the rock became stronger under higher strain rate. But the difference between failure and non-failure envelope are still obtained from the failure stage. The strength difference caused by the different strain rate is around 3% according to the stress of volumetric deflection point differences.

Appendix. C. LVDT Calibration

The calibration of the LVDT extensometers are made by a *Mitutoyo* micrometer as shown in the Fig. C-1. The accuracy of the micrometer is 0.001 mm.

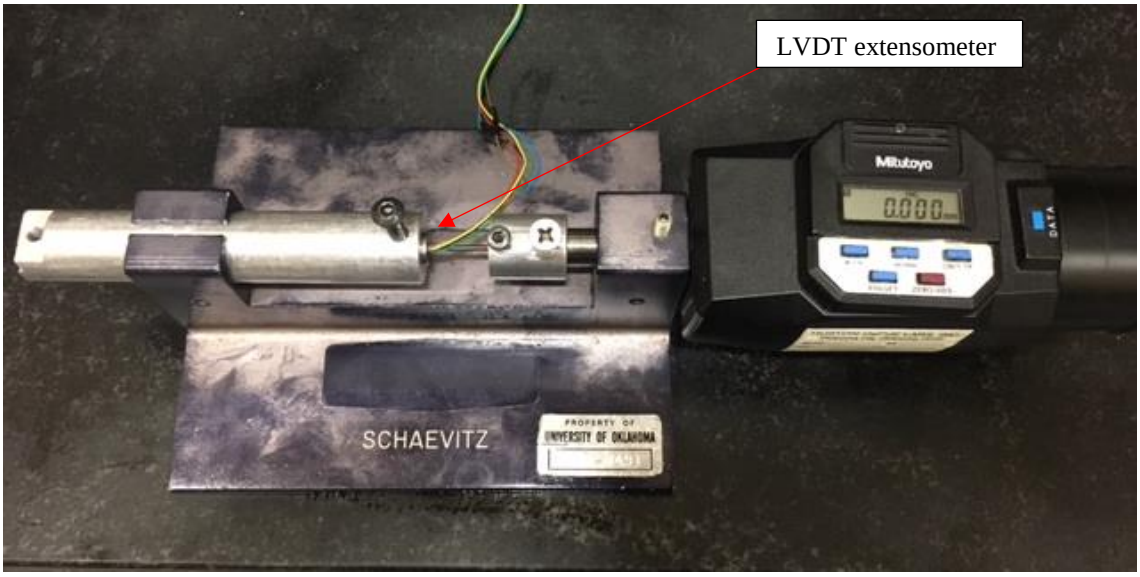

Fig. C.1 *The Mitutoyo Micrometer for LVDT extensometer calibrations*

To calibrate the LVDT extensometer, the sensor will be fixed in the extensometer (as in the figure) and connected to the experimental system. By manually adjust the relative displacement of the LVDT extensometer, the absolute displacement is shown in the screen of the micrometer. Meanwhile, the measured displacement is shown in the MTS series 793™ controller. The measured displacement (shown in the controller software) is calculated by the acquired voltage change times the *gain* (the parameter in the experimental software) by the software. To calibrate the sensor, the *gain* for each LVDT extensometer shall be manually adjusted to obtain the same measured displacement as the absolute displacement shown in the micrometer.

Following table summarizes the error of each LVDT extensometer after the calibration:

Table. C. 1 LVDT extensometer error after calibration

	LVDT 1		LVDT 2		LVDT 3	
Absolute Value	**Displayed Value**	**Error**	**Displayed Value**	**Error**	**Displayed Value**	**Error**
mm	mm	%	mm	%	mm	%
-2.00	-2.012	0.60%	-2.009	0.45%	-1.992	0.40%
-1.60	-1.608	0.50%	-1.614	0.88%	-1.591	0.56%
-1.20	-1.211	0.92%	-1.207	0.58%	-1.192	0.67%
-1.00	-1.004	0.40%	-1.013	1.30%	-0.995	0.50%
-0.80	-0.804	0.50%	-0.807	0.88%	-0.791	1.13%
-0.60	-0.603	0.50%	-0.614	2.33%	-0.600	0.00%
-0.40	-0.405	1.25%	-0.408	2.00%	-0.398	0.50%
-0.20	-0.206	3.00%	-0.203	1.50%	-0.199	0.50%
0.20	0.198	1.00%	0.197	1.50%	0.197	1.50%
0.40	0.400	0.00%	0.398	0.50%	0.400	0.00%
0.60	0.599	0.17%	0.599	0.17%	0.599	0.17%
0.80	0.794	0.75%	0.800	0.00%	0.795	0.63%
1.00	0.995	0.50%	1.000	0.00%	0.996	0.40%
1.20	1.192	0.67%	1.196	0.33%	1.196	0.33%
1.60	1.588	0.75%	1.597	0.19%	1.595	0.31%
2.00	1.990	0.50%	1.993	0.35%	1.990	0.50%
	Average error	**0.75%**	**Average error**	**0.81%**	**Average error**	**0.51%**